

**Radiometric measurement of
thermodynamic temperatures during the
phase transformation of metal-carbon
eutectic alloys for a new high-temperature
scale above 1000 °C**

vorgelegt von
Diplom-Physiker
Klaus Anhalt
aus Fulda

Der Fakultät II - Mathematik und Naturwissenschaften
der Technischen Universität Berlin
zur Erlangung des akademischen Grades
Doktor der Ingenieurwissenschaften
Dr.-Ing.

genehmigte Dissertation

Promotionsausschuss:

Vorsitzender: Prof. Dr. E. Sedlmayer
Berichter/Gutachter: Prof. Dr. C. Thomsen
Berichter/Gutachter: PD Dr. A. Hoffmann

Tag der wissenschaftlichen Aussprache: 25.7.2008

Berlin 2008

D 83

Die Internationale Temperaturskala von 1990 (ITS-90) ist definiert anhand von Temperaturfixpunkten und interpolierenden Messverfahren. Im Hochtemperaturbereich oberhalb der Erstarrungstemperatur von Kupfer (1084 °C) jedoch fehlen bislang stabile Fixpunkte. Die Extrapolation oberhalb des Erstarrungspunktes von Kupfer limitiert die erreichbare Unsicherheit der Temperaturskala. Neuartige Temperaturfixpunkte aus eutektischen Metallkohlenstofflegierungen (M-C) gefertigt in einem Graphittiegel versprechen hier erstmals eine Lösung. Die vorliegende Arbeit untersucht das Potential dieser M-C-Fixpunkte für die Strahlungsthermometrie und Radiometrie. Dazu werden Messtechniken entwickelt, die es erlauben die Stabilität, Reproduzierbarkeit und die Phasenübergangstemperatur dieser Fixpunkte mit kleinst-möglicher Unsicherheit unter Verwendung absolut-radiometrischer Methoden zu bestimmen.

Für Fixpunkte unterschiedlicher Herkunft aus Co-C (1325 °C), Pd-C (1492°C), Pt-C (1738 °C), Ru-C (1954 °C) und Re-C (2475 °C) konnte eine Reproduzierbarkeit von bis zu ± 100 mK nachgewiesen werden. Für die Bestimmung der Phasenübergangstemperatur wurde ein Messverfahren entwickelt, das eine optimale Zellform mit den geringen Messunsicherheiten der radiometrischen Temperaturbestimmung mit Filterradiometern kombiniert. Mit diesem Verfahren konnte erstmals die thermodynamische Phasenübergangstemperatur von Co-C, Pt-C, Ru-C und Pd-C mit einer Messunsicherheit ($k=1$) von 200 mK bestimmt werden.

Speziell für die Anwendung in der Radiometrie gefertigte Fixpunkte aus ZrC-C (2885 °C), TiC-C (2758 °C) und Re-C (2475 °C) mit einer großen strahlenden Öffnung wurden erstmalig mit radiometrischen Methoden mit einer Messunsicherheit ($k=1$) von unter 500 mK untersucht. Die gewonnen Ergebnisse sind essentiell für die Erweiterung der Temperaturskala oberhalb 1100 °C bis über 2800 °C. Mit diesen Fixpunkten wird es erstmals möglich sein, die Temperaturskala in diesem Temperaturbereich mit einer Interpolationsfunktion zu realisieren und damit die Messunsicherheit signifikant zu verringern.

Schlagworte:

Hochtemperaturfixpunkte, Metall-Kohlenstoff, Radiometrie, Strahlungsthermometrie, Thermometrie, Internationale Temperaturskala

The International Temperature Scale of 1990 (ITS-90) is defined by temperature fixed-points and interpolating measurement schemes. Up to now, in the high-temperature range above the freezing temperature of copper (1084 °C) long-term stable high-temperature fixed points are missing. Here, the extrapolation of the temperature scale to higher temperatures limits the principal uncertainty of the temperature scale. Novel fixed-points made from metal-carbon eutectics in a graphite crucible offer a solution, as their phase transition temperature can be as high as 3000 °C and they would allow using an interpolation function for temperature measurements between the fixed-points temperatures. The work presented investigates the potential of metal-carbon (M-C) eutectic fixed-points for radiation thermometry and radiometry. Measuring techniques were developed to determine the stability, reproducibility and the thermodynamic phase transition temperature of these fixed-points with lowest uncertainties using absolute radiometric methods.

For fixed-point cells of Co-C (1324 °C) , Pd-C (1492 °C) , Pt-C (1738 °C), Ru-C (1954 °C) and Re-C (2474 °C), manufactured by different laboratories, a reproducibility of less than ± 100 mK was observed. For the determination of the temperature during the phase transition a measurement scheme was developed that combines the best fixed-point design with the small measurement uncertainty of the radiometric temperature measurement using filter radiometers. Using this scheme, the melting temperature was determined for Co-C, Pd-C, Pt-C and Ru-C for the time with standard uncertainties ($k=1$) below 200 mK. The phase transition temperature of ZrC-C (2885 °C), TiC-C (2758 °C) and Re-C (2475 °C) has been determined for the first time with measurement uncertainties ($k=1$) below 500 mK using absolute radiometry and fixed-points cells especially designed for radiometric applications.

These results are essential for a revision of the temperature scale up to 2800 °C. For the first time it is now possible to realise a temperature scale above 1085 °C based on an interpolation function using fixed-points. Consequently, the measurement uncertainty will be reduced significantly.

Keywords:

High-temperature fixed-points, metal-carbon eutectics, radiometry, radiation thermometry, thermometry, international temperature scale

Contents

1	Introduction	1
2	Temperature measurement and temperature scales	5
2.1	Methods of primary temperature measurement	6
2.2	Practical temperature scales	10
3	Objectives	15
4	Sources of blackbody radiation: High temperature furnaces and M-C fixed points	17
4.1	Variable high temperature blackbodies	17
4.1.1	VEGA/HTBB type furnace	18
4.1.2	Nagano type furnace	20
4.2	Fixed-point blackbodies	22
4.3	Phase diagram of a metal-carbon eutectic alloy and the influence of impurities on the phase transition	28
5	Building M-C fixed points	37
6	Detectors of thermal radiation	45
6.1	Radiation Thermometer LP3	48
6.1.1	Stability at high temperatures	49
6.1.2	Solving the thermal drift problem	52
6.1.3	Size of source effect- SSE	54
6.2	Interference filter radiometers	57
6.2.1	Set-up and principal features of a radiometer for spectral irradiance	57
6.2.2	Radiometric calibration scheme	58
6.2.3	Diffraction at apertures	62
7	Scale comparison of three different ITS-90 realisations	67
7.1	Three different radiation thermometers and calibration schemes	67
7.2	Comparison of the high-temperature scales	69
7.3	Discussion	73
8	Evaluation of M-C eutectic fixed-points	75
8.1	A relative comparison Pt-C, Re-C in two non-identical furnaces	75

8.1.1	Description of the eutectic fixed-point blackbody cavities . . .	76
8.1.2	Description of the used furnaces and the installation of the fixed-points	77
8.1.3	Measurements	78
8.1.4	Results	80
8.1.5	Comparison uncertainty	82
8.1.6	Discussion	82
8.2	A relative comparison of Co-C, Pd-C, Pt-C, and Ru-C in two identical furnaces	87
8.2.1	Outline and set-up of the measurements	87
8.2.2	Repeatability of single cells/ effect of temperature steps on the melting	91
8.2.3	Relative temperature differences for one filling material	91
8.2.4	Discussion	93
8.3	Evaluation of two fixed-point cell designs for Cu, Pt-C and Re-C . .	95
8.3.1	Comparison of small aperture cells	95
8.3.2	Comparison of small and large aperture cells for Cu, Pt-C and Re-C	98
8.3.3	Comparison of radiation-thermometer vs. filter-radiometer measurements for LA cells	101
8.3.4	Discussion	101
9	Thermodynamic temperature determination of M-C eutectic fixed point cells	105
9.1	Measurements of thermodynamic temperatures using large aperture fixed-point cells of Re-C, ZrC-C and TiC-C	105
9.1.1	Measurements	109
9.1.2	Results	109
9.1.3	Conclusion	112
9.2	Thermodynamic temperature measurements of radiance cells by using an irradiance mode filter radiometer	115
9.2.1	Measurement principle	115
9.2.2	Measurement scheme	116
9.2.3	Stability measurements and SSE	117
9.2.4	Measurement Uncertainties	118
9.2.5	Results	119
9.2.6	Temperature differences between cells of one material	121
9.2.7	Thermodynamic temperature scale comparison	123
10	Investigation of the radiance distribution along the fixed-point aperture using a radiometric camera system	125
11	An investigation of the thermal annealing effect on the melting be- haviour of Co-C and Fe-C using differential scanning calorimetry	131

11.1	Manufacture of Fe-C and Co-C samples for DSC	132
12	Impact of metal-carbon fixed-points for thermometry, radiometry and photometry	135
12.1	Radiation thermometry	135
12.2	Radiometry and photometry	136
12.3	Contact thermometry	139
13	Summary	143
	Bibliography	147
A	Phase diagrams and physical properties of binary metal-carbon alloys	159
	Acknowledgement	165

List of Abbreviations

BIPM	<i>Bureau International des Poids et Mesures</i> , International Bureau of Weights and Measures (the international body responsible for metrology)
CCPR	<i>Comité Consultatif de Photométrie et Radiométrie</i> , Consultative Committee on Photometry and Radiometry (a consultative committee of the BIPM)
CCT	<i>Comité Consultatif de Thermométrie</i> , Consultative Committee on Thermometry (a consultative committee of the BIPM)
CGPM	<i>Conférence Générale des Poids et Mesures</i> , General Conference on Weights and Measures (held every 4 years at BIPM by representatives of the governments of all member states)
CIPM	<i>Comité International des Poids et Mesures</i> , International Committee for Weights and Measures (held every year by 18 individuals nominated by the CGPM)
DSC	Differential Scanning Calorimetry
FR	Filter radiometer
HTBB	High-Temperature Blackbody, a furnace type, e.g. BB3200pg of PTB
ITS-201X	New International Temperature Scale of 201X with M-C eutectic fixed-points
ITS-90	International Temperature Scale of 1990
LNE-INM/CNAM	.	<i>Laboratoire National de Métrologie et d'Essais - Institut National de Métrologie / Conservatoire National des Arts et Métiers</i> , France
LP2	Linearpyrometer 2, a radiation thermometer
LP3	Linearpyrometer 3, a radiation thermometer
M-C	Metal- carbon
MC-C	Metalcarbide-carbon
MEW	Mean effective wavelength
Nagano	A furnace manufacturer
NIST	<i>National Institute of Standards and Technology</i> , USA
NMI	National Metrology Institute
NMIJ	<i>National Metrology Institute of Japan</i> , Tsukuba, Japan
NPL	<i>National Physical Laboratory</i> , Teddington , United Kingdom
RTCR	Radiation thermometry cryogenic radiometer
SI	<i>Système International d'Unités</i> , International System of Units

SSE	Size-of-Source-Effect
Thermo Gauge	A furnace manufacturer
Topcon	A radiation thermometer
VNIIOFI	<i>All-Russian Research Institute for Optical and Physical Measurements</i> , Moscow, Russia
W-Re	Tungsten-Rhenium thermocouple

Parts of this work have been published in the following publications:

1. Anhalt, K., Hartmann, J., Lowe, D., Machin, G., Sadli, M., Yamada, Y., Thermodynamic temperature determinations of Co-C, Pd-C, Pt-C and Ru-C eutectic fixed-point cells, *Metrologia*, 43, 2006, pp. S78-S83
2. Anhalt, K., Hartmann, J., Lowe, D., Machin, G., Sadli, M., Yamada, Y., Bloembergen, P.(2005). A comparison of Co-C, Pd-C, Pt-C, Ru-C and Re-C eutectic fixed points independently manufactured by three different institutes. In: Gröbner (ed.), *Proceedings of Newrad 2005*, Davos, Switzerland, pp. 89-90
3. Yamada, Y., Khlevnoy, B. B., Wang, Y. F., Wang, T. J., Anhalt, K. (2006). Application of metal (carbide)-carbon eutectic fixed points in radiometry. *Metrologia*, 43(2), S140-S144
4. Anhalt, K., Hartmann, J., Machin, G., Sakuma, F., Lowe, D. (2005). Comparison of high temperature scales of the NMIJ and the NPL with the scale of PTB from 1300 K to 3100 K. In D. Zvizdic (ed.). *9th Int. Symposium on Temperature and Thermal Measurements in Industry and Science*. Dubrovnik, Croatia, pp. 1063-1069.
5. Anhalt, K., Wang, Y., Yamada, Y., Hartmann, J. (2008). Large- and small-aperture fixed-point cells of Cu, Pt-C, and Re-C. *International Journal of Thermophysics*, 29(3), pp. 969 - 983.
6. Lowe, D., Anhalt, K., Hartmann, J. (2008). Construction and validation of a platinum-carbon eutectic fixed point. *Metrologia*, 45(3), pp. 325-329
7. Khlevnoy, B., Sakharov, M., Ogarev, S., Sapritsky, V., Yamada, Y., Anhalt, K. (2008). Investigation of furnace uniformity and its effect on high-temperature fixed-point performance. *International Journal of Thermophysics*, 29(1), 271-284.
8. Machin, G., Anhalt, K., Hartmann, J., Lowe, D., Sasajima, N., Yamada, Y. (2005). A comparison of high temperature fixed-points of Pt-C and Re-C constructed by BIPM, NMIJ and NPL. In: D. Zvizdic (ed.). *9th Int. Symposium on Temperature and Thermal Measurements in Industry and Science*. Dubrovnik, 2004
9. Hartmann, J., Anhalt, K., Khlevnoy, B., Sapritskii, V. I., Sakharov, M. K., Ogarev, S. A., Hollandt, Jrg, Sperfeld, P. (2005). Thermodynamic temperature measurements of the melting curves of Re-C, TiC-C and ZrC-C eutectic irradiance mode fixed point cells. In D. Zvizdic (ed.). *9th Int. Symposium on Temperature and Thermal Measurements in Industry and Science*. Dubrovnik, 2004 (pp. 189 - 194). Zagreb, Croatia.
10. Hartmann, J., Edler, F., Anhalt, K. (2007). Neuartige eutektische Metall-Kohlenstoff-Hochtemperaturfixpunkte für die Thermometrie. *PTB Mitteilungen*, (3), pp. 256- 260

11. Hartmann, J., Anhalt, K., Hollandt, J., Schreiber, E., Yamada, Y. (2003). Improved thermal stability of the linear pyrometer LP3 for high temperature measurements within the EU-Project HIMERT. In: VDI (Ed.), Vol. 1784. Temperatur 2003. VDI Berichte (pp. 135-141). Duesseldorf, Germany: VDI.
12. Khlevnoy, B., Anhalt, K., Sakharov, M. K., Burdakin, M., Ogarev, S. A., Sapritsky, V. I., Yamada, Y., Sperfeld, P.(2006). New High-temperature furnaces for Metal (Carbide)-Carbon Eutectic Fixed Points. In: Phys.- Techn. Bundesanstalt(ed.), Temperatur 2006. Verfahren und Geräte in der Temperatur- und Feuchtemessung, Berlin, pp. 277-284
13. Edler, F., Anhalt, K., Hartmann, J. (2005). Novel fixed point cell design for simultaneous contact and non-contact temperature measurements. In D. Zvizdic (ed.). 9th Int. Symposium on Temperature and Thermal Measurements in Industry and Science. Dubrovnik, 2004 (pp. 936942). Zagreb, Croatia.
14. Anhalt, K. , Hartmann, J., Hollandt, J.(2008). Radiation thermometry capabilities of the PTB up to 3200 K. NCSLI Measure, 3(1), pp. 26-34

1 Introduction

The demand of science and industry for accurate and highly reproducible high-temperature measurements can often not be fulfilled due to an inherent limitation in the high-temperature part of the current International Temperature Scale of 1990 (ITS-90). Two outstanding examples are solar radiometry for predicting climate change and improvements to performance and safety of aeroplane jet turbine engines.

Solar radiation is the main energy source behind any form of life on our planet. The electromagnetic radiation coming from the sun, after being partly absorbed in the earth's atmosphere, does not only provide a habitable climate on earth, it drives bio-chemical processes as plants photosynthesis, and also the human eye-sight is adapted to the solar electromagnetic spectrum. A profound observation of solar radiating properties using precision radiometry plays a key role in order to understand global warming. The National Research Council of the US National Academy of Science estimated, that the sun's 11-year sunspot cycle causes a variation in solar irradiance of around 0.1 %, which for the years 1980 to 1986 is of the same order of magnitude as the effect of anthropogenic greenhouse gases on global climate [QF99], [Cou94]. Solar radiometry measures the radiance or irradiance variation of the sun, a hot object with a surface temperature of around 5500 °C, traceable to blackbody radiation. In the laboratory, however, hot artefacts can only be handled safely up to a temperature of about 2700 °C, and a difference of 0.1 % in spectral irradiance at a wavelength of 500 nm relates at 2700 °C to a temperature difference of only 0.5 °C, a challenging small quantity to measure.

Another striking example illustrating the importance of a precise high-temperature measurement for engineering processes is found in the next generation of aeroplane jet turbine engines, where the energy efficiency is aimed to be increased by running the rear part of the engine at higher temperatures compared to the front part [PMSF08]. Yet, such a process increases the thermal stress on the materials and new alloys are currently developed for this purpose. These materials require thermal annealing at a temperature of 1300 °C and only allow deviation from this maximum temperature of less than 3 °C. Without high-accuracy fixed-points available at these temperatures such a small deviation can not be obtained in the field.

These examples demonstrate the strong need for accurate temperature measurements in the high temperature range between 1000 °C and 3000 °C. The inherent limitation of the high-temperature part of the ITS-90 is the lack of suitable high-temperature fixed-points. In contrast to the temperature range below 1085 °C, where a large number of defining temperature fixed-points, represented by the phase tran-

sition of very pure elements, enables an interpolation function for the calibration of thermometers assuring lowest measurement uncertainties, for temperatures above the freezing temperature of Copper (1084.62 °C) presently any temperature scale realisation is principally limited by the absence of stable and reliable temperature fixed-points. The temperature scale on both contact and non-contact thermometers is presently extrapolated from the highest fixed-point during calibration leading to a measurement uncertainty of several °C at 3000 °C. The mechanical stability and impurity contamination from the crucible material limits the performance and accuracy of the currently available fixed-points using conventional materials at these high temperatures.

Resolving these inherent limitation of high-temperature measurements requires the development and characterization of novel fixed-point materials in the temperature range above 1085 °C. High-temperature fixed-points made from metal-carbon (M-C) eutectics show the unique potential to facilitate primary scale realisation and dissemination. Such fixed-points are innately independent from impurity intake from the crucible as the crucible itself is made from carbon which is also part of the eutectic alloy. Ideally, such fixed-points show a unique melting and freezing temperature, they are not subject to drift, are robust and can easily be transported.

Implementation of such metal-carbon fixed-point cells in any future temperature scale demands careful investigation to guarantee reproducible manufacture and optimized handling. Additionally, the temperature of the phase transformation must be determined with the lowest measurement uncertainties available to assure highest reproducibility and stability of the new cell materials.

The work on the characterisation on the M-C eutectics is embedded in a worldwide project on improving the high-temperature part of the ITS-90. In particular, in Europe the research was bundled within the European Union funded project "Novel high temperature metal-carbon eutectic fixed-points for radiation thermometry, radiometry and thermocouples - HIMERT". Partners cooperating within the project were NPL (UK), LNE-INM/CNAM (F), LNE (F), PTB (D), Universidad de Valladolid (E) supported by a collaboration with the NMIJ (J). The main tasks for the PTB in this project were the precise radiometric evaluation of different fixed-point cells and the radiometric measurement of the thermodynamic phase transition temperature. The scientific and metrological prerequisites together with the obtained results of these efforts are the topic of the present work. Basing upon the long-lasting experience in precise absolute radiometric temperature measurements at PTB further developments specially suited for radiometric measurements of high-temperature thermal sources have been developed for enabling the determination of the thermodynamic phase transition temperature of these high-temperature fixed-points above 1085 °C.

During a one year visit at the japanese metrology institute, the NMIJ, the manufacture of fixed-point cells of highest quality was studied. And in cooperation with the All-Russian Institute for Measurements in Optics and Physics, VNIIOFI, fixed-

points cell were investigated, that have been especially designed for applications in radiometry.

This work is organized in 12 chapters. First, concepts of temperature measurement and temperature scales are introduced (Chapter 2), then the objectives for this thesis (Chapter 3) are formulated. Chapter 4 deals with blackbodies as sources for thermal radiation, especially with fixed-points of metal-carbon and the properties of these eutectic alloys. The following chapter describes the manufacture of M-C fixed-points (Chapter 5). Methods for precise detection of thermal radiation by radiation thermometry and radiometry are the topic of Chapter 6, a temperature scale comparison for one of the detectors is presented in Chapter 7. The M-C fixed-points are analyzed with respect to reproducibility and repeatability (Chapter 8), then their thermodynamic temperature is determined (Chapter 9). The radiance distribution along the fixed point apertures was investigated by use of a camera system (Chapter 10) and the effects of thermal annealing using differential scanning calorimetry (Chapter 11). Finally, the impact of the novel fixed-points is illustrated for thermometry, radiometry and photometry (Chapter 12).

2 Temperature measurement and temperature scales

Temperature is one of the most frequently measured physical quantities, due to its influence on almost every biological, chemical and physical process. It determines the velocity of chemical reactions, the reproduction of living cells and the efficiency of thermal engines. And also human life strongly depends on temperature.

The importance of reliable temperature measurements for industrial processes was realized early and in 1927 the 7th CGPM ¹ decided to introduce an International Temperature Scale (ITS) to harmonize the world wide temperature measurements and to guarantee their comparability. At that time the ITS aimed to harmonize the development of individual national temperature scales.

In contrast to other base quantities of the International System of Units (SI) like length or mass, temperature is not additive. This means the temperature $2T$ cannot be realised by joining two systems of temperature T . This is why a temperature scale has to be defined for the measurement of temperatures. Using the freezing and the boiling point of water at standard atmospheric pressure (101.325 kPa) as reference temperatures, the swedish astronomer *Anders Celsius* defined a temperature scale in 1742 by dividing this temperature interval by 100 and the temperature unit degree Celsius (symbol °C) was defined. In 1854, *William Thomson*, later known as *Lord Kelvin*, proposed a new temperature scale based on the second law of thermodynamics using the absolute zero temperature and one additional temperature fixed-point. It was only until one hundred years later, in 1948, that the CGPM followed his proposal. As the defining temperature fixed-point the triple point of water was chosen, i.e. the temperature at which the solid, liquid, and gaseous phases of water are in equilibrium. The temperature of the triple point of water (TPW) was set to 273.16 K defining the temperature unit kelvin (symbol K) by

$$1 \text{ K} = \frac{1}{1/273.16} \cdot T_{\text{TPW}}. \quad (2.1)$$

From this definition it follows that temperature differences are exactly the same irrespective of whether the Kelvin or the Celsius temperature scale is used, while the absolute temperatures differ by 273.15 K. Temperatures measured according to the Celsius temperature scale are denoted as t , while temperatures measured by the

¹CCPM = Conférence Générale des Poids et Mesures

Kelvin temperature scale are referred to as T . Conversion of temperatures measured in degrees Celsius into Kelvin temperatures is made through

$$T/\text{K} = t/^{\circ}\text{C} + 273.16 \quad (2.2)$$

2.1 Methods of primary temperature measurement

In principle, any fundamental relation for the measurand incorporating temperature can be used for a temperature measurement. In metrology such a fundamental approach is called primary thermometry, and results in the measurement of the thermodynamic temperature of the object. In the following the most important methods are highlighted.

1. A well-known practical method is **constant volume gas thermometry** relying on the ideal gas law which relates the product of pressure p and volume V to the temperature T of the gas

$$pV = NkT \quad (2.3)$$

where k is Boltzmann's constant, the fundamental constant for statistical thermodynamics, and N is number of molecules in the gas. Typically a constant volume vessel filled with an ideal gas is operated at different temperatures and the pressure difference between the two temperatures is measured. This method forms the basis for the currently valid temperature scale ITS-90 in the temperature range up to 460 °C[ES89]. A variation of gas thermometry is the dielectric constant gas thermometry (DCGT). At low pressure p the permittivity of an ideal gas can be expressed as

$$\epsilon = \epsilon_0 + \alpha_0 N/V$$

(α_0 is the polarisability of a single gas atom). Then the equation of state for an ideal gas can be rewritten as

$$p = kT(\epsilon - \epsilon_0)/\alpha_0. \quad (2.4)$$

DCGT determines $\epsilon - \epsilon_0$ by measuring the change in electrical capacity for a gas-filled capacitor for different pressure levels. At PTB dielectric constant gas thermometry is used to measure Boltzmann's constant k aiming at a redefinition of the SI unit *Kelvin* based on Boltzmann's constant [FFBS05].

2. **Acoustic thermometry** relies on the relationship between speed of sound and temperature of an ideal gas. For an ideal gas the speed of sound c_0 can

be calculated for small amplitudes, not too high frequencies and an isotropic propagation according to

$$c_0 = \sqrt{\left(\frac{c_p}{c_0}\right)_{p=0} \frac{RT}{m}}. \quad (2.5)$$

Here c_p and c_v are the specific heat capacity at constant pressure or volume, respectively, and m the mass of a gas particle [Mol99, RDGM99].

3. **Noise thermometry** uses the Nyquist noise equation relating the mean square noise voltage $\langle u^2 \rangle$ in an electrical resistor to its temperature.

$$\langle u^2 \rangle = 4kTR\Delta f \quad (2.6)$$

Nyquist derived this equation from thermodynamic calculations valid for frequencies $\nu \ll kT/h$, where R is a frequency-independent resistance and δf the bandwidth [WGA⁺96, EKT04, NFET01, CA78].

4. At thermal equilibrium temperature not only determines the energy distribution of particles, but also the energy distribution of photons, the particles of light in the electro-magnetic radiation field. *Max Planck* provided with the discovery of the corresponding radiation law a solution for one of the fundamental problems of classical physics at the end of the 19th century and commenced the era of quantum physics. **Planck's law of thermal radiation** states that for a cavity with a uniform temperature inside and along its wall the spectral radiance L_λ for the vacuum wavelength λ is independent of the shape and material of the cavity walls and only dependent from λ , the temperature T

$$L_\lambda = \frac{2hc^2 \cdot n^{-2} \cdot \lambda^{-5}}{\exp\left(\frac{hc}{n \cdot \lambda \cdot k \cdot T}\right) - 1}, \quad (2.7)$$

where h stands for Planck's constant, c the speed of light in vacuum, n the refractive index of the gas inside the cavity, λ the wavelength in vacuum and k for the Boltzmann constant.

Max Planck derived this formula in 1900 assuming that the energy exchange of a blackbody wall to its surroundings is not continuous, instead he introduced here an energy quantum $h\nu$. With this radiation formula he could explain discrepancies in the spectral distribution of the black-body radiation measured at the Physikalisch- Technische Reichsanstalt by *Lummer* and *Pringsheim* [LE00] that differed from the at that time best theoretical description of the energy distribution in the black body spectrum derived by *Willy Wien*. Furthermore, with its first introduction of the concept of energy quantisation, it is today understood as the starting point of quantum physics.

While the spectral radiance can directly be calculated with Planck's law, integration over all wavelengths and solid angle 2π yields the Stephan-Boltzmann law for the total radiation L emitted by the cavity radiator

$$L = \int_0^{\infty} L_{\lambda} d\lambda = \frac{2\pi^5 k^4 n^2}{15h^3 c^2} \cdot T^4 \quad (2.8)$$

A suitable cavity radiator, also called blackbody or blackbody radiator, can be realized by electrically heated heat-pipes or, especially for temperatures up to 3000 °C, made from a graphite cavity set-up in a high temperature furnace. The energy distribution of the thermal radiation can then be observed nearly undisturbed via a small aperture in the cavity wall. The cavity's temperature can be determined by a radiometric measurement of the spectral radiance or total irradiance, respectively, and the use of an appropriate detector of known spectral responsivity.

The blackbody source introduced here for the first time, is a body that will absorb all incident electromagnetic radiation at all wavelengths and from all directions. A blackbody, when in equilibrium with its surroundings, must also be a perfect emitter, emitting exactly what it absorbs [Kir60].

Often Eq. 2.7 is used in a simplified form

$$L_{\lambda} = \frac{c_1 \cdot n^{-2} \cdot \lambda^{-5}}{\exp\left(\frac{c_2}{n \cdot \lambda \cdot T}\right) - 1} \quad (2.9)$$

with the values for the radiation constants c_1 and c_2 set in the text of the ITS-90 [PT90]

$$c_1 = 3.7417749 \cdot \text{Wm}^2, \quad (2.10)$$

$$c_2 = 0.014388\text{Km}. \quad (2.11)$$

Figure 2.1 shows the spectral radiance for several temperatures from room temperature (290 K) to the sun's mean surface temperature (5673 K). In order to achieve a sufficiently large radiance output from a blackbody in the visible wavelength region (380 nm to 780 nm) and in the UV (190 nm to 380 nm) the blackbody temperature must significantly exceed the freezing temperature of gold (1337.33 K). For short and long wavelengths two approximations of Planck's law can be deduced from classical physics. The Rayleigh-Jeans law describes the infrared spectral region and is valid for $hc/\lambda \ll kT$

$$L_{\lambda}(\lambda, T) = \frac{2ck}{\lambda^4} T. \quad (2.12)$$

For $hc/\lambda \gg kT$ Wien's approximation can be used in the form

$$L_{\lambda}(\lambda, T) = \frac{c_1}{\pi\lambda^5} \exp\left(\frac{-c_2}{\lambda T}\right). \quad (2.13)$$

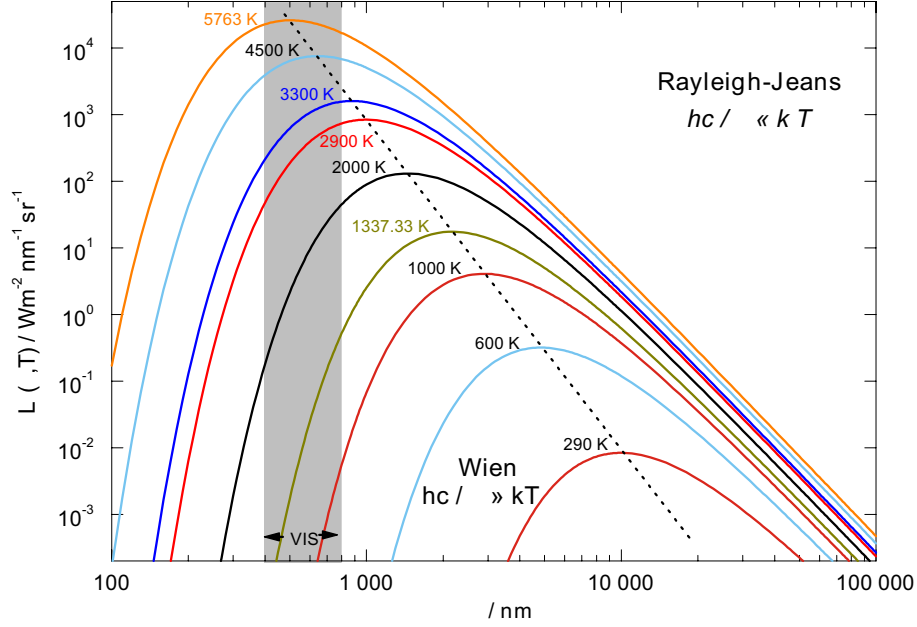


Figure 2.1: Spectral radiance of a blackbody radiator for different temperatures.

From Eq. 2.13 Wien's displacement law can be deduced, which gives for a temperature T the wavelength of maximum spectral radiance

$$\lambda_{max}T = 2.897768 \cdot 10^6 \text{ nm K.}$$

An ideal blackbody is a cavity in complete thermal equilibrium, with uniform temperature throughout and with only an infinitesimal small hole (in order to achieve an effective emissivity of one). Any real blackbody source will only be an approximation to this ideal source, mostly limited by the achievable temperature uniformity and lower emissivity. A high emissivity can be achieved first by choosing a suitable wall material or coating of high blackness. Secondly, by following design principles, so that any light reflected from the surface is reabsorbed by another part of the blackbody or is reflected back onto an absorbing surface.

For high temperature blackbodies the material options are often limited (i.e. materials that withstand high temperatures) and moreover emissivity depends on the blackbody internal temperature uniformity, the more uniform the temperature across the blackbody, the more it will be a true Planckian radiator.

The precise determination of the emissivity is one of the key problems in radiation thermometry and radiometry. A high emissivity is usually difficult to measure and, therefore, analytical or numerical models are used to calculate the emissivity of the blackbody [BM74][Pro98],[HT02]. A simple model for the

emissivity ϵ_{cav} of a cylindrical cavity radiator with length l , radius r and wall emissivity ϵ_{wal} was given by *Bauer and Bischoff* [BB71]

$$\epsilon_{cav} = \frac{\epsilon_{wall}}{1 - \epsilon_{wall} \cdot \frac{1}{1+l^2/r^2}} . \quad (2.14)$$

All temperature measurement methods relying on such fundamental thermodynamic equations measure the absolute or thermodynamic temperature T . In contrast to this most practical temperature measurements rely only on an approximation to the thermodynamic temperature, such practical temperature scales are described in the next section.

2.2 Practical temperature scales

The fundamental primary temperature measurement techniques described in the last chapter are often too complex, time-consuming and expensive for practical everyday temperature measurements. Furthermore, even the best gas thermometer shows less reproducibility than the platinum resistance thermometer over most of its range [Qui91]. For these reasons, in 1927 the CGPM passed a detailed description of a temperature measurement technique based on a number of reproducible temperatures, so called fixed-points, to which numerical values of thermodynamic temperatures were assigned. The CGPM also defined the interpolating standard instruments that were to be calibrated at these fixed-points. Such a scheme was first proposed by the british physicist H.L. Callendar in 1899 [Cal99] to meet the everyday demand for reliable, simple to use and world wide comparable temperature measurements in science and industry.

This detailed set of instructions was called the International Temperature Scale of 1927 (ITS-27). The International Temperature Scale is revised from time to time, by this taking account of scientific and technological progress in order to ensure that the temperatures measured according to the valid scale are the closest possible practical approximation of the corresponding thermodynamic temperatures. Currently valid is the International Temperature Scale of 1990 (ITS-90) [PT90]. Also for the ITS-90, the basis is provided by a set of temperature fixed-points which are embodied by phase transitions of pure materials and the triple points of water, argon and neon. These provide highly reproducible and stable temperatures, which can be used as reference temperatures for the calibration of temperature measurement devices. The thermodynamic temperatures of these phase transitions have been accurately measured by applying one of the above-mentioned fundamental temperature measurement techniques. Besides the temperature fixed-points, the ITS-90 also describes the instruments to be used for measurement between the defining fixed-point temperatures. Paragraph 3 of the text of the ITS-90 [PT90], which gives an outline of the scale, is repeated here:

Fixed-point		T_{90}/K	$t_{90}/^{\circ}\text{C}$	$\Delta T/\text{mK}$
He	vapour pressure point	3 to 5	-270.15 to -268.15	0.3
e-H ₂	triple point	13.8033	-259.3467	
e-H ₂ (or He)	vapour pressure point	17	-256.15	
e-H ₂ (or He)	vapour pressure point	20.3	-252.85	
Ne	triple point	24.5561	-248.5939	0.5
O ₂	triple point	54.3584	-218.7916	1
Ar	triple point	83.8058	-189.3442	1.5
Hg	triple point	234.3156	-38.8344	1.5
H ₂ O	triple point	273.16	0.01	0
Ga	melting point	302.9146	29.7646	1
In	freezing point	429.7485	156.5985	3
Sn	freezing point	505.078	231.928	5
Zn	freezing point	692.677	419.527	15
Al	freezing point	933.473	660.323	25
Ag	freezing point	1234.93	961.78	40
Au	freezing point	1337.33	1064.18	50
Cu	freezing point	1357.77	1084.62	60

Table 2.1: Defining fixed-points of the ITS-90. All substances except ³He are of natural isotopic composition, e-H₂ is hydrogen at the equilibrium concentration of the ortho- and para-molecular forms. Additionally, estimates of the (k=1) uncertainty ΔT of thermodynamic temperature of some of the defining fixed-points of ITS-90 is stated [Qui91].

Between 0.65 K and 5.0 K T_{90} is defined in terms of the vapour-pressure temperature relations of ³He and ⁴He.

Between 3.0 K and the triple point of neon (24.5561 K) T_{90} is defined by means of a helium gas thermometer calibrated at three experimentally realizable temperatures having assigned numerical values (defining fixed-points) and using specified interpolation procedures.

Between the triple point of equilibrium hydrogen (13.8033 K) and the freezing point of silver (961.78°C) T_{90} is defined by means of platinum resistance thermometers calibrated at specified sets of defining fixed-points and using specified interpolation procedures.

Above the freezing point of silver (961.78°C), T_{90} is defined in terms of a defining fixed-point and the Planck radiation law.

The defining fixed-points of the ITS-90 are listed in Table 2.1.

Temperatures measured according to the ITS-90 are denoted by T_{90} when given in Kelvin, resp. t_{90} when given in °C. T_{90} and t_{90} are only approximations, though rather good ones, of the thermodynamic temperature T . Although any possible difference between T and T_{90} is very small, and at the moment not significant for most industrial and scientific applications, in the temperature range from 13.8033 K

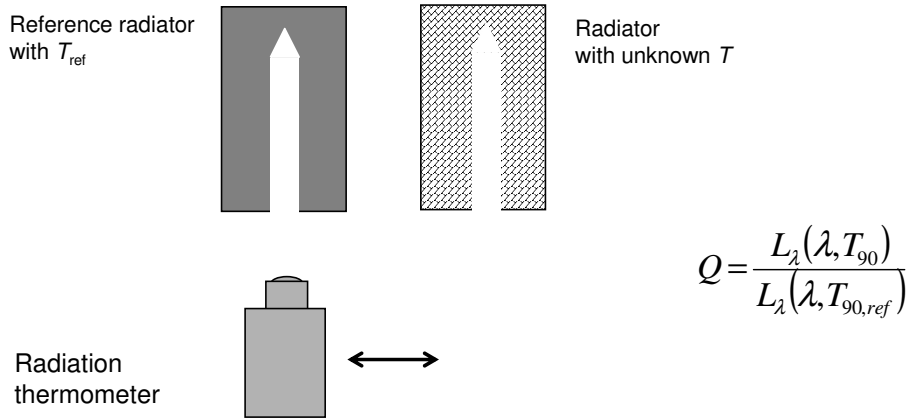


Figure 2.2: Above the freezing temperature of Al, Au or Cu a temperature T_{90} is defined by a spectral radiance ratio measurement using a radiation thermometer.

to 1234.93 K the standard uncertainty of the ITS-90 with respect to the thermodynamic temperature extends to 40 mK at the freezing point of silver, to 50 mK at the freezing point of gold and to 60 mK at the freezing point of copper (see Table 2.1) [Qui91].

For temperatures above the freezing point of silver, the uncertainty increases still further, since above this temperature, due to the lack of stable and reproducible fixed-points, the ITS-90 is based on extrapolation. In this temperature range a temperature T_{90} is determined by a spectral radiance ratio measurement relative to one of the ITS-90 fixed-points of silver, gold or copper

$$\frac{L_{\lambda}(\lambda, T_{90})}{L_{\lambda}(\lambda, T_{90,\text{ref}})} = \frac{\exp(c_2/[\lambda \cdot T_{90,\text{ref}}]) - 1}{\exp(c_2/[\lambda \cdot T_{90}]) - 1}. \quad (2.15)$$

Here, c_2 is the second radiation constant, with the value given in Equation (2.11). This measurement technique is illustrated in Figure 2.2.

And the uncertainty of the reference temperature of the silver, gold or copper fixed-points propagates according to [Jun86] with

$$u\left(\frac{T_{90}}{T_{90,\text{ref}}}\right) = \left(\frac{T_{90}}{T_{90,\text{ref}}}\right)^2 u(T_{90,\text{ref}}). \quad (2.16)$$

With Eq. (2.16) and the expanded standard uncertainty of the thermodynamic temperature of the gold or copper fixed-point (100 mK and 120 mK, respectively) a theoretical limit of the measurement uncertainty according the ITS-90 can be calculated and is shown in Figure 2.3.

The principal limit for the expanded standard uncertainty of the ITS-90 extrapolates from 100 mK at the gold fixed-point and 120 mK at the copper fixed-point to

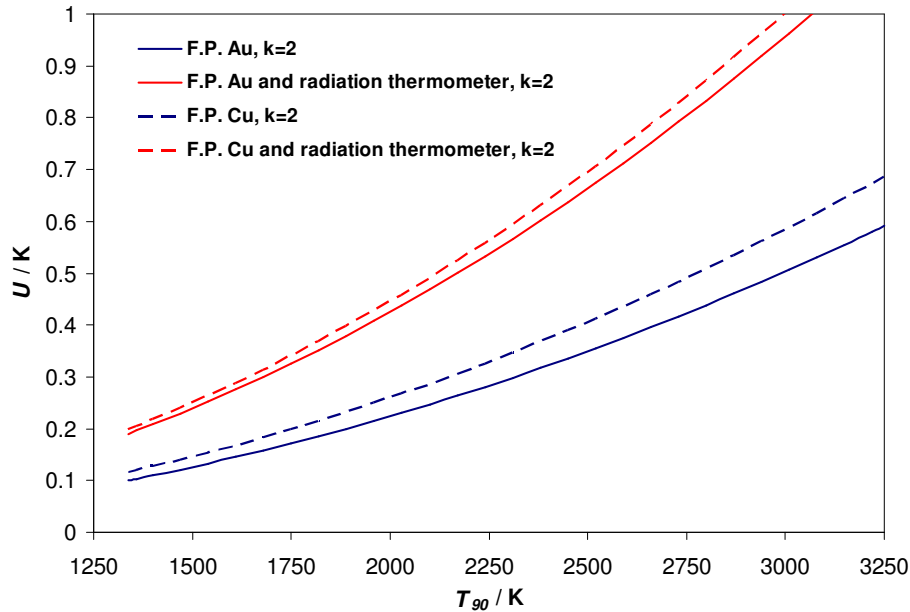


Figure 2.3: Theoretical and practical limit for the expanded measurement uncertainty U according to the ITS-90 when extrapolating from either the gold or the copper fixed-point (F.P. Au or F.P. Cu). For the practical limit a radiation thermometer with an effective wavelength of 650 nm and a calibration uncertainty of 0.2% was considered.

600 mK (Au) and 700 mK (Cu) at 3250 K. This principal uncertainty limit is further increased by the additional uncertainty contribution introduced by the inevitable radiation thermometer necessary to perform the measurements. An instrument's expanded standard uncertainty of 0.2 % for a typical high-quality radiation thermometer working at an effective wavelength of 650 nm will increase the uncertainty in temperature measurement to more than 1.5 K.

Additional high-temperature fixed-points with well-known thermodynamic temperatures, that prove to be reproducible and stable to within 100 mK, will significantly improve practical temperature measurements above the freezing point of copper. This work investigates the use of metal-carbon eutectic alloys as high-temperature fixed-points and such additional fixed-points would enable an interpolating scale above the freezing point of silver, gold and copper, reducing the measurement uncertainty drastically.

Pure metal fixed-points as the freezing points of nickel (1728 K), iron (1811 K), palladium (1828 K), platinum (2041 K), rhodium (2236 K), iridium (2719 K), molybdenum (2895 K) and tungsten (3687 K) have been recommended above the freezing temperature of copper as secondary temperature reference points [BBMP96]. However, for the practical use of such fixed-points problems arise from the contamination of the pure metal with the material of the fixed-point crucible, which leads to a modification of the fixed-point temperature, e.g. by dissolved graphite from the crucible.

Eutectic	Approximate temperature/K	Approximate temperature/°C
<i>Metal-carbon</i>		
Fe-C	1426	1153
Co-C	1597	1324
Ni-C	1602	1329
Pd-C	1765	1492
Rh-C	1930	1657
Pt-C	2011	1738
Ru-C	2227	1954
Ir-C	2564	2291
Re-C	2747	2474
<i>Metal carbide-carbon</i>		
TiC-C	3034	2761
ZrC-C	3155	2882
HfC-C	3458	3185

Table 2.2: Metal-carbon and metal carbide-carbon eutectics and their approximate fixed-point temperature.

Instead, alumina was proposed as an alternative crucible material for some of the metals above [KGK00, JT76, Jon79, KGK99]. However, alumina crucibles tend to be too fragile for practical use and what is of special concern to radiation thermometry: alumina crucibles have a lower emissivity compared to graphite crucibles and are transparent in the long wavelength range [MMB]. For thermocouples, calibration at high temperatures can be done using the wire bridge method [PT90]. And also alumina itself has been proposed as a fixed-point material (ca. 2320 K) realized in a tungsten crucible [SSO95].

However, none of these materials proved to be stable and reliable enough to be used as part of a high-temperature fixed-point in thermometry. Therefore, the consultative committee for temperature (CCT) of the *Comité International des Poids et Mesures* (CIPM) encouraged National Metrology Institutes in 1996 to develop high temperature fixed-points at temperatures above 2300 K with reproducibilities better than 100 mK and to improve the techniques of absolute radiation thermometry [Qui97]. In 1999 *Yoshiro Yamada* of the NMIJ² proposed, that binary eutectic alloys of metal and carbon might provide a solution to the contamination problem. Carbon is here integral part of the eutectic alloy and a purified graphite crucible will not contaminate the fixed-point material. Subsequent research has shown that a series of metal-carbon and metalcarbide-carbon eutectics have potential as fixed-points in the region from 1426 K to 3453 K.

²NMIJ = National Metrology Institute of Japan

3 Objectives

While the fixed-points made from metal-carbon eutectic alloys promise a significant reduction of the measurement uncertainty and simplify the necessary efforts for a precise temperature measurement above the freezing temperature of copper (1084 °C), the implementation into a new and extended temperature scale ITS-201X requires additional research to be able to design, manufacture and use these fixed-points to their full capacity. Especially, low uncertainty temperature values need to be assigned to the respective phase transition temperatures.

From the late 1990s the successful manufacture of M-C eutectic fixed-point cells has been reported by several institutes such as the NMIJ [YSSO99, Yam01, Sas02], the NPL [MYL⁺, LM04] and the VNIIOFI [SOK⁺03], and also comparisons between fixed-point cells have been reported [YDB⁺01, MYL⁺]. However, these first comparisons were often hindered by large uncertainty contributions due to considerable drift of the radiation thermometers or an unexpected large furnace effect. As a consequence the measurement uncertainty was considerably larger than the temperature differences between the fixed-point cells. Up to the beginning of this thesis, the phase transition temperature of the eutectic alloys has only been measured according to ITS-90, with relatively large measurement uncertainties. But the required low measurement uncertainties can only be achieved by applying absolute radiometric methods. Here, PTB has a long tradition of measuring directly thermodynamic temperatures in the temperature range below 1000 °C using filter radiometry. Via Planck's law of thermal radiation thermometric fixed-points can also be utilized for radiometry [SOK⁺03, Yam05]. Such fixed-points can serve as stable artefacts for the realization of radiometric quantities as spectral radiance or spectral irradiance. However, a typical set-up for the measurement of spectral irradiance sets special requirements on the design of the fixed-point cell and the equivalence between different fixed-point cell designs has to be analysed.

This thesis aims at the investigation of M-C eutectic fixed-points by means of radiometry and radiation thermometry in order to prove their suitability for an improved temperature scale. The challenging task of developing and characterising such novel high-temperature fixed-points requires the solution to a number of provoking scientific and technological problems.

This includes, that the stability, reproducibility and the phase transition temperature have to be determined with the lowest possible measurement uncertainty. The cell design and cell manufacture has to be studied and advanced to guarantee a reproducible, universally valid temperature value for the phase transition. For this

objective, fixed-point cells have to be manufactured using highly pure materials and then the performance of these M-C eutectic fixed-point cells must be investigated and if necessary optimized. In detail this requires the following:

- Fixed-point cells of Cu, Pt-C and Re-C need to be manufactured with two different designs, one optimized for radiation thermometry and the other for applications in radiometry, and their performance needs to be evaluated in detail (chapter 5 and chapter 8.3).
- High-temperature graphite furnaces have to be characterized and optimized for the use as fixed-point furnaces, this includes the measurement of the temperature uniformity inside the furnace (Chapter 4.1).
- The repeatability and reproducibility of the fixed-point cells needs to be approved by comparing cells manufactured independently by different institutes, here a relative measurement scheme guarantees lowest measurement uncertainties (Chapter 8).

These preparatory tasks are an essential prerequisite for the main objective of this thesis, the thermodynamic temperature measurement of the phase transition of metal-carbon alloys.

The investigations of the above mentioned fixed-point properties require the development and application of improved and novel measurement schemes for such high temperatures, namely

- The characterization and improvement of a standard radiation thermometer LP3 by optimizing the optical filter design to gain a better high-temperature stability of the instrument (Chapter 6), and the validation of the improved instrument by applying it in several bi-national comparisons of temperature scale realisations (Chapter 7).
- Novel radiometric methods need to be designed, characterized and optimized, as only absolute radiometric methods can be used to measure such high temperatures with the required low uncertainties. For the direct traceability to the primary detector standard of the PTB, the radiation thermometry cryogenic radiometer RTCR, filter radiometers need to be selected and specially designed for the absolute radiometric temperature measurement (Chapter 6.2).
- Not only temperature metrology, but also radiometry will greatly benefit from such stable and well characterized fixed-point blackbodies. Consequently, the usability of M-C eutectics in radiometry needs to be investigated (Chapter 9.1). As radiance and irradiance measurements vary in the field of view on the aperture and bottom of the fixed-point cell, the differences observed between the two measurement techniques are studied by the use of a photometric camera system (Chapter 10).

4 Sources of blackbody radiation: High temperature furnaces and M-C fixed points

Practical realisation of blackbody sources are commercially available and widely used in radiation thermometry and radiometry as reference sources for temperature radiation. With known temperature, determined either by radiation thermometry or radiometry at selected wavelengths, and the known effective emissivity such furnaces are used as primary realisation or transfer source for both radiation temperature and spectral radiance/ irradiance over a wide wavelength range [Spe98, Yin01, Fle66, SKK⁺97, Sap96, Car03, Khl01b], as the spectral radiance can be calculated using Plancks law of thermal radiation (eq.(2.7)). Different furnace types were experimentally used within this work, out of them, the two blackbody furnaces available at the PTB, the HTBB3200pg and the Nagano-Chino, are described in the following sections. These furnaces were not only used as blackbodies itself, furthermore they can be used to operate M-C eutectic fixed point cells by installing the eutectic cell into them, so that the actual blackbody is then formed by the fixed point cell. Both of these furnaces can in principal be operated vertically and were used to manufacture metal-carbon fixed point cells.

Other furnaces systems, such as the Thermo Gauge [Bro97] used e.g. at the NPL or specific variants of the above HTBB-Vega and Nagano-Chino used e.g. at the NMIJ, are described in the experimental part of this work with references to literature only.

At the end of the chapter fixed-point blackbody sources are presented. The radiating cavities here are generally much smaller compared to variable temperature blackbodies. With a suitable length to diameter ratio of the cavity a high emissivity can be achieved and the dimension can be chosen to match the area of best temperature uniformity in the furnace these fixed-point radiators will be installed to.

4.1 Variable high temperature blackbodies

All high temperature blackbody furnaces presented here comprise as central part a graphite cavity. Graphite withstands high temperatures and has a relatively high emissivity. The two furnaces described in the following, however, use different forms of graphite making use of their specific physical properties.

4.1.1 VEGA/HTBB type furnace

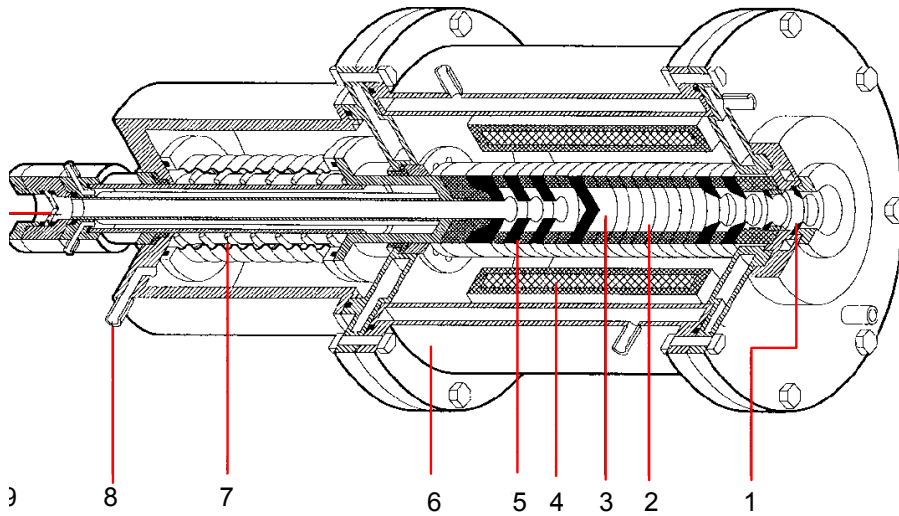


Figure 4.1: The High Temperature pyrolytic graphite blackbody BB3200pg: **1** output aperture of the radiator, **2** pyrolytic graphite rings forming the cavity, **3** bottom of the cavity, **4** thermal insulator, **5** baffles in optical path for thermal shielding, **6** water-cooled housing, **7** clamping spring, **8** inert gas purge inlet, **9** rear quartz window

The HTBB (**H**igh-temperature **blackbody**) 3200pg was designed and manufactured by the All-Russian Institute for Opto-physical Measurements, VNIIOFI, as a blackbody radiator with a long lifetime for temperatures up to 3200 K with maximum radiance stability and uniformity over a sufficiently large output area (see Fig. 4.1). Its heater and blackbody is made from rings of pyrolytic graphite, an anisotropic form of graphite made by decomposing a hydrocarbon gas in a vacuum furnace at very high temperatures [LLK67]. In comparison to normal graphite, pyrolytic (pg) graphite has a higher density and as a consequence a ten times lower sublimation rate for temperatures between 2800 K and 3200 K, which makes it more robust at high temperatures. Pyrolytic graphite specimens are available as plates grown to a thickness of 5 mm- 10 mm. These plates possess an explicit layered structure in which the planar graphite crystals are orientated normal to the growth direction of the plates. From these, pyrolytic graphite plates rings are cut, with the symmetry axis of the rings coinciding with the growth direction. The electrical properties of the pyrolytic graphite rings are strongly anisotropic. Thermal and electrical conductivities perpendicular to the furnace axis (the growth axis of the pyrolytic plates) are substantially higher than along the furnace axis [Del01].

A clamping spring arrangement fixes the ring set in the furnace and guarantees a reliable electrical contact between them. An electrical current going through the rings via the front flange and the back electrode is heating the furnace, thus

flowing perpendicularly to the rings graphite layers, and therefore in the direction of maximum electrical resistance.

The individual rings differ in thickness and thermal and mechanical history which results in a variety of values for each rings specific electrical resistance, a property that can be measured [KOS⁺07] and used to arrange the pyrolytic rings such that the highest resistance rings, which will be most efficiently heated, are located at the front and end of the cavity, which is naturally cooled by radiation loss. In order to improve the temperature uniformity baffles from graphite and pyrolytic graphite can be installed into the furnace tube.

The BB3200pg has a 45 mm thick heat insulation shield in order to protect the housing and to improve the temperature uniformity along the length of the cavity. The housing, and the front and back-flange are made from stainless steel and are water cooled. A special design was developed at the PTB for the housing and the front back flanges that ensures a guided water flow and avoids welding connections at the inner sides of these parts, which face the hot furnace. The rear electrode is made from copper and also water cooled. A flexible woven copper wire connection allows the electrode to glide as the heater tube expands by about 10mm/1000°C.

The whole furnace can be evacuated and when used is purged by Ar gas at a flow rate of 4 l/min to prevent oxidization of the graphite parts at high temperatures.

Compared to a furnace tube made from normal graphite such a radiator made from pyrolytic graphite rings has a

- higher total electrical resistance (pyrolytic graphite has a low specific electric conductivity along the furnace axis),
- lower temperature gradient in the main part of the radiating cavity (pg has a low thermal conductivity along furnace axis, this produces a higher radial gradient from the cylindric water cooled housing to the centre,
- equalization of the temperature field because of pyrolytic graphite's negative coefficient of specific electric conductivity.

The consumed power amounts to 14 kW at 3200 K, with an electrical current of around 600 A DC at a voltage drop across the furnace of around 25 V .

For temperature control a pyrometer viewing from behind and through the rear electrode can sense the temperature in the furnace. The output signal is used to control the power supply via a PID control software on a PC.

The specific electrical resistance for the pyrolytic graphite rings varies across the heater. As the cavity is made up out of around 40 pyrolytic rings, the position of individual rings can be changed in different configurations. By measuring the electrical resistance of the rings and arranging the heater according to their resistances can help to improve the temperature uniformity. In other words, putting higher-resistance rings towards the end of the heater is likely to compensate for the heat loss towards the colder environment and flattens the temperature gradient in

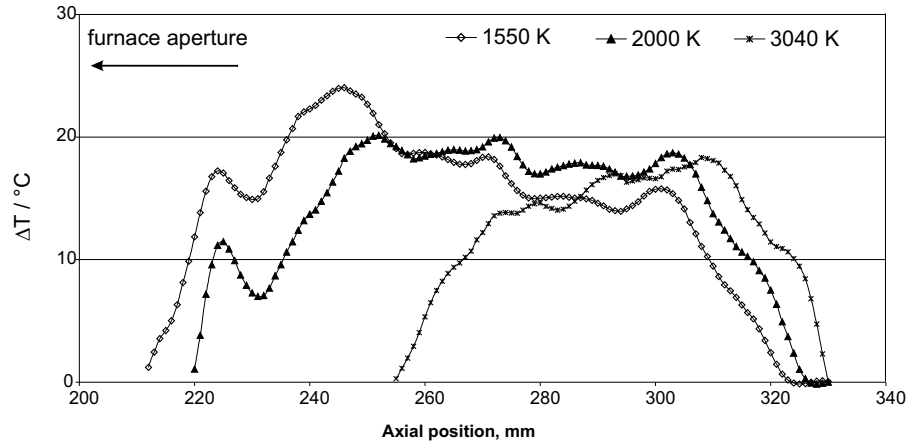


Figure 4.2: Temperature distribution along the cavity wall of the HTBB3200pg

the central part of the cavity. An apparatus was constructed to measure the specific electrical resistance. This apparatus consists of two massive water-cooled metal electrodes, and a pyrolytic heater ring between them, by which a current of about 20 A is applied perpendicular to the ring plane. The voltage drop across a pair of pin electrodes is then measured on the outer surface of the heater ring. Arranging the rings according to their thermal resistance can help improving the temperature uniformity: i.e. higher thermal resistance rings at the ends to compensate for the heat losses. Details on the improvements to the temperature uniformity of this type of furnace can be found in [KSO⁺08].

The temperature distribution can be measured using various techniques either by scanning the furnace temperature with a radiation thermometer, or for temperatures up to 1500 °C using a thermocouple. Here, a tilted radiation thermometer was used to measure the heated cavity over a length about 200 mm around the centre of the furnace. For this the front lens of the radiation thermometer was equipped with an aperture of 10 mm in diameter in order to reduce the risk of vignetting at the entrance of the furnace and thereby to maximize the scan width. For 1550 K, 2000 K and 3040 K the result is shown in diagram 4.2. With increasing furnace temperature, the temperature uniformities worsens and the hottest part is pushed to the rear side of the furnace. This is related to the heat losses from the front opening of the furnace, which is most efficiently cooling the front part of the heated cavity.

4.1.2 Nagano type furnace

Another commercial furnace system that was used in this work is the Nagano high temperature furnace. Two versions of this furnace were used: the Nagano

M [YSGS02] and the smaller Nagano S ¹. The first allows temperature and fixed point measurements up to 2800 °C the latter due to its smaller size and insulation only up to 2000 °C.

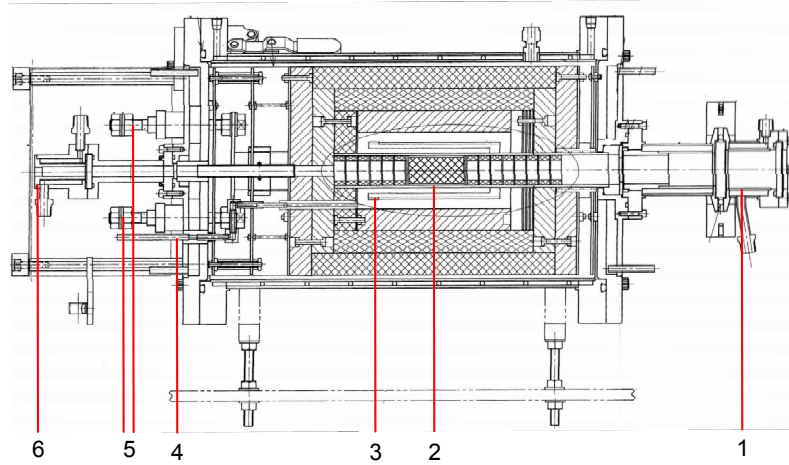


Figure 4.3: Nagano M type single zone C/C composite heater furnace: **1** front flange with removable purge unit and quartz window, **2** C/C furnace tube, which can hold C/C baffles and fixed point cell, **3** C/C composite heater element, **4** purge gas inlet, **5** rear electrodes, **6** quartz window with attached fibre-optic radiation thermometer

The single-zone heater for both furnaces is made from a cylindrical C/C composite material ². The C/C composite material enables the furnace system size, including furnace, power supply and controller, to be of reasonable dimensions. C/C composite heaters can be made to a thickness of approximately 2 mm, while still being strong enough to withstand thermal shocks, and thus enabling a high voltage- low current operation. This has the advantage that the power cables and transformer can be kept within reasonable size. However, with high voltage an electrical spark is more likely to incite between the heater and the graphite insulation.

The heater in Figure 4.3 forms a meander and needs to be mechanically fixed only on the back side of the furnace, where the electrodes are placed. Inside the heater a C/C furnace tube of 27 mm inner diameter can hold fixed point crucibles or can be used as a blackbody cavity. Discs from graphite felt and C/C material can easily be placed into the furnace tube to improve the temperature uniformity. A fibre-optic radiation thermometer from the back side is used to control the furnace temperature. For temperatures up to 2000 °C the furnace is purged with Ar gas to prevent oxidation of the graphite parts. For higher temperatures the inner parts, heater and furnace tubes, can additionally be purged with He to prevent electrostatic discharges or sparks, as He has a 1.5 times higher ionization potential [Bro66]. The

¹Nagano S = VR 10-A20, Nagano M = VR 10- A24

²C/C-composite=Carbon-fibre-reinforced-carbon-composite

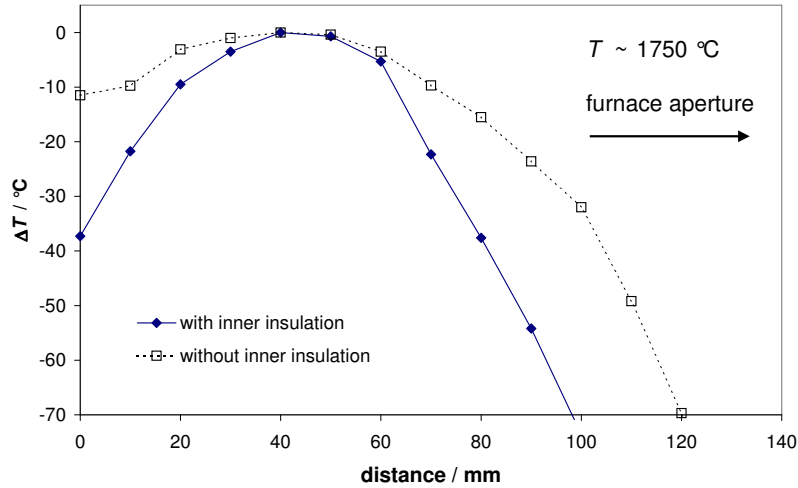


Figure 4.4: Temperature distribution along the furnace axis for a Nagano type furnace

thermal conductivity of helium however is about a magnitude higher than for Ar-gas, in a pure He environment the furnace could not reach highest temperatures. Therefore, only the inner part of the furnace is purged with He, while Ar is still used for the outer parts at temperatures above 2000 °C. Typically 3-4 l/min of each gas are used.

For evacuation of the whole furnace the front side is closed with a glass window that can be removed for precise measurements at high temperatures, it is replaced by a purge unit that allows to reduce the risk of oxygen entering the furnace by actively purging the front opening with N₂. For temperature control both a feedback radiation thermometer that senses the temperature from the rear through a quartz window at the furnace bottom and a W-Re thermocouple positioned from the side of the water cooled housing into the furnace can be used.

The temperature uniformity inside the furnace was measured using a miniature graphite blackbody probe, that was moved along the furnace axis. For a furnace set-temperature of around 1750 °C the result is shown in Figure 4.4. Here, a better temperature uniformity can be achieved by removing parts of the cylindrical graphite-felt insulation. Then, the larger volume inside the furnace improves the radiation exchange between the furnace parts.

4.2 Fixed-point blackbodies

The blackbody furnaces above can all be used over a wide temperature range, yet the precise blackbody temperature itself still has to be measured with a calibrated contact or radiation thermometer.

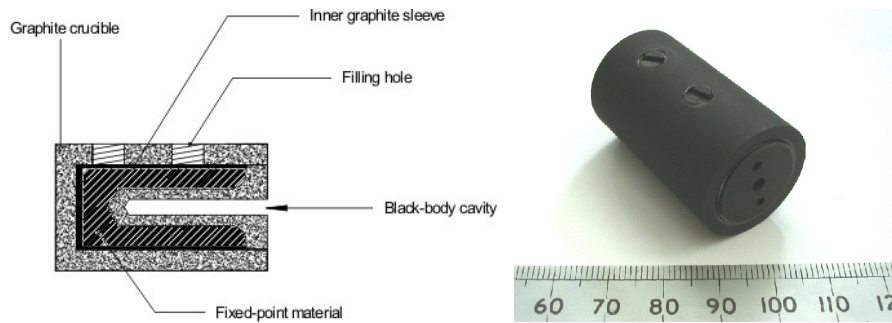


Figure 4.5: Fixed point blackbody cell as designed by the NPL. The metal is brought into the crucible through filling holes on the side.

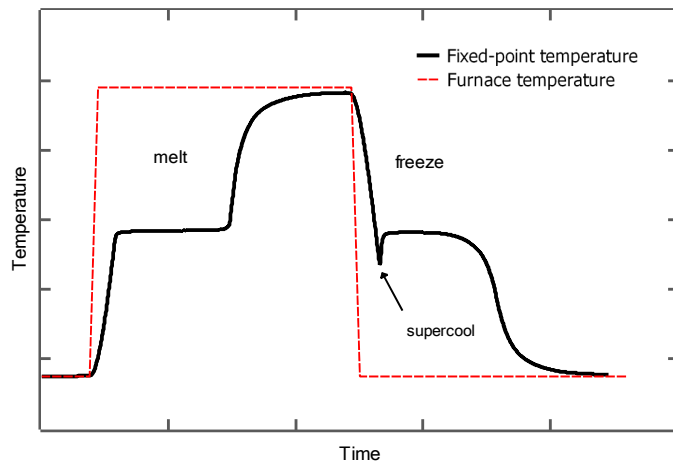


Figure 4.6: A temperature plateau indicates the phase transformation.

For a metal with known melting temperature a blackbody with known temperature can be built by immersing a blackbody cavity into the metal. At the phase transition temperature from liquid to solid, the cavity walls will then all be at the same temperature. Such a design can be realized by either pressing the cavity into a hot crucible filled molten metal, as it is often done for Al and other conventional fixed points. Alternatively a fixed point design is used, where the cavity is solidly connected to the crucible. The void between crucible and cavity is then filled with metal powder or flakes and successively molten.

Such a fixed-point blackbody can be installed into the furnaces above and used as a fixed point radiator for radiation thermometry and radiometry at its phase transition temperature. With the cell design presented in Figure 4.5, various metal fixed point radiators can be realized. The typical emissivity of such a blackbody design is around 0.9996.

Melt and freeze cycles of eutectic fixed-points (and of thermometric fixed-points generally) are typically initiated by placing the crucible at room-temperature inside

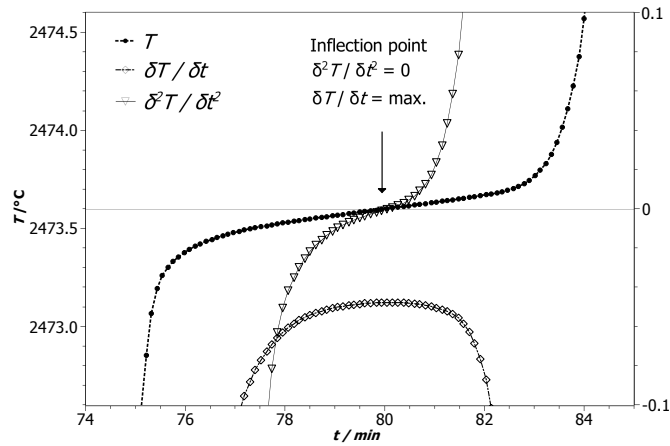


Figure 4.7: Inflection point of the melting plateau for a Re-C fixed-point cell

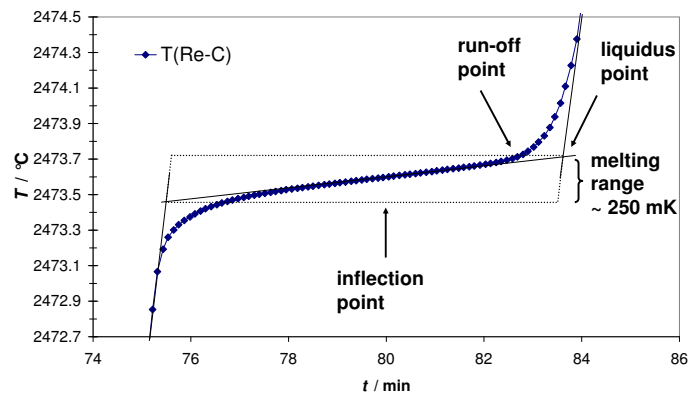


Figure 4.8: Characteristic temperature points used to describe and analyse the melting plateau

a furnace, whose temperature is slowly increased until a few ten degrees below the melting temperature of the eutectic material. Then, after keeping this temperature a few minutes for good thermal homogeneity and subsequently increasing the furnace temperature in a step or ramp above the melting temperature, the melt can be observed as a plateau in the cavity's temperature vs. time diagram. Ideally, the melt finishes at a so-called run-off or break-off point with a sharp temperature rise from the plateau to the set temperature of the furnace. The furnace is then held a few minutes at the higher temperature above the freezing temperature. Consequently, when the temperature is then reduced below the freezing point, the freeze is observed, usually after undergoing a supercool. Fig. 4.6 illustrates the observed melting and freezing plateaus in dependence from the furnace temperature settings.

The smallest temperature steps, that can be used for initiating the phase transformations depend strongly upon the furnace and its thermal uniformity in the desired temperature range. If the temperature step is too small (or the furnace uniformity is not sufficient) the melting plateau will have a larger gradient (i.e. the melt will be

measured over a wider temperature range) and will not show a pronounced break-off at the end of the melt. The unique fixed-point temperature should be defined by the liquidus point - the temperature at which the last solid melts. In practice a direct measurement of the liquidus point temperature is obstructed by the presence of impurities [FH06]. Before it is reached the remaining solid shell is pierced by pre-melted channels along the grain boundaries, which settled during the preceding freeze, and make up the so-called mushy zone [PE04]. These channels enable a direct thermal contact with the cavity, which is thus no longer protected all around by the latent-heat barrier. Therefore for metals the preferred route to the liquidus point is to initiate a freeze from the liquid state which is free from structural features, which might be influenced by thermal history. However for freezing at the liquidus point a supercooling is needed to trigger nucleation and the supercooling temperature required can become a considerable temperature deviation to the system. Also furnace effects, as described below, can curve the final rise out of the melting plateau and hinder a direct determination of the liquidus point temperature. A solution is found in using the inflection point of the melting curve as a reproducible indicator of the melting temperature, see Figure 4.7.

For an ideal fixed-point the inflection point during the melt is found to be a repeatable temperature, independent from the furnace conditions and the temperature steps used to initiate the phase transition. In this work this quality of fixed-point cells is assessed by comparing 3 or 4 melting curves of the same fixed point cell in the same furnace. The standard deviation of these temperature values is called *repeatability* and it can be as low as a few mK for good fixed-point cells. Figure 4.9 shows this inflection point temperature for three melting plateaus of a Pt-C fixed-point cell at a temperature of around 2000 K. Although the furnace was operated at different start and end temperatures to melt the fixed-point material the repeatability of the inflection point during the melt is within ± 30 mK.

Indicators for cell quality and plateau shape are a small melting range, i.e. the temperature range of the melting plateau with limited slope around the inflection point and the length plateau duration. Both reduce the uncertainty for determining the point-of-inflection of the melting plateau. For best cells a melting range of around 200 mK can be achieved with a plateau length of up to 15 minutes. Ideally, the melting plateau should end with a clear run-off point, after which the temperature increases steeply and with constant slope.

An example for the effect of a non-ideal temperature distribution inside the furnace on the fixed point cell is shown in Figure 4.10. Here, the same Pt-C fixed-point cell was installed in a Nagano type furnace at two different positions. The temperature uniformity of this furnace is shown in Figure 4.4, first the 45 mm long cell was installed in a zone with a minimum temperature gradient of around 5 K, then the cell was moved to a position where the temperature shows a gradient of several 10 K. A shortened melting plateau is observed for the cell with the larger temperature gradient, yet, the curved temperature rise indicates, that the melt is not completely finished after the run-off point. The shortened plateau will remove the point of

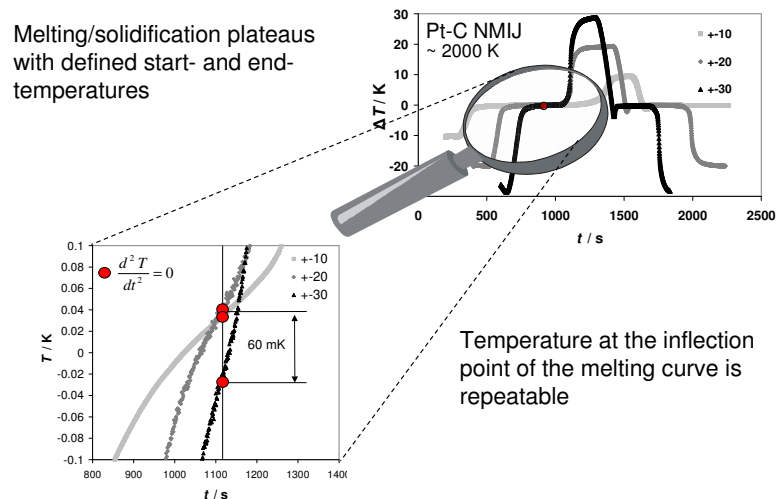


Figure 4.9: The inflection point of the melting plateau is a repeatable temperature

inflection towards colder temperatures and away from the liquidus point. Thus, a lower melting temperature will be measured. Smaller sized cells are generally more tolerant of furnaces that have a short uniform zone and should therefore be preferred. For certain radiometric applications a larger cell design is necessary and as will be shown in Chapter 9.1 and Chapter 8.3 the observed plateaus are then generally of poorer quality.

Apart from showing a repeatable temperature for a single fixed-point cell, the unique temperature should be reproducible by another fixed-point built with nominally the same material. This fixed-point property is called *reproducibility*. In this work fixed-points manufactured in different laboratories using different material suppliers and fixed-point designs are compared in order to show the achievable agreement. This work investigates a special type of fixed point blackbody cells that are filled with eutectic metal-carbon alloy. Chapter 5 shows the cell filling procedure for two selected cell designs in more detail. In the following section the physico-chemical details of the eutectic metal-carbon phase transition are discussed.

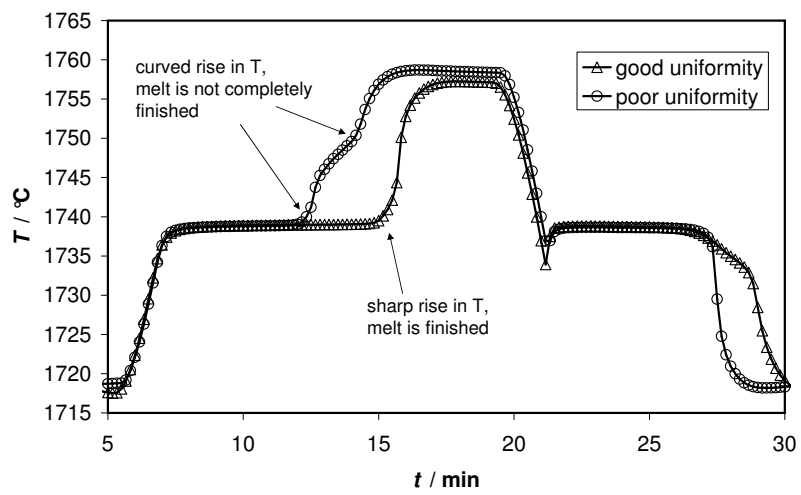


Figure 4.10: Furnace effect: A non-ideal temperature uniformity effects the plateau shape of a Pt-C fixed-point cell.

4.3 Phase diagram of a metal-carbon eutectic alloy and the influence of impurities on the phase transition

Metal-carbon fixed-points are based on the observation, that in the eutectic alloys phase diagram a lowest temperature exists for the liquid phase at a particular composition of metal and carbon.

Whenever a pure element or compound can exist both as crystalline solid and a liquid, there is a temperature, T_E , at one pressure value, above which the liquid is the stable form of the material, and below which, the solid is stable. The temperature so defined is also called *melting point*, it is the only temperature at which the crystalline solid and the liquid can coexist in equilibrium.

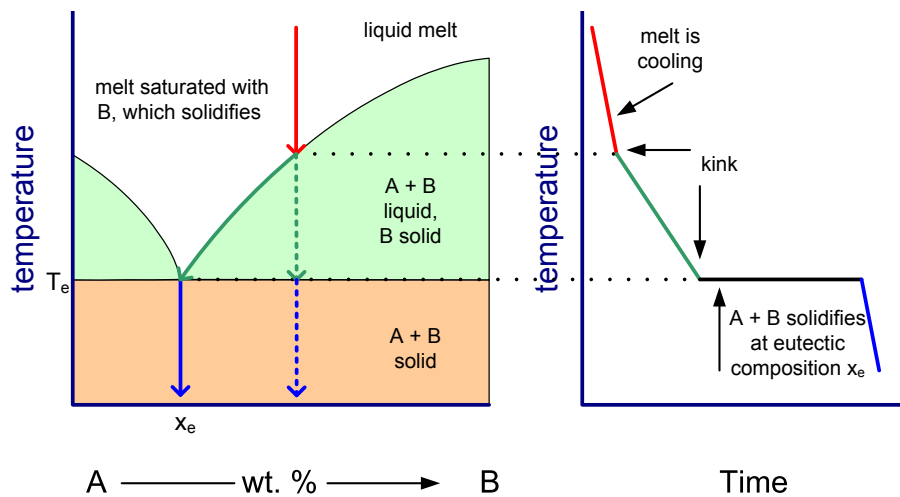


Figure 4.11: Phase diagram of a binary eutectic alloy and a typical freezing curve for a composition enriched in B

For alloys, e.g. of constituents A and B, the melting temperature generally depends upon the composition of the alloy, the concentration of A and B. For each composition of the liquid there is a temperature, the *liquidus temperature*, at which it is in equilibrium with the appropriate solid, and conversely a *solidus temperature* is defined. In an equilibrium phase diagram that plots liquidus temperature as a function of composition this effect is known as a curve, the liquidus or solidus line.

A special equilibrium relationship exists for the case where two materials A and B are completely soluble in the liquid and not soluble in the solid phase. Then an eutectic point occurs at the intersection of the two liquidus lines L_A and L_B which slope in opposite directions. At the eutectic point for a fixed composition and temperature the liquid is in equilibrium with the two different solid phases. From the *phase rule*

$$P + F = C + 2 \quad (4.1)$$

where P is the maximum number of phases present in the system at equilibrium, F is the number of degrees of freedom³ and C is the number of components in the system. For a binary alloy ($C = 2$) at the eutectic point, the liquid, two solid phases, and the vapour are all in equilibrium, $P = 4$, $C = 2$ and $F = 0$ follows; which means for the eutectic transition a unique composition and temperature exists.

The fact that the eutectic composition occurs at the intersection of two liquidus lines with opposite slope implies, that it has the lowest liquidus temperature of any liquid in the part of the phase diagram between the neighbouring maxima.

Metal-carbon fixed-points in a graphite crucible are taking advantage of this characteristic as it makes the fixed-point immune to contamination from the crucible material. This is illustrated in Figure 4.11. If a melt is cooled with a composition enriched in one component B, the additional material freezes out, the composition changes along the liquidus line with decreasing temperature and the slope of the freezing curve changes. When the eutectic composition is reached the whole sample, the eutectic, freezes and a temperature plateau is observed, which will last until all the eutectic mixture is frozen.

The eutectic morphology is characterized by the simultaneous growth of two phases from the liquid and a wide variety of micro-structures for binary eutectics alloys can be observed in the solid.

For most eutectic alloys the constituents differ greatly in their volume (and mass) fraction. The uniform distribution of both atoms A+B is separated into discrete areas of A and B during solidification. This makes clear that eutectic growth is largely a question of diffusive mass transport.

The structures can be classified as lamellar, rod type, discontinuous, regular and irregular and various variations. An overview can be found in [KF98],[Pfa78],[Cha64]. A lamellar structure with lamellae α and β is typical for eutectic alloys. During eutectic solidification, two solutes are rejected into the liquid: Solute A in front β lamellae, solute B in front of α lamellae and the solutes diffuse along the solid/liquid interface from one phase to the other. Thus, solute diffusion plays an important role. With decreasing lamellar spacing the solute concentration in front of the liquid/solid interface is also decreasing, and as a consequence a finer structure forms. Phase boundaries are connected with excess free energy. Therefore, a finer structure is connected with a larger area between the two phases. Thus, surface energy acts to increase lamellar spacing. An optimum lamellar structure exists under specific growth conditions with respect to the solute diffusion and surface energy. A deviation from the equilibrium spacing will be connected with a deviation from optimum, e.g. the presence of impurities results in an adjustment of lamellar spacing

³the number of parameters such as pressure, temperature, and composition that can be varied independently of each other



Figure 4.12: Micrograph of Fe-C

by creation of new lamellae or terminations until the new spacings become stable. Naturally such a lamellar scenario requires an even partition of molecules A and B in the volume. When one phase has only a small volume fraction a rod-type (fibrous) structure is more probable to form [Pfa78].

Examples for eutectics with even partitioned constituents are Pb-Sn and Al-Cu. Such eutectics are also called regular or non-faceted/non-faceted eutectics, both phases have a low entropy of fusion. With large differences in the entropy of fusion of the two phases, the binary eutectic is called anomalous, irregular or faceted/non-faceted. Metal / non-metal eutectics like Fe-C or Al-Si are examples for anomalous eutectics [KF98],[Ell83].

A micrograph of the anomalous Fe-C structure is shown in Fig. 4.12.

During eutectic solidification, the driving force for transformation is defined by the local undercooling ΔT , with contributions from thermal undercooling, solutal undercooling and curvature undercooling.

When the two phases, α and β , grow simultaneously from the liquid during freezing, α segregates B and β segregates A. This results in concentration (composition) gradients of components A and B ahead the liquid/solid interface, and a diffusion controlled solutal mass transport is necessary to continue the growth of α and β phases. However, a finer structure with short diffusion length and fast energy dissipation (fast crystal growth) increases the overall surface energy (which tends to prefer a wider lamellar structure).

For an ideal, normal eutectic, the lamellar distance can be determined. The B concentration enrichment in front of the α lamellae is related to a diffusion current j_B to the β lamellae and vice versa.

$$j_B = 2D_L \frac{\Delta c_L}{S/2} \quad (4.2)$$

$$\Delta c_L = c_{L\alpha} - c_{L\beta} \quad (4.3)$$

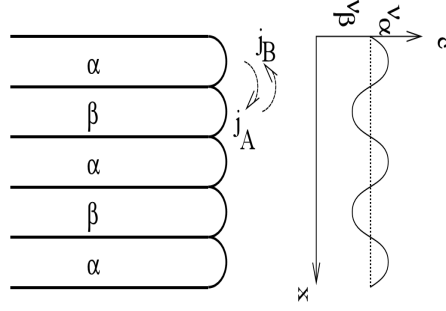


Figure 4.13: Schematics of the eutectic structure.

with D_L the diffusion coefficient of B atoms in the liquid, S is the lamellar spacing, $c_{L\alpha,\beta}$ the concentration of B atoms in front of an α or β lamellae. The diffusion length shortens with decreasing lamellar spacing. On the other hand additional surface energy has then to be compensated and this limits lamellar spacing. This additional energy has to be compensated by an thermal undercooling

$$\delta T_1 = \lambda_1 \cdot \frac{E_{\alpha\beta}}{S} \quad (4.4)$$

The diffusion current due to the concentration gradient can also be expressed as an undercooling

$$j_B = 4D_L \frac{\Delta c_L}{S/2} = (c_L - c_\alpha) \cdot v, \quad (4.5)$$

where v is the velocity of the advancing freeze front. This follows, because of the need to transport the non-segregated B atoms away from the α lamellae.

$$\Delta c_L = \frac{c_L - c_\alpha}{8D_L} \cdot S \cdot v \quad (4.6)$$

ΔT_2 is the undercooling necessary to form this concentration gradient.

$$\Delta T_2 = \lambda_2 \Delta c_L \quad (4.7)$$

In summary the melt has to be undercooled by

$$\Delta T = \Delta T_1 + \Delta T_2 \quad (4.8)$$

$$\Delta T = \lambda_1 \cdot \frac{E_{\alpha\beta}}{S} + \lambda_2 \frac{c_L - c_\alpha}{8D_L} \cdot S \cdot v \quad (4.9)$$

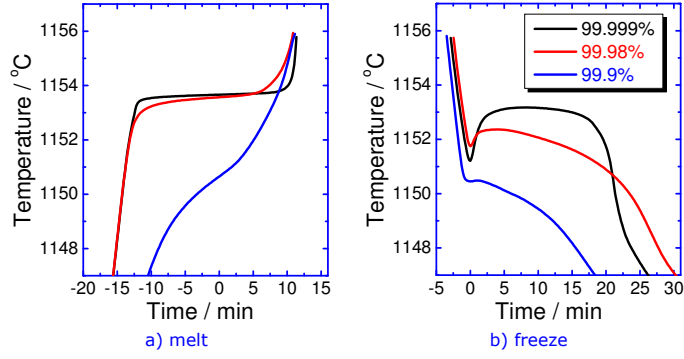


Figure 4.14: The effect of impurities on the melting freezing plateau of Fe-C. [YSGS02]

in order to freeze with a velocity v and lamellar spacing S . For a specific undercooling ΔT is then

$$v(S) = \frac{8D_L}{\lambda_2(c_L - c_\alpha)8D_L} \frac{1}{S} \left(\Delta T - \lambda_1 \frac{E_{\alpha\beta}}{S} \right) \quad (4.10)$$

and the lamellar spacing with the fastest grow rate will develop $\frac{\delta v}{\delta S} = 0$ (extremum criterion).

For an anomalous eutectic the situation is more complex due to the limited abilities of faceted phase for branching. Branching is needed for growth at the extremum lamellar spacing.

Although any fixed-point in precision thermometry should be manufactured using the purest substances available, trace impurities will always be present in any fixed-point to some extent.

The effect of impurities on the phase transformation of a metal-carbon fixed-point was investigated in a number of theoretical and experimental studies [SYB03] [Sas02] [YBS⁺02]. Figure 4.14 illustrates the effect of different purity grades for the Fe source material on the plateau formation of Fe-C fixed-point cells.

The impurities can either originate from the supplier of the pure materials or can be introduced during the fixed-points filling process. Generally, any impurity will have an effect on the phase transformation of the pure substance. This effect should be evaluated in the fixed-points temperature uncertainty budget. However the exact value of this effect is difficult to evaluate, due to the lack of reliable impurity analysis and also due to insufficient knowledge of the involved chemical reactions and their process parameters. This section aims to provide an understanding of the principal effects that are connected with impurities for the phase transformation of a pure substance.

For an ideal dilute solution the effect of impurities can be estimated from the slope of the freezing curve following Raoult's Law. Such an ideal dilute solution requires the impurities to be un-soluble in the solid phase and completely dissolved in the liquid

phase. [Fel03],Magnum]. In such a rare case the difference between the temperature of the ideally pure fixed-point substance T_{pure} and of the observed sample T_{sample} can be determined by Raoult's Law [Fel03]

$$\Delta T(F) = T_{pure} - T_{obs}(F) = c_0/F \cdot A \quad (4.11)$$

where F is the liquid fraction of the observed sample, A is the first cryoscopic constant, and c_{11} the total impurity concentration. At $F = 1$ (the liquidus point) the temperature will be shifted by the impurities by $\Delta T(F = 1) = c_{11}/A$. However, for most fixed-point substances at least a few impurities are soluble in the solid phase and the segregation of these impurities during the freezing is in first approximation described by the equilibrium distribution coefficient $k_0 = c_s/c_l$, where c_s and c_l are mole fraction concentrations of the impurity in the solid and liquid equilibrium phases of the sample, respectively. For low impurity concentrations the relation between the equilibrium distribution coefficient of each impurity, $k(x)$, and the liquidus slope induced by each impurity, $\alpha(x)$ [K/molfraction] is known as the van't Hoff relation:

$$\alpha(x) = \frac{k(x) - 1}{A}. \quad (4.12)$$

The main problem, however, is to know the equilibrium distribution coefficient for each particular impurity, which is difficult due to

- insufficient knowledge of binary and ternary phase diagrams for low impurity concentrations,
- melting and freezing conditions, which are normally not at the thermodynamic equilibrium.
- effect of freezing conditions on the magnitude of k , e.g. freezing rate or degree of mixing in the molten state [Pfa78].

The value of k_0 can be less than or greater than unity, depending on whether the impurity intake lowers or raises the melting point of the substance (see Figure 4.15).

For $k < 1$ the melting temperature of the fixed-point metal is lowered by the impurity and the impurity concentration in the liquid is higher than in the solid. For $k > 1$ the impurity increases the melting point of the fixed-point metal and the impurity concentration in the liquid is then lower than in the solid. Such concentration differences lead to a segregation of impurities in the melting and solidification process. The segregation of impurities determines the shape of the melting and freezing plateaus and at the same time micro-structure that forms.

A simple segregation model that describes the diffusion processes during the phase transformation is the Scheil-Gulliver Solidification model (SGS). The model assumes that there is only diffusion of impurities in the liquid phase and that this diffusion

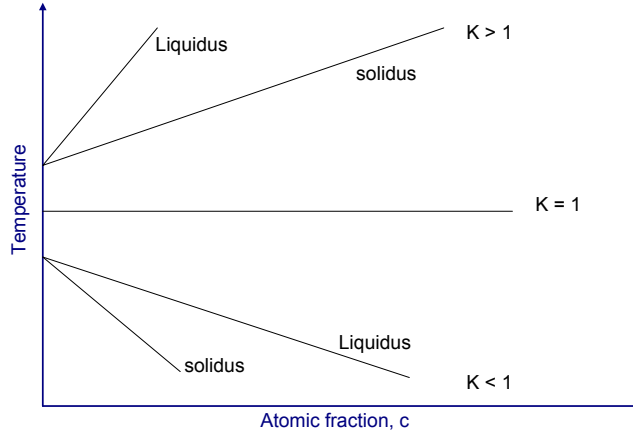


Figure 4.15: The effect of an impurity with distribution coefficient $k > 1, k = 1, k < 1$ on the melting point of a solid. In each case the lower line, the *solidus*, gives the melting point as a function of composition, the upper line, the *liquidus* curve, gives the freezing point as a function of composition. Both lines merge for $k=1$.

is instantaneous (and that there is no diffusion in the solid). It is represented by the Scheil equation

$$c_l(x) = c_0(x) \cdot F^{k(x)-1}, \quad (4.13)$$

where $c_l(x)$ is the concentration of the impurity x in the liquid phase, $c_0(x)$ is the overall concentration, F the liquid fraction and $k(x)$ the equilibrium distribution coefficient.

A graphical representation of the model is given in Fig. 4.16. The assumption of no diffusion in the solid imposes an impurity gradient into the solid phase of the freezing fixed-point. Also this results in a varying temperature shift ΔT induced by the impurity concentration at the liquid fraction F :

$$\Delta T = \alpha(x) \cdot c_0(x) \cdot F^{k(x)-1}. \quad (4.14)$$

4.14 can be used to model the effect of impurities on the fixed-points plateau shape, by calculating the plateau shape for a given impurity concentration. Such a model can then be compared with experimental studies.

As in a real fixed-point always several different impurities are present, each with different equilibrium distribution coefficients, the total influence can be calculated by adding the particular influence of all the impurities. And with 4.14 follows

$$\Delta T = \sum_i \alpha(x_i) \cdot c_0(x_i) \cdot F^{k(x_i)-1}. \quad (4.15)$$

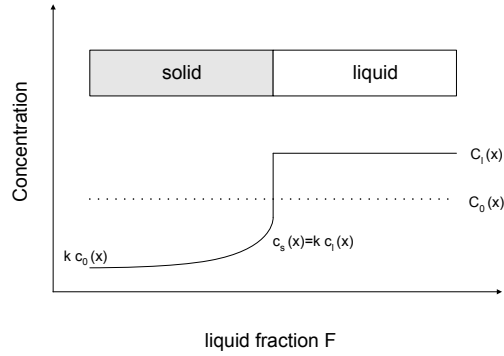


Figure 4.16: Graphical representation of the Scheil Gulliver model. No diffusion of impurities in the solid results in a impurity concentration gradient with the advancing solid liquid interface.

This approach to determine the influence of impurities on the liquidus temperature is also called *sum of individual estimates* **SIE** [BY06],[FH06]. It is noteworthy that its calculation does not require knowledge of the full transition curve in order to correct for the effect of small amounts of impurities. Only the liquidus slopes with regard to the detected impurities are required. However, for a practical calculation using SIE not all process parameters and material constant might be available. Then the *Overall maximum estimate* **OME** allows an estimate for the bound of the impurity influence on the liquidus point temperature

$$|\Delta T_{OME}| = \sum_i ((k_i - 1)/A) \cdot x_i. \quad (4.16)$$

It does so by assuming an ideal solution of impurities in the liquid, upper and lower bounds for k_i (e.g. $0 < k_i < 2$ for metal fixed-points considering that for zone refined fixed-point materials impurities with equilibrium distribution coefficients are effectively removed) and an evenly distribution of k_i between k_{min} and k_{max} . For a calculation of the influence of impurities on the liquidus temperature using OME the concentration of the involved impurities has to be fully specified. The required impurity levels for the metal-carbon system for a temperature difference of 1 mK and 10 mK between the pure and the contaminated system are shown in Table 4.1 [BY06].

System	ΔT / mK	Purity (molefraction)
Fe-C	10	0.999988
	1	0.999999
Co-C	10	0.999987
	1	0.999999

Table 4.1: Required purity levels for an influence on the liquidus temperature below 1 mK and 10 mK, calculated using OME. From: [BY06].

5 Building M-C fixed points

Metal (carbide)-carbon (M(C)-C) eutectics fixed-point cells establish themselves as highly reproducible, stable and useful tools in radiation thermometry with the advancements in cell manufacture and better understanding of furnace effects on their performance (see Chapters 8.1 and 8.2).

For those fixed points exceeding 2500 K, there is special interest in the extension of their application to radiometry. Such applications, e.g. for direct measurements of spectral irradiance, require fixed-point cells with a large aperture, preferably exceeding 9 mm. Such cells had been specially designed and tested for VEGA black-body (BB) furnaces [SOK⁺03]. With their wide inner furnace tube these furnaces could hold M(C)-C eutectic fixed-point cells with the dimensions needed to maintain a high emissivity even with the large radiating aperture. However, such large-aperture fixed-point cells were found to be of poorer quality with wider melting ranges and non-ideal plateau shapes during the phase transformation compared to the commonly achievable realisations of small-aperture fixed-point cells used in radiation thermometry, typically of 3- or 4-mm aperture diameter, see Chapter 9.1. Subsequent investigation to improve temperature uniformity in the BB furnace showed that indirect radiative heating of the cells with additional thermal insulation surrounding the cell holder improves the plateau quality for a 3-mm-aperture cell [KOS⁺07]. A preliminary result of an attempt to apply this method to a Re-C eutectic point (2474 °C) large-aperture cell with an 8-mm aperture was reported in [YWS06]. Here, the large aperture cell retains the outer diameter of 24 mm so as to fit in the same holder as the small-aperture cell. However, the observed plateau was far from ideal.

In this chapter further investigations on the large-aperture cells for radiometry are described, again with the same outer diameter as the small-aperture cells. An improvement to the filling method was experimentally attempted, and the differences in performance between large- and small-aperture cells are studied systematically. Finally, measurements by radiation thermometers and filter radiometers, in irradiance mode, are compared.

Two types of cells are employed in this investigation, the small-aperture (SA) cell, and the large-aperture (LA) cell. Three fixed points are studied: Re-C eutectic (2747 °C), Pt-C eutectic (1738 °C) and Cu (1084.62 °C) points, and for each type two SA and one LA cells are involved. Material used came from the same supplier for each fixed-point type, but the production lot were different for the two SA cells (with the exception of Re), and the same for one SA cell and the LA cell.



Figure 5.1: The fixed point cell is filled from the back with the end cap removed. Two layers of C/C sheet are used for thermal and mechanical insulation of the metal alloy from the graphite crucible. The C/C sheet sticks out of the crucible in order to facilitate filling and to protect the graphite threads (left). The cell is filled with a mix of metal-carbon powder at the eutectic composition (centre). The ingot of the filled cell is covered with two additional layers of C/C material (right).

For all cells one to three layers of 0.5-mm thick "C/C sheet" (manufactured by Toyo Tanso Co. Ltd, TCC-019) purified carbon cloth material were placed inside the fixed-point cells between the crucible outer wall and the metal to optimize the temperature uniformity and to reduce the risk of cell breakage [YKW⁺06]. Carbon fibre reinforced graphite foil (C/C foil) is used between the fixed-point metal and the crucible wall for thermal insulation and to reduce the mechanical stress on the fixed point cell caused by differences in the thermal expansion coefficient between alloy ingot and graphite crucible during heating and cooling. The C/C foil shows an anisotropic thermal conductivity, which helps to uniform the temperature gradient along the cylindrical axis of the crucible and it has a flexible, woven structure. It is cut into tightly fitting pieces, just big enough to guarantee one or two layer of C/C material between the crucible and the alloy. And, since this material is initially cut longer than the length of the crucible forming a tube sticking out of the crucible like a funnel. This protects the graphite threads of the crucible and enlarges the volume available for filling with the low density metal powder, thus simplifying the filling process and reducing the filling steps necessary. Figure 5.1 illustrates the use of the C/C inside the cell.

The principal cell design is shown in Fig. 5.2.

Small-aperture (SA) cells The SA cell design is displayed in Figure 5.2. The outer diameter is 24 mm, and the length is 45 mm. The crucible has a cavity with an aperture diameter of 3 mm, and length of 33 mm, with a conical bottom shape with an apex angle of 120°. The wall thickness of the cavity is 2 mm. The emissivity

of the cavity was calculated to be 0.9997. The space between the crucible inner wall and the cavity outer wall, which is filled with the C/C sheets and the ingot, is 4.5 mm. The filling procedure for the fixed-point cells followed the well established routine at the National Metrology Institute of Japan (NMIJ) [8] using a vertical version of the common Nagano M as filling furnace (Nagano VR20-A10), which is exclusively used for the filling of fixed-point cells.

Large-aperture (LA) cells The LA cell design is presented in Figure 5.2 and is the same as the cell in [YKW⁺06]. The crucible has a 24 mm outer diameter and a length of 100 mm. The cavity has a diameter of 8 mm and a length of 89 mm. The shape was designed to be similar to the cavity of the SA cell in order to achieve the same effective emissivity. The cavity wall has a thickness of 2 mm. The required large cavity aperture in connection with the crucible's outer diameter of 24 mm restricts the outer graphite walls of the crucible to a thickness of 2 mm. The thickness of the metal ingot plus the thickness of the C/C sheet around the cavity is 4 mm.

With this design altogether six fixed point cells were filled for Cu, Pt-C and Re-C, for each metal one small aperture cell (SA) and a large aperture cell (LA).

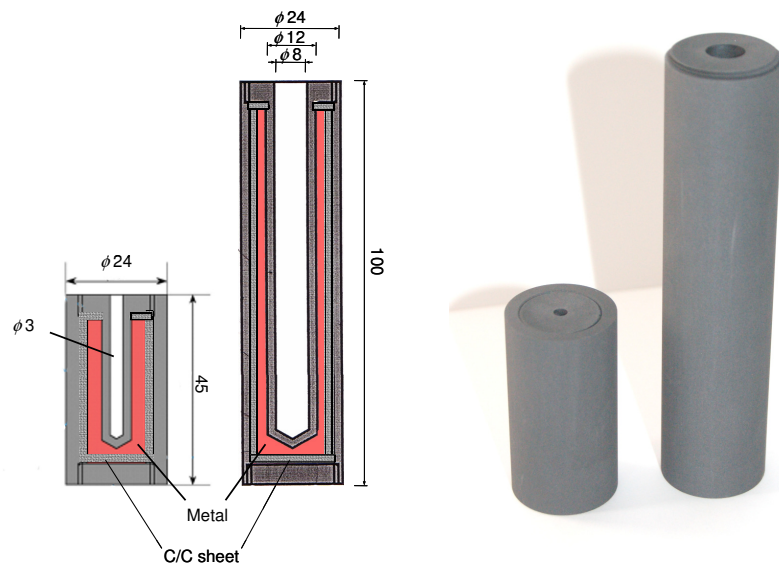


Figure 5.2: Cell design used for Cu, Pt-C and Re-C fixed point cells, dimensions in mm.

The cells were filled vertically, with the opening of the cavity facing down. The filling furnace (Nagano VR20-A10) used for these cells here at the NMIJ is similar to the Nagano M furnace detailed below, but arranged vertically. The fixed-point crucible was placed inside a cylindrical graphite chamber, which is exchanged for

each type of metal to protect metal deposition on furnace parts and thus to prevent cross-contamination. This chamber is directly surrounded by the carbon-fibre reinforced carbon composite heater element. For temperature control the furnace is equipped with a W/Re thermocouple and a radiation thermometer port at the top for monitoring the temperature. To prevent reaction of the alumina insulation material with the graphite furnace material and to conserve the thermocouple itself, the sensor can be retracted from the furnace centre so that at 2500 °C there is approximately a 1000 °C temperature difference between the thermocouple reading and the true furnace temperature.

The radiation thermometer focuses on a 2 mm hole in the lid of the cylindrical chamber. The signal from this is used to determine when the metal powder has melted. This furnace can be operated in vacuum up to 2000 °C, in addition to an oil rotary pump, a turbo molecular pump is connected through 33 mm to 37 mm inner diameter tubes and pipes allows the filling to be done in vacuum and the degassing of all crucible graphite parts. As an example for filling an Re-C point, the furnace is operated in vacuum up to 2000 °C, then in helium and argon to 2500 °C. Helium is used in the centre of the furnace to prevent electrical discharge; argon is used in the surroundings to improve thermal insulation. A vacuum gauge is located in front of the turbo molecular pump. Although the reading at this position cannot be expected to be equivalent to the pressure inside, it gives an indication of the amount of degassing from inside the furnace, and therefore indicates when baking can be stopped. A thorough furnace baking is carried out whenever the filling metal material is changed. Fig.5.3 shows the decrease in pressure, while the furnace is steadily evacuated and heated. Only when the temperature exceeds 1900 °C, the pressure is continuously dropping, which is understood as a sign of effective degassing of the crucible/material in the furnace.

This furnace is used exclusively for filling fixed-points, and care is taken to avoid cross-contamination between different materials. Disposable items as plastic containers or weighing spoons are used where possible and all items are cleaned with ethanol, to avoid contact with any surface plastic wrap or cling-film is used.

The metal and graphite powders are weighed and mixed at the eutectic composition less 1 % (typically the eutectic composition is 2% carbon by weight). The material is weighed and added to the crucible in an argon-filled glove-bag, which is exclusively used for only one filling.

Each filling step is carried out after the furnace was pumped and refilled with Argon gas.

After each filling cycle the fixed-point is visually inspected. Any appearance of graphite on the surface is understood to be a sign of a hyper-eutectic alloy. The composition of the next fill can then be altered by adding additional pure metal powder.

Once the crucible is considered sufficiently full the ingot is covered with one or two additional C/C discs and the graphite end cap is screwed into place and the

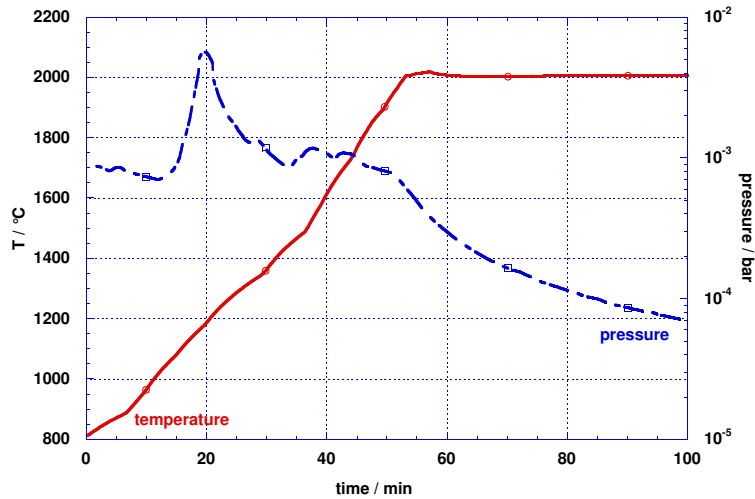


Figure 5.3: The filling furnace can be evacuated for degassing of the crucibles. Only at a temperature higher 1900 °C the pressure is steadily decreasing showing the effective degassing of the crucible.

fixed-point is completed.

The following list summarizes the described filling technique:

- To avoid cross-contamination between different metals only disposable plastic container were used for weighing and filling, a new set of containers is used with every new material
- Filling and weighing is done under Ar atmosphere in an inflatable plastic glove-bag, one glove-bag is used exclusively for one material
- Degassing of all graphite parts (crucible and C/C sheets) under vacuum up to 2000 °C and under argon atmosphere in the furnace up to 2500 °C
- C/C sheets are inserted between ingot and crucible for an improved temperature uniformity and mechanical stability

The novel large aperture design appears to be easily affected by cell breakage and non-uniform ingot formation. The 2 mm thin outer graphite walls are fragile and the design constraints as 24 mm outer diameter with an 8 mm diameter cavity leaves only a small channel for the metal ingot between crucible wall and cavity. First attempts in filling cells of this design were therefore not successful. In order to guarantee a uniform ingot first a hypo-eutectic Re-C mixture was tested, because of its lower viscosity in the melt and therefore higher likeliness to fill the narrow gap between cavity and crucible wall uniformly. During filling with metal powder it became already apparent, that the metal carbon easily separates due to the large density difference between the two materials. As a result the long thin channel of the crucible when filled with the premixed powder will have a carbon concentration gradient from bottom to top with higher carbon concentration on the top and more graphite has to be taken from the crucible walls to form the eutectic alloy at the

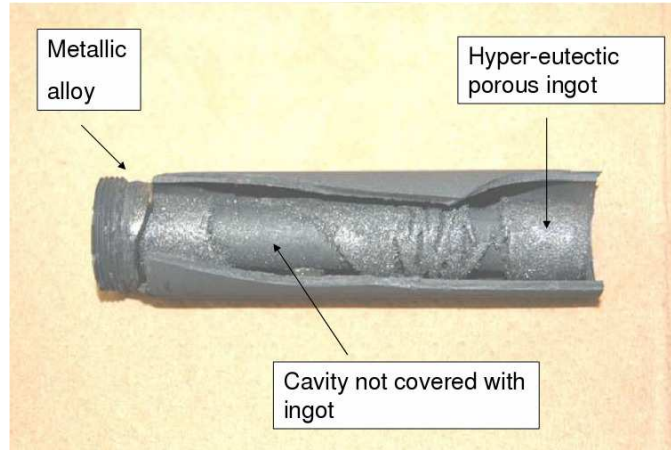


Figure 5.4: First attempt of filling a large aperture cell of Re-C.

bottom, which weakens the already thin graphite walls additionally and led to cell breakage (Figure 5.4).

Such problems of cell breakage can be minimized if a hyper-eutectic metal-carbon mixture is used. Here, the mix is a few percent richer in carbon than the eutectic composition. This alloy will not damage the graphite walls, it however, due to its high viscosity settles in a porous sintered structure, that shrinks in its original shape formed when filling with the powdery mix even when it is melting. After sintering and melting the volume taken up by the ingot is reduced by only a few ten percent. The minimization of surface energy, and thus the forming of a small volume metal with high density is hindered by the high viscosity of the graphite enriched material. The change of shape can best be described as shrinking of the filled volume. In the crucible for the sintered metal ingot an ideal, free shrinking in all directions can be impeded by adhesion to the graphite walls, the cylindrical shape and non-uniformities of the material. As a result the thin cylindrical ingot can tear, leaving parts of the cavity non-covered by the fixed-point material.

Therefore, for the large aperture cells of Pt-C and Re-C a special filling scheme was developed. The cells were filled with a hyper-eutectic metal-carbon mixture to avoid an additional reaction of the metal with the graphite walls of the crucible. To ensure an uniform ingot formation, the filling was performed in additional steps. In each step the cells were additionally filled with metal-carbon powder up to 20 mm in height and then sintered at a temperature 50 K - 100 K below the materials melting temperature. This temperature was only exceeded for the completely filled cell to melt the metal-carbon eutectic.

Material	Cell design	C/C layers	Mass	Mixture
Cu	small aperture cell	2 C/C layers	25.8 g Cu	
5N Alfa Aesar	large aperture cell	2 C/C layers	113.2 g Cu	
Pt-C	small aperture cell	2 C/C layers	65.1 g Pt	hypo 0%
5N Tanaka Kanzo	large aperture cell	2 C/C layers	70.6 g Pt	2% hyper
Re-C	small aperture cell	2 C/C layers	57.2 g Re	hypo 1.1%
5N ZKMW China	large aperture cell	2 C/C layers	76.8 g Re	5% hyper

Table 5.1: Overview of the manufactured fixed-point cells

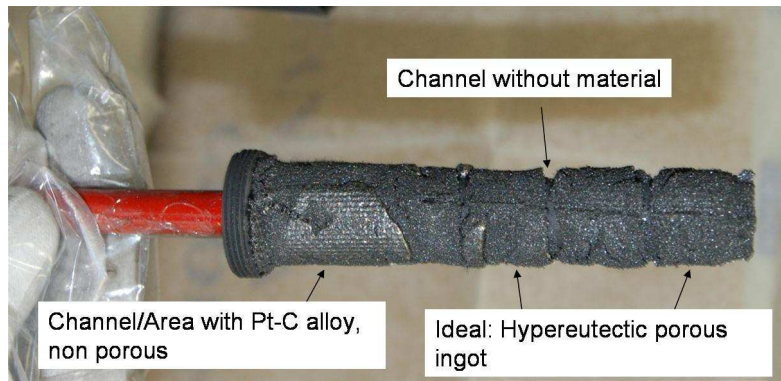


Figure 5.5: The ingot of the large aperture Pt-C cell after sintering and melting.

6 Detectors of thermal radiation

Planck's law of thermal radiation connects the temperature of a blackbody to radiometry. In radiometry electromagnetic radiation is typically described by the following quantities.

Radiant flux (or *optical power* or *radiant power*) is the energy Q (in Joule) radiated by a source per unit of time, expressed as

$$\Phi = \frac{dQ}{dt}. \quad (6.1)$$

The unit of radiant flux is the Watt ($W = J/s$).

The **solid angle** Ω of a cone is the ratio of the area A cut out from a spherical surface to the square of the radius r of the sphere

$$\Omega = \frac{A}{r^2}. \quad (6.2)$$

The unit of solid angle is the dimensionless unit steradian sr.

Radiance L is the radiant flux per unit solid angle emitted from a surface element in a given direction per unit area of the surface element perpendicular to the direction.

$$L = \frac{d^2\Phi}{d\Omega dA \cos\theta} \quad (6.3)$$

The unit of radiance is $Wsr^{-1}m^{-2}$.

Irradiance E is the density of incident radiant flux at a point or area on a surface, defined as radiant flux per unit area (unit is W/m^2)

$$E = \frac{d\Phi}{dA} \quad (6.4)$$

When detectors are used in radiometry an additional important quantity is the **spectral responsivity** of the detector. In case of photo-diodes it is the output current for a given optical flux received by the detector.

The typical measurement geometry for the detection of thermal radiation by a radiation thermometer in terms of spectral radiance, and by a filter radiometer in terms of spectral irradiance is shown in Fig. 6.1.

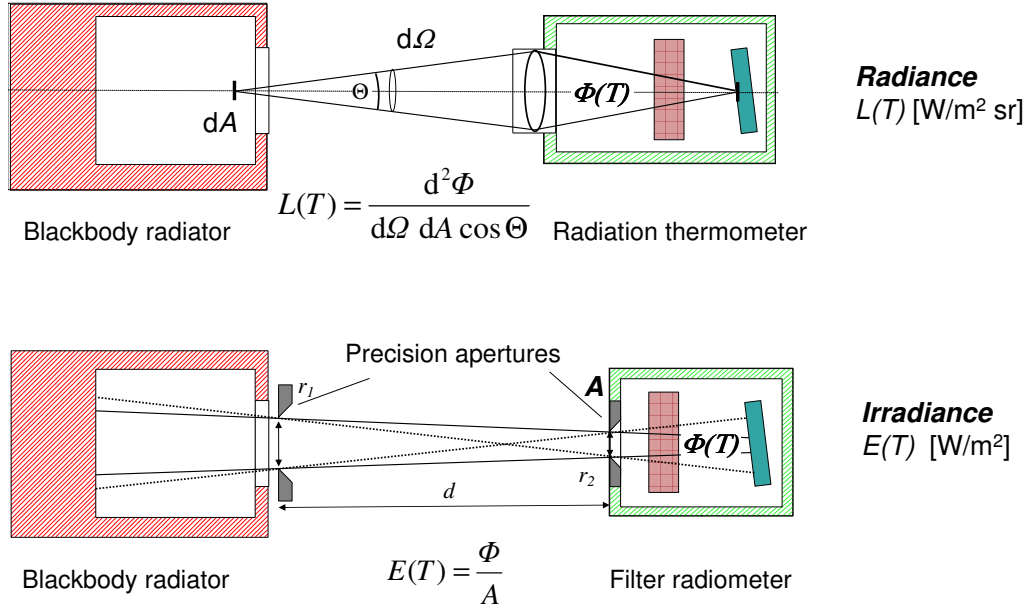


Figure 6.1: Measurement geometry for the measurement of thermal radiation with a radiation thermometer and a filter radiometer

The relation between Planck's law and the irradiance mode measurement with the filter radiometer is analysed in the following.

The blackbody radiator is an irradiance source with temperature T and spectral radiance

$$L(\lambda, T) = \varepsilon(\lambda) \cdot L_{\lambda, BB}(\lambda, T) = \varepsilon(\lambda) \cdot \frac{2hc^2}{n^2\lambda^5} \cdot \frac{1}{\exp\left(\frac{hc}{n\lambda kT} - 1\right)} \quad (6.5)$$

with $\varepsilon(\lambda)$ the emissivity of the blackbody radiator. The optical geometry is defined by the area of furnace aperture A_1 with radius r_1 , the area of detector aperture A_2 with radius r_2 and the distance d between the two apertures. The radiant flux $d\Phi_{1 \rightarrow 2, \lambda}(\lambda, T)$ from one area element dA_1 of the aperture A_1 to an area element dA_2 of the aperture A_2 is

$$d\Phi_{1 \rightarrow 2, \lambda}(\lambda, T) = L_{\lambda}(\lambda, T) \cdot \frac{dA_1 \cos \vartheta_1 \cdot dA_2 \cos \vartheta_2}{d^2} \quad (6.6)$$

where d' is the distance between the two area elements and ϑ_1, ϑ_2 are the angles between the normal vectors of the area elements. The total radiation transport between source and detector can then be expressed as

$$\Phi_{1 \rightarrow 2, \lambda}(\lambda, T) = L_{\lambda}(\lambda, T) \cdot \int_{A_1} \int_{A_2} \frac{dA_1 \cos \vartheta_1 \cdot dA_2 \cos \vartheta_2}{d^2} \quad (6.7)$$

For the experimental set-up used here an analytical solution is given by [Mod03]

$$\Phi_{1 \rightarrow 2, \lambda}(\lambda, T) = L_{\lambda}(\lambda, T) \cdot \frac{2\pi r_1^2 \cdot \pi r_2^2}{r_1^2 + r_2^2 + d^2 + \sqrt{(r_1^2 + r_2^2 + d^2)^2 - 4r_1^2 r_2^2}} \quad (6.8)$$

Then follows for the spectral irradiance at the detector aperture

$$\begin{aligned} E_{\lambda}(\lambda, T) &= \frac{\Phi_{1 \rightarrow 2, \lambda}(\lambda, T)}{\pi r_2^2} \\ &= \varepsilon \cdot L_{\lambda, BB}(\lambda, T) \cdot \frac{2\pi r_1^2}{\underbrace{r_1^2 + r_2^2 + d^2 + \sqrt{(r_1^2 + r_2^2 + d^2)^2 - 4r_1^2 r_2^2}}_{\text{geometrical factor G}}} \end{aligned} \quad (6.9)$$

The photo-current of the detector, which is here a filter radiometer that is calibrated in terms of spectral irradiance responsivity $s_E^{FR}(\lambda)$ is then for an experimental set-up as shown in Figure 6.1 given by

$$I_{photo} = \int_{\lambda} s_E^{FR}(\lambda) \cdot E_{\lambda}(\lambda, T) d\lambda = \varepsilon \cdot G \cdot \int_{\lambda} s_E^{FR}(\lambda) \cdot L_{\lambda, BB}(\lambda, T) d\lambda \quad (6.10)$$

where G represents the geometrical factor defined in eq.6.9 . Measurement of the photo current therefore allows to determine the temperature of the blackbody radiator, if the following parameters are known: the spectral irradiance responsivity of the detector, the geometrical factor G , i.e. aperture radius r_1, r_2 and the distance d between the apertures, and the emissivity ε of the blackbody radiator.

6.1 Radiation Thermometer LP3

In metrological laboratories worldwide the radiation thermometer LP3 ¹ is used for radiation temperature measurements at the highest metrological level and as a transfer standard to establish traceability. With the fundamental principle developed by PTB [KK75], the instrument was developed and is commercially manufactured by KE Technologie GmbH, Stuttgart [Woe82, FNST01].

A detector, such as a silicon photo-diode, generates a photo-current proportional to the incident radiation. For a certain range of sufficient stability of the detectors sensitivity vs. incident radiation intensity as well as vs. time the detector allows the measurement of a radiation intensity ratio in terms of a ratio of photo currents I_1/I_2 . And together with an optical system this is then also valid for radiance ratios L_1/L_2 .

$$\frac{I_1}{I_2} = \frac{L_1}{L_2} \quad (6.11)$$

Thus, using Planck's equation for the radiance L the unknown temperature of a blackbody can be determined from a radiance comparison with a reference source. For highest precision measurements only a narrow wavelength interval of the total temperature radiation is selected by an interference filter and one can write for blackbodies at temperatures T_1 and T_2 [PT90]

$$\frac{I_1}{I_2} = \frac{L(T_1)}{L(T_2)} = \frac{\exp(\frac{c_2}{\lambda_{eff}T_2}) - 1}{\exp(\frac{c_2}{\lambda_{eff}T_1}) - 1} \quad (6.12)$$

The instrument here is characterised using the concept of the mean effective wavelength λ_{eff} , a single wavelength at which the spectral radiance ratio is equal to the measured radiance ratio for the temperatures T_1 and T_2 [Lie76, HM77, Eul60]. With this method the full integral in the Planck equation does not have to be solved, which would require an absolute characterisation of the used interference filter, the instruments transmission and the detectors spectral responsivity. Therefore, it follows

$$T_2 = \frac{c_2}{\lambda_{eff}} \Big/ \ln \left(\frac{I_1}{I_2} (\exp(\frac{c_2}{\lambda_{eff}T_1}) - 1) + 1 \right).$$

Photo-current I_1 and temperature T_1 can be determined at a blackbody source of known temperature, a reference point or fixed point black body. For any measured photo-current I_2 the temperature T_2 can then be calculated if λ_{eff} is known.

Using Wien's approximation eq.(6.12) λ_{eff} can be calculated directly from the relation

$$\lambda_{eff} = c_2 \left(\frac{1}{T} - \frac{1}{T_{ref}} \right) / \ln \frac{I_{ref}}{I} \quad (6.13)$$

in an iterative process that usually converges after a few steps.

¹LP=LinearPyrometer

This measurement principle allows to realise the International Temperature Scale of 1990 (ITS-90) at high temperatures when a gold, silver or copper fixed point blackbody is used as a reference. The LP3 features a silicon detector with advanced electronics to process the photo current signal. The most important design principles of the LP3 are presented in Fig.6.2 and are described in the following.

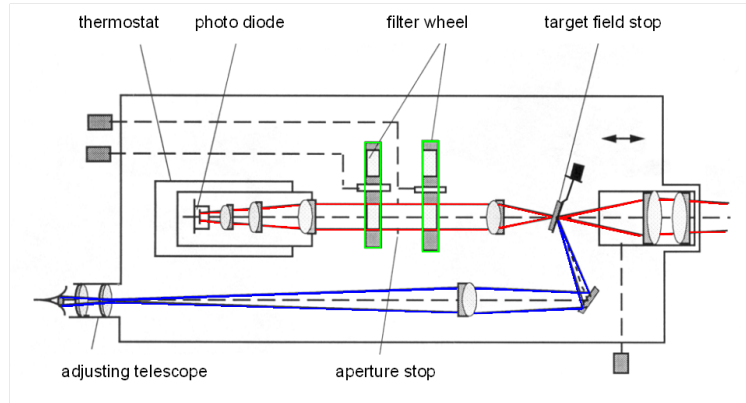


Figure 6.2: Schematic diagram of the optical design of the LP3.

Optical design: The front lens images the target on the measurement field stop, which consists of a mirror with a 0.2 mm diameter aperture. The reflected light from this mirror passes to an eyepiece, which enables focusing and position alignment. The radiation which passes the aperture in the measurement field stop is collimated onto interference filters, which are mounted in two filter wheels with six filter positions each. Neutral density filters or blocking glasses are preferably mounted in the first filter wheel, while interference filters are mounted in the second filter wheel. The incident radiation is finally detected by a Si photo diode positioned in a temperature stabilized housing in the optical path.

Spectral characteristics: Main design features of the interference filters are optimum blocking of the side bands and high long-term stability preventing an ageing, e.g. caused by humidity. Typically a narrow bandwidth of the interference filters of around 10 nm is selected for a low dependency of the effective wavelength on the measured temperature. Fig. 6.3 shows the relative spectral responsivity of the LP3 S/N 8005.

6.1.1 Stability at high temperatures

This section describes a solution for one of the largest problems of reproducible measurements at high temperatures: A thermal drift of the interference filters used in the radiation thermometer [HAH⁺03].

The LP3 with an interference filter at 650 nm can readily measure up to 2850 °C without using additional neutral density (ND) filters. However, applying the LP3

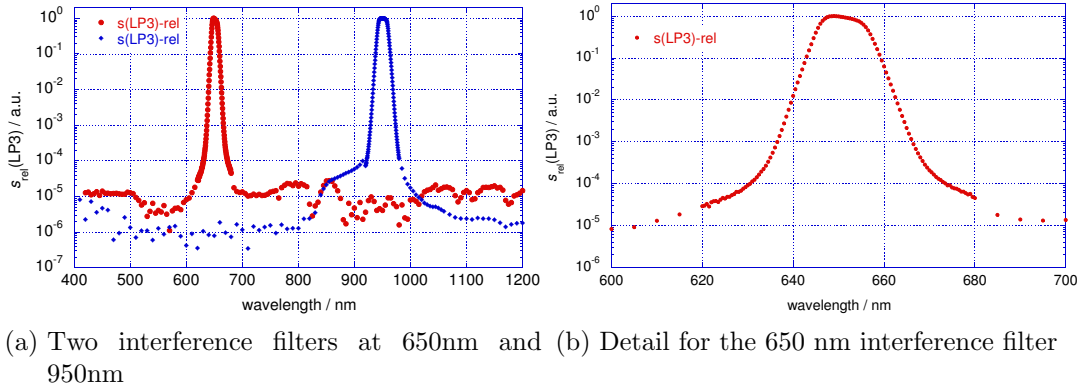


Figure 6.3: Relative spectral responsivity of the radiation thermometer LP3-8005 with the interference filters for 650 nm and 950 nm (a) and 650 nm at enlarged wavelength scale (b)

to measure the phase transition temperatures of Re-C at about 2475 °C revealed a significant thermal drift of several hundred mK of the signal, when measuring the Re-C fixed-point under equal conditions repeatedly. Figure 6.4a shows details of this effect. It was reported that this effect recovers partly in a relatively short time (less than one hour) [Har02]. However, for several days after such a high temperature measurement at 2500 °C with the LP3 the temperature measured for a copper fixed-point was still lower by up to 100 mK.

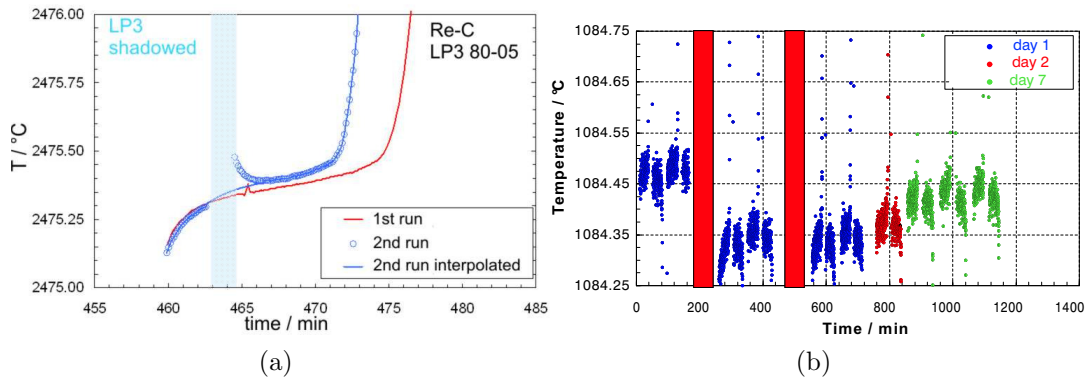


Figure 6.4: Two temperature measurements during the melting of a Re-C eutectic fixed-point cell. In the second run the radiation thermometer has been shadowed for about 2 minutes as indicated by the grey area (a), Cu fixed-point temperature values after the high temperature measurement reveals the drift (b)

To obtain further insight in the thermal drift problem the radiation thermometer was focused on a blackbody source with a stable radiation temperature of about 2500 °C. To investigate the drift of the detector signal, the radiation coming from

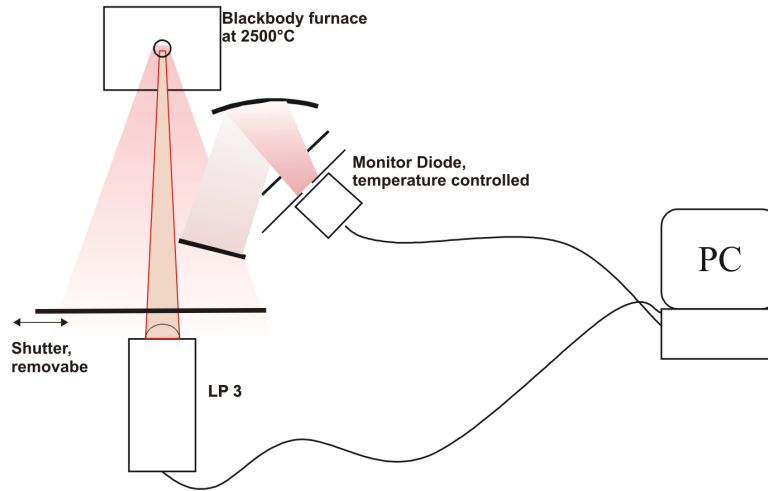


Figure 6.5: Schematics of the setup used to investigate the thermal drift of the interference filters of the LP3

the blackbody source was shadowed for different periods of time and the signal as a function of time after the LP3 received again radiation from the blackbody was recorded. A monitor diode allows a correction of the LP3 signal for any drifts of the furnace signal. Figure 6.5 gives schematics of the experimental set-up.

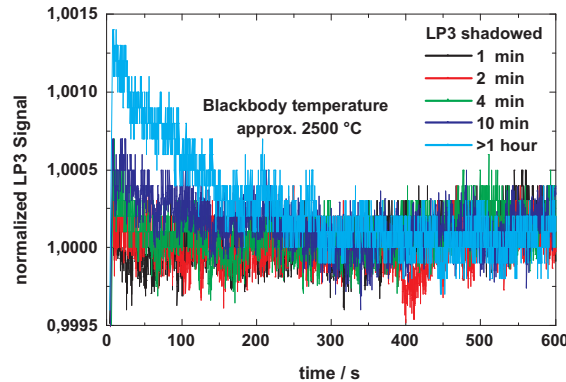


Figure 6.6: Temporal behaviour of the relative photo-current of the radiation thermometer LP3 equipped with the old interference filter set-up focussed on a stable blackbody at about 2500 °C

Figure 6.6 shows a summary of results obtained with the radiation thermometer equipped with the original interference filter with a central wavelength around 650 nm. It can be concluded from Fig.6.6 that the largest effect is observed when the cold interference filter is exposed to the radiation from the high temperature blackbody. The decay time of this effect is about 5 minutes. If the radiation thermometer

is shadowed for more than 4 minutes and after reaching thermal equilibrium, a distinct effect can be observed. Therefore, a minimum time of 4 minutes is necessary to allow for a significant cooling of the interference filter.

The result of this investigation is that there is indeed a thermal drift behaviour and that the time constant is about 4 to 5 minutes. As a consequence, precautions have to be taken if the radiation thermometer LP3 is to be used with this interference filter for a high temperature measurement: One has to ensure that during calibration and measurement the LP3 is used at thermal equilibrium, i.e. the LP3 is at least 5 minutes exposed to thermal radiation before the measurement can commence. Additionally, the results of these investigations lead to the assumption that the main reason for the short-term thermal drift should be a heating up of the interference filter, which causes a thermal expansion and, therefore, a change of the wavelength of the filter.

6.1.2 Solving the thermal drift problem

From the investigation presented in the last section it was concluded that the thermal drift problem is caused by a heating of the applied interference filter. The filters used so far consist of a multilayer structure, this is the main part of the interference filter, mounted directly on a colour glass substrate that blocks radiation in side bands off the centre wavelength of the interference filter.

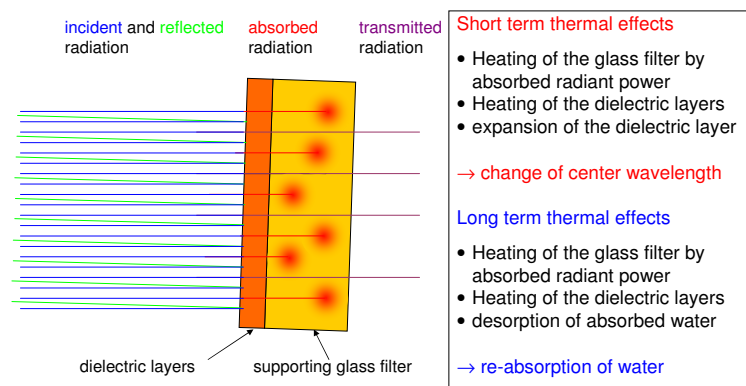


Figure 6.7: Absorption of light in the colour glass leads to an heating and consequently to a change in the centre wavelength

Figure 6.7 shows the working principle of the interference filter and colour glass. Generally, for a wavelength other than the centre wavelength light is reflected by the interference filter and the transmitted radiation outside the bandpass is absorbed by the colour glass. Therefore, the colour glass is significantly heated when high temperature radiation has to be filtered. This absorption is the underlying process that causes the thermal instability as it heats up the multilayer structure, which is in intimate contact with the colour glass. By heating, the multilayer structure is

changed, resulting in a change in effective wavelength of the interference filter and with a change in signal.

To prevent this effect a new interference filter design has been implemented in the LP3. In the new design a colour glass filter is separated from the multilayer structure which is now on a standard optical glass². A special colour glass filter was selected with a low temperature dependence for the transmittance at the central wavelength of the interference filter and is mounted in the second filter wheel. This design reduces the temperature increase in the interference filter significantly so that only a small drift in the temperature signal after exposure to thermal radiation is obtained. This new filter design for the LP3 was tested in a similar procedure as described before.

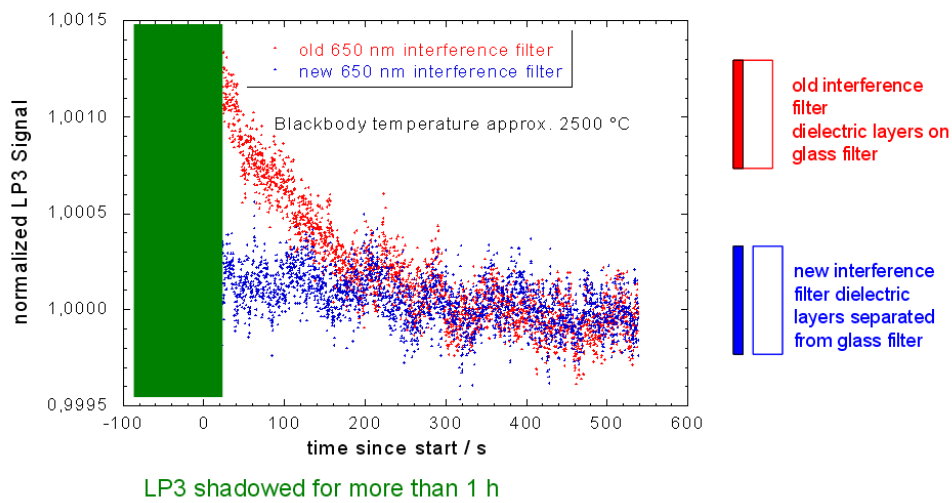


Figure 6.8: Temporal behaviour of the photo current for the radiation thermometer LP3 80-05 equipped with the old and new interference filters. The blocking time was more than one hour for both measurements.

Figure 6.8 demonstrates that the separation of the interference filter from the colour glass filter significantly reduces the thermal drift problem. For further support of this findings experiments similar to that shown in Fig.6.4a have been performed with the improved LP3 and no significant change in the plateau shape has been observed when temporarily blocking the radiation.

This result is additionally confirmed by an investigation on the longer term stability at the gold point of the instrument during the measurements described in Chapter 8.1. Here, the LP3 8005 with the new filter set-up was used during a 2 week comparison to measure Pt-C and Re-C fixed-point cells. On each day a gold fixed-point was measured before and after the measurements at Pt-C and Re-C to monitor the

²OG515

instruments stability. The measured radiance temperature of the gold fixed-point differed by less than 50 mK during these 2 weeks. No significant differences of this result were observed for measurements at 1738 °C, Pt-C, and 2475 °C, Re-C (Figure 8.1).

6.1.3 Size of source effect- SSE

For optical measurements of highest accuracy influences of the geometrical size of the object to be measured on the measurand have to be considered. This so called size-of-source-effect (SSE) is caused by scattering, optical aberration, diffraction and multiple scattering at lens or mirror surfaces of the radiation thermometer and inside its housing. This causes a dependence of the signal on the size of the radiating source, or in other words on the radiance distribution of the source.

Whenever two sources are compared, and unless they have exactly the same radiance distribution, the contribution of the SSE will be different for the two sources and a correction has to be made. Similarly, when two radiation thermometers are compared using one source, the influence of the SSE will be different for each radiation thermometer as the SSE depends on the design and performance of each instrument.

Generally, the calibration of a radiation thermometer involves the measurement of a reference source. Thus, any temperature measurement is effectively a radiance ratio measurement relative to this source and must involve a SSE correction and an accompanying contribution to the uncertainty.

The size-of-source-effect can be characterized by the fraction in spectral radiance or photo current signal I from a source with diameter d and temperature T with respect to the radiation coming from a source with infinite diameter d_∞ and same temperature T

$$SSE(d, T) = \frac{I(d, T)}{I(d_\infty, T)}.$$

In practice, for real sources of thermal radiation the outer dimensions are finite and only a diameter d_{max} can be realized.

The SSE is commonly determined by varying the source size of a uniform planar radiating source and the corresponding radiance signal. Two schemes of SSE measurement exist:

1. A direct method: The signal increase is measured when the radius of a disk radiating source is increased. It requires a highly stable and uniform source as small differences between two large signals are measured.
2. An indirect method: Here only the contribution from outside the target area is measured by blackening the source center to cover the target, the radiance signal is then measured by varying source diameter.

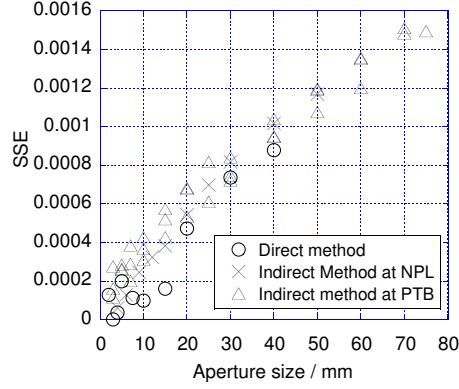


Figure 6.9: Size-of-Source-effect for the radiation thermometer LP3 80-05 measured with the direct and indirect method

In this work the SSE of an radiation thermometer LP3 has been determined using both methods.

For the direct method a double heat-pipe blackbody at 950°C was used. The radiating area was varied by apertures between 3 mm and 40 mm with the LP3 in an distance of 700 mm in front of the heat-pipe furnace.

A new set-up for the indirect method was developed in this work. In front of an integrating sphere a transparent plastic glass holds a black obscuration of 2 mm diameter and a cartridge holder allows to place apertures centric to the black spot. The apertures, made from 1 mm Al sheet metal and blackened to avoid multi-reflections, are between 3 mm and 50 mm in diameter and can be fast and easily exchanged in routine SSE measurements. The new set-up allows, in comparison to a previous device, a relatively quick measurement for routine determination of the SSE.

$$SSE(d, d_{ref}) = \frac{I_d(L_0) - I_{d_{ref}}(L_0)}{I_{d_{ref}}(L_0)} \quad (6.14)$$

In Figure 6.9 the results of an SSE measurement with the direct and the indirect method are presented. Additionally a SSE measurement of this instrument at another set-up, namely at the radiation thermometry group of the NPL is shown.

In order to correct for SSE, one needs to know the SSE function of the radiation thermometer and the radiance distribution L of the source. If a signal $I(d)$ is obtained with uniform disk source of diameter d in comparison to that of the same radiance with a diameter d_{ref} then the corrected Signal $I(d_{ref})$ is given by the following

$$I(d_{ref}) = (1 + SSE(d, d_{ref}))I(d)$$

More generally, if the radiance distribution $L(d)$ can be assumed to be radially symmetric and is given as a function of the relative source diameter, $\tilde{L}(d) = L(d)/L_0$,

then the detected signal will be related to the corrected signal $I(d_{ref})$ by the following

$$I = \left(1 - \int_0^{d_0} SSE(d)dd + \int_{d_0}^{\infty} \tilde{L}(d)SSE(d)dd \right) I(d_{ref})$$

Here, d_0 is a diameter within which the source can be assumed to be uniform (i.e. $\tilde{L}(d) = 1$ for $d < d_0$). This can be the target diameter or the cavity aperture in case of a blackbody source. The choice of d_{ref} is arbitrary as long as it is larger than the target diameter. It should be noted, that the SSE function needs to be characterized at least to where the integrand in the second integral becomes negligibly small so that the integral can be determined. Similarly, for the first integral to be calculable, d_{ref} needs to be smaller than the evaluated maximum diameter of the SSE function. Correcting towards a uniform source of infinite diameter (i.e. $d_{ref} = \infty$) is therefore usually practically not possible. The radiance ratio of two sources can be evaluated by simply correcting both measured radiance signals toward the same reference source diameter d_{ref} before taking the ratio.

Reduction of the SSE The magnitude of the SSE depends on the quality of the optical material used and on the design of radiometer. It has been shown that by reducing the number of glass air interfaces in the objective lens, by selecting of lenses with good surface finish and by adopting a Lyot stop the SSE can be greatly reduced [YAS05, SMY01].

6.2 Interference filter radiometers

In the previous chapter a standard radiation thermometer was described. The calibration methods in different national metrology institutes for the temperature measurement according to the ITS-90 will be presented in chapter 7. The calibration scheme typically yields expanded measurement uncertainties of around 1 K at 2500 K for a centre wavelength of around 650 nm. The main contribution to the measurement uncertainty for high temperatures originate in the extrapolation from the freezing temperature of gold point.

A direct thermodynamic temperature measurement of a blackbody radiator with lower measurement uncertainties is possible by applying radiometric methods and Plancks law of thermal radiation. The method and the filter radiometers used are described in the following section.

6.2.1 Set-up and principal features of a radiometer for spectral irradiance

Filter radiometers are widely used in radiometry as transfer standards for the measurement of spectral irradiance [FTM96, Fox95]. The main components of a filter radiometer are a precision aperture, an interference filter and a photo diode all set-up in a temperature controlled copper housing as displayed in Figure 6.10.

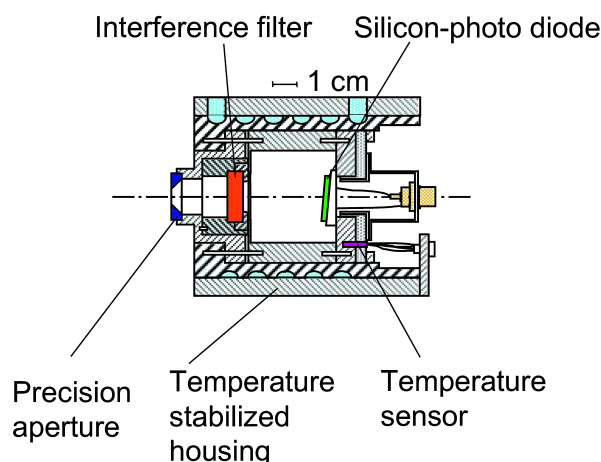


Figure 6.10: Schematics of a filter radiometer used for the thermodynamic temperature measurement. Main components are a diamond turned precision aperture, an interference filter and a Si- photodiode. A thermostat temperature controls the housing.

The diamond-turned opening aperture has a diameter of typically 5 mm or smaller and defines the effective area of the detector for a homogeneous radiation field.

Reflections at the apertures land are minimized by the small thickness of the land (ca. 15 μm), inter-reflections between aperture and interference filter are minimized by an opening angle of 29° relative to the optical axis on the tapered rear-side of the aperture.

The interference filter defines the spectral bandpass for the measurement of a broadband source such as blackbody radiation. In this work filter radiometers with interference filters with center wavelength of around 476 nm, 676 nm, 800 nm and 900 nm have been used, each with a spectral bandwidth of around 20 nm. High graded interference filters were selected as the temporal stability for a transfer standard is of concern. For the interference filters of 676 nm and 800 nm the $\lambda/4$ layers of the interference filters are made from cryolite and zinc sulfide [Sto95]. For all filters the out-of-band blocking is high with 10^{-7} to 10^{-9} relative to the bandpass [TFH⁺05]. The transmission of incident light shows an angular dependence and therefore the interference filter should be calibrated with the same beam geometry of the latter use.

A windowless Hamamatsu S1337 Silicon photo diode with a sensitive area of 10 mm x 10 mm is used as detector. The photo diode is tilted by about 5° with respect to the interference filter in order to avoid inter-reflections with the rear-side of the interference filter.

A thermostat controls the temperature of the housing to be $(25 \pm 0.05)^\circ\text{C}$, as the transmission of the interference filters shows a temperature dependence and shifts to longer wavelengths by about 30 pm/K [TFH⁺05].

The filter radiometers are stored in a dry chamber and clean room conditions are available in the laboratory for most measurements, which results to a good long term stability of these filter radiometers [TFH⁺05].

6.2.2 Radiometric calibration scheme

The various steps for the calibration of a filter radiometer at PTB are described in detail in [FFS96], [Tau03], [TFHH03] and [Sto95] and are summarized in the following section. Figure 6.11 illustrates the procedure. Basically, the calibration of a filter radiometer is a two-step process. First, a broadband transfer detector, e.g. a Si trap detector, is calibrated against a cryogenic radiometer at several discrete laser emission lines. Then the transfer detector is used to continuously calibrate the filter radiometer at a spectral comparator facility.

Traceability to the SI unit Ampere is performed using the electrical substitution principle. In electrical substitution radiometry incident optical energy heats a copper cavity and the resulting temperature change is monitored. The optical radiation is then shuttered off and the same temperature rise is created by electrical heating. The optical power must then be the same as the electrical power for the temperature rise. At cryogenic temperatures the sensitivity increases largely because of

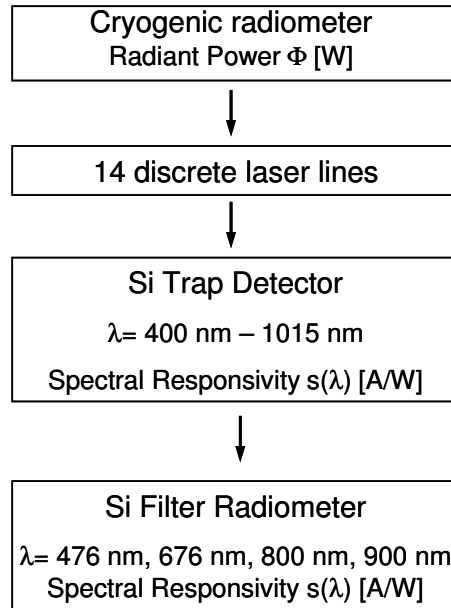


Figure 6.11: Radiometric calibration chain of the filter radiometer

the decrease in specific heat of copper, which allows larger cavity to be build which are better absorbers for optical radiation, additionally, superconductivity removes a self-heating effect of the leads, both effects help to improve the equivalence of optical power and substituted electrical power. The radiation thermometry cryogenic radiometer RTCR [Fu93, RJK⁺00] used at PTB employs laser radiation from a Kr⁺ and an Ar⁺ laser with optional intra-cavity frequency doubling and a tunable Ti:sapphire ring laser. With these lasers 12 lines in the UV (238 to 400 nm), 14 lines in the visible (400 nm to 799 nm) and continuously tunable radiation in the NIR (800 nm to 1015 nm) can be used for calibration. The uncertainty of the optical power measurement with the RTCR is 0.02 % to 0.08 % in the UV and 0.007 % to 0.01 % in the visible and NIR range.

For a single photo-diode the spectral responsivity $s(\lambda)$ can be expressed over a wide wavelength range as [Zal83]

$$s(\lambda) = \frac{Q_{int}(1 - R)}{hc}. \quad (6.15)$$

Where Q_{int} is the internal quantum efficiency and R the reflectivity. By specially arranging silicon-photo diodes the reflectance can be minimized and the resulting detectors responsivity is only wavelength dependent.

A trap detector [Pal93], [FTM96] is made up from several photo-diodes, which are arranged in a way that the radiation reflected from one photo-diode hits the next photo-diode. This results in a detector that behaves similar to a cavity detector with high absorption, and if only photo-diodes with high internal quantum efficiency are used the trap detector can have an external quantum efficiency approaching one.

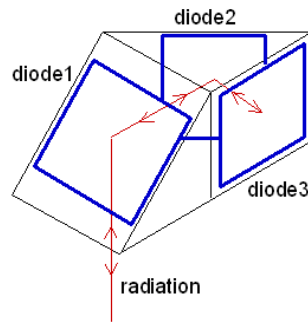


Figure 6.12: Schematic view of a reflection Trap detector; also shown is the path of the light inside the Trap.

An example for a trap detector with 3 photo-diodes is presented in Figure 6.12, after 5 reflections the radiation is reflected onto itself. Trap detectors are used for the calibration of filter radiometers as they allow to be used both with laser sources and for calibration with monochromator based sources. For the transfer of the spectral responsivity scale from the trap detector to the filter radiometer the spectral comparator set-up (Figure 6.13) is used.

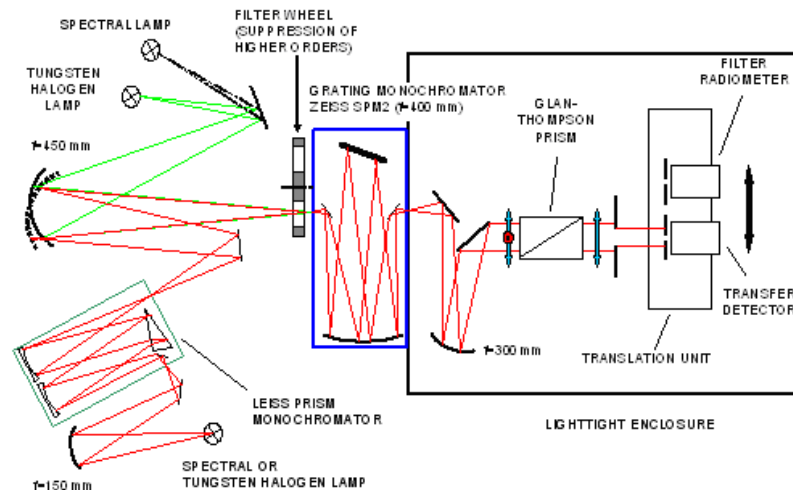


Figure 6.13: Improved spectral comparator facility for the calibration of narrow-band filter radiometers against broadband transfer detectors.

The calibration of a narrow-band filter radiometer against a broad-band detector such as a trap-detector requires the out-of-band transmission to be in the order of 10^{-6} . While for a single grating monochromator the stray light contribution is typically in the order of 10^{-5} , the required lower stray-light level could be achieved by the use of a prism monochromator as a predisperser for FR 476, FR 676, FR 800 and FR 900. Such a combination of prism and single grating monochromator

has advantages over the use of a double-grating monochromator as the transmitted flux is higher and no suppressing filters of higher order are required. For the calibration of the silicon diode based narrow-band filter radiometers up to 1200 nm gratings of 1302 lines / mm and 1200 lines/mm were used, resulting in a spectral dispersion of about 2 nm /mm. The wavelength setting for both monochromators has been calibrated at about 50 spectral emission lines of different spectral lamps. A Glan-Thompson polarization prism is inserted into the beam behind the grating monochromator in order to consider the influence of polarization in the spectral responsivity of the detectors. For three existing filter radiometers this calibration and stray light suppression scheme has been successfully applied, for the filter radiometer at 476 nm developed in this work the stray light suppression had to be improved as the prism monochromator uses a glass prism which limits the spectral dispersion of the monochromator to wavelengths above 400 nm. As a result stray light in the UV cannot be effectively suppressed and falsifies the result in the filter radiometers spectral responsivity in the UV below 400 nm shown in Figure 6.14. Here, compared to the halogen lamp a deuterium lamp spectral has a lower emission in the UV range and consequently the Si detector detects a lower signal level below 400 nm.

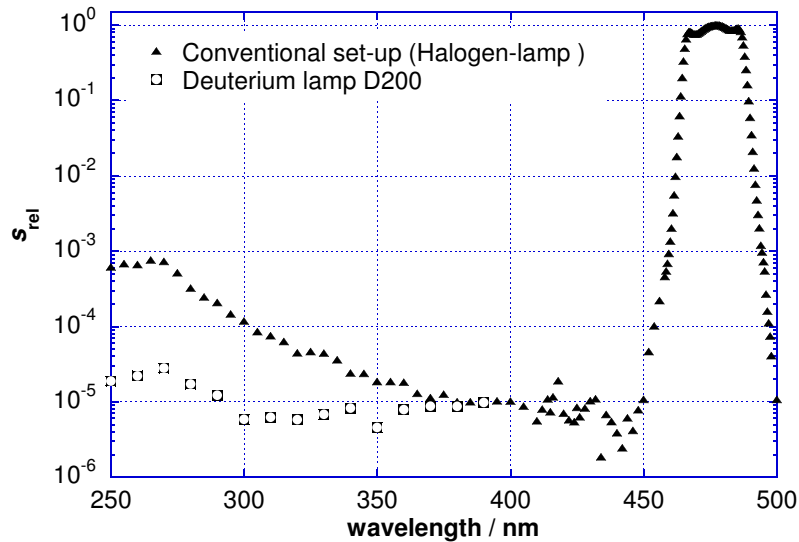


Figure 6.14: Initial investigations of the FR476 filter radiometer revealed stray light effects below 400 nm.

Only by selecting incident radiation exclusively in the UV the large influence of stray light could be further detected. A Xe arc lamp, with maximum emission already in the UV, together with long pass glass filters UG11 to block radiation above 400 nm was then used to show the blocking of the interference filter below 400 nm. The result is presented in Figure 6.15 . The resulting spectral responsivity is represented for non-polarized radiation and the data is the average of two measurements in two perpendicular directions of polarization.

The rise in spectral responsivity for wavelengths below 300 nm is most probably

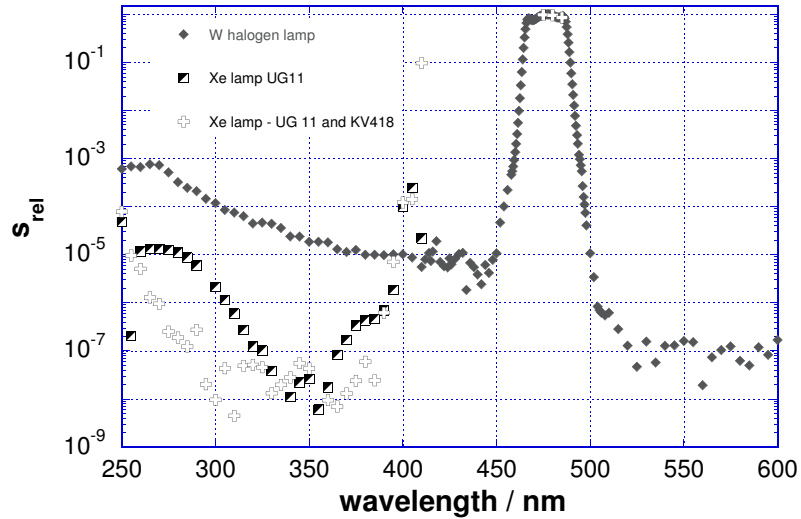


Figure 6.15: Relative spectral responsivity measurements for the calibration of the FR 476 filter radiometer. The influence of stray light was largely suppressed by the use of an Xe lamp in connection with suitable long-pass filters UG11 and KV418.

	FR 476	FR 676	FR 800	FR 900
Expanded standard uncertainty, $k=2$	7.8×10^{-4}	5.1×10^{-4}	5.8×10^{-4}	7.6×10^{-4}

Table 6.1: Uncertainties in spectral responsivity for the filter radiometers FR 476 [PTB05] , FR 676 [PTB03a], FR 800 [PTB03b]and FR 900 [PTB03c].

caused by fluorescence of the interference filter.

For all four filter radiometers used in this work the spectral responsivities are plotted in Figure 6.16 , Table 6.1 shows the expanded uncertainty of the spectral responsivity calibration. The relative measurement uncertainty is given for the maximum of the spectral responsivity, which represents an upper bound for the integrated total responsivity of the filter radiometer.

6.2.3 Diffraction at apertures

Precision apertures limit the optical beam diameter and define the optical beam geometry. Diffraction effects at these apertures lead to a deviation ϵ between the measured radiation flux Φ and the flux calculated by means of geometrical optics Φ_0 :

$$\Phi = (1 + \epsilon)\Phi_0 \quad (6.16)$$

Generally the deviation ϵ is small for a large ratio of aperture diameter to wavelength

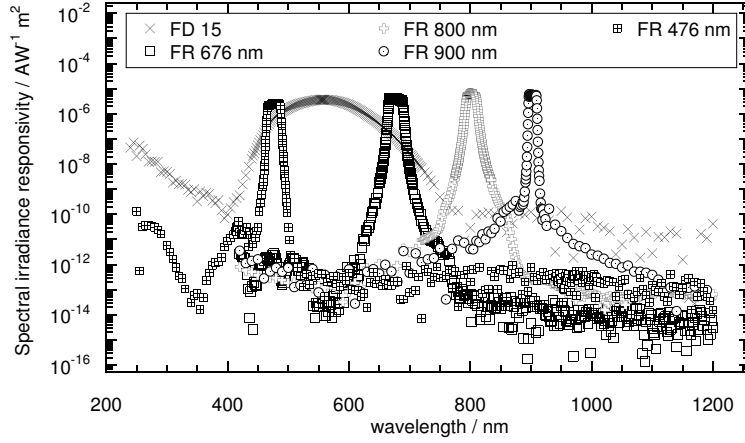


Figure 6.16: Spectral responsivities of the used filter radiometers

[Ble70], but can have positive or negative sign. For typical experimental set-ups in radiometry, where the radiation overfills the aperture, ϵ becomes positive and is generally $\ll 1$.

For irradiance measurements of an blackbody radiator like the HTBB diffraction occurs for both of the two apertures that define the optical geometry. As both effects are small, they can be treated independently and the two corrections add to

$$\epsilon(\text{aperture}_1 + \text{aperture}_2) \approx \epsilon(\text{aperture}_1) + \epsilon(\text{aperture}_2) \quad (6.17)$$

Hence, the following two cases will be treated separately:

1. Diffraction at the filter radiometers aperture: furnace aperture acts as a source and the photo diode as an underfilled detector
2. Diffraction at the furnace aperture: opening of the black body radiator HTBB acts as a source, the filter radiometer aperture as an over filled detector.

Invoking the reciprocity theorem of Kirchhoff, the deviation due to diffraction does not change if source and detector are exchanged. Therefore, the two cases can be treated as equivalent regarding in case 1) for the diffraction at furnace aperture the filter radiometer aperture as a source and the furnace opening as an underfilled detector.

[SDB72] gives both exact solutions and approximations for this diffraction problem. A simple approximation is given below:

$$\epsilon(u, w, w') \approx -\frac{1}{2\pi w} \ln \frac{(w' + w)^2 - u^2}{(w' - w)^2 - u^2} \quad (6.18)$$

with

$$u = \frac{2\pi}{\lambda} r^2 \left(\frac{1}{s} + \frac{1}{s'} \right) w = \frac{2\pi}{\lambda} r \frac{a}{s} w' = \frac{2\pi}{\lambda} r \frac{a'}{s'} \quad (6.19)$$

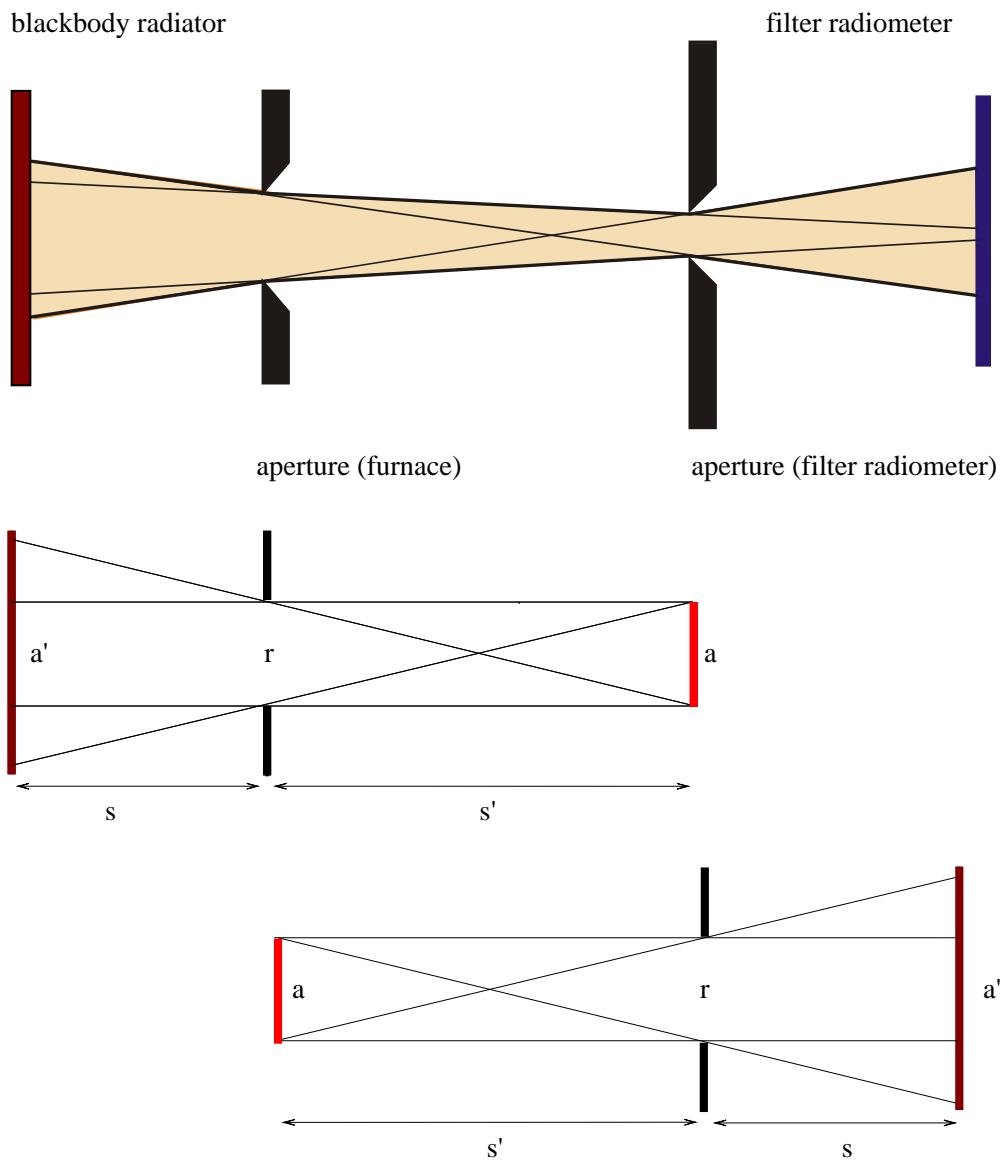


Figure 6.17: Calculation of the diffraction correction: The diffraction effects can be separated into a) diffraction occurring at the furnace aperture and b) diffraction at the filter radiometer aperture. a = source radius, a' = detector radius, r = aperture radius.

MC / MC-C	T / K	$u / \text{K}, k=1,$ FR 676, 3 mm aperture	$u / \text{K}, k=1,$ FR 676, 20mm aperture	$u / \text{K}, k=1$ LP3
Co-C	1597	0.12	0.04	0.38
Pd-C	1765	0.15	0.04	0.42
Pt-C	2012	0.2	0.06	0.49
Ru-C	2227	0.24	0.07	0.55
Re-C	2745	0.37	0.1	0.75
TiC-C	3031	0.45	0.13	0.86
ZrC-C	3153	0.48	0.14	0.98

Table 6.2: Standard uncertainty ($k=1$) of a thermodynamic temperature measurement for an ideal blackbody radiator, using filter radiometer FR 676 and two different precision apertures and the radiation thermometer LP3

This approximation is valid to $3 \cdot 10^{-5}$ for $(w + w')^2 - u^2 > 6000$. Here, for the diffraction at the filter radiometer aperture $(w + w')^2 - u^2$ amounts to 10^6 and for the furnace aperture to 10^7 . The approximation (6.18) can therefore be used.

For a blackbody source with broad spectral characteristics the diffraction correction has to be calculated for all wavelengths measured. The used radiometers only have a small bandpass of 10 nm - 20 nm. The diffraction correction ϵ is inversely proportional to the wavelength and varies little across the bandpass, for simplification only the centre wavelength of the interference filters is used in the calculation of the correction. While a furnace aperture diameter of 20 mm is typically used for the standard measurement of the HTBBs temperature using a FR676 filter radiometer, a large eutectic fixed-point cells requires a furnace aperture of 3 mm in diameter, which results in a considerably diffraction at the smaller furnace aperture.

Yet, a smaller furnace aperture contributes considerably to the overall measurement uncertainty, because of the increasing relative uncertainty contribution in the knowledge of the aperture area. The precision of the measurement of the aperture diameter is typically limited at around ± 500 nm. Table 6.2 illustrates the consequence on the measurement uncertainty for the two discussed furnace aperture diameters for the filter radiometer FR 676, and a distance of 1000 mm between furnace and detector aperture. Here, an ideal blackbody is assumed with an emissivity of 1. The lowest measurement uncertainty can only be achieved with a furnace aperture that is too large to measure a fixed-point cell directly.

7 Scale comparison of three different ITS-90 realisations

The level of agreement between scales at different national metrological laboratories will be an important consideration when deciding if alterations to the ITS would be beneficial to users. For this reason the high-temperature scales of the NMIJ and the NPL were compared with the scale of the PTB in 2001 and 2003. According to ITS-90 a temperature T_{90} above the freezing point of silver is defined by comparison of spectral radiance with a blackbody radiator operated at the freezing temperature of silver, gold or copper as described in Chapter 1. However, the ITS-90 does not recommend any particular methods or wavelengths for this comparison and consequently many approaches may be followed in order to realize a high-temperature scale on a thermometer. The first part of the chapter describes the different methods of scale realisation on radiation thermometers at the three participating institutes. In the second part the different comparisons and the results obtained are described.

7.1 Three different radiation thermometers and calibration schemes

The radiation thermometers used for the comparison are listed in Table 7.1. Common to all is an effective wavelength around 650 nm and the use of a silicon photodiode detector. Each of them is operated at different measurement distances and different focal length.

PTB-LP3

For these comparisons the PTB high-temperature scale was realised on a radiation thermometer of type LP3, which is based on a combination of high quality interference filters and a selected silicon photodiode with a resulting effective wavelength of $\lambda_{eff} = 650$ nm (Table 7.1). A sophisticated opto-mechanical configuration reduces polarisation dependence, stray-light, and size of source effect yielding an excellent reproducibility. The radiation thermometer LP3 was characterised by determining the linear relationship between the output signal of the detector and the spectral radiance of the measured source. For calibration the high temperature blackbody radiator BB3200pg (HTBB) was applied as a transfer standard source of thermal

Item	NMIJ Topcon	NPL LP2	PTB LP3
Type	OEP -PM -650NB	IKE LP2	IKE LP3
Serial number	90870181	LP2 -80 -30	80 -05
Nominal centre wavelength	650 nm	650 nm	650 nm
Band width (FWHM)	15 nm for 1 st filter, 45 nm for 2 nd filter	20 nm	10 nm
Temperature range	1100 K to 3100 K	800 K to > 3300 K	1000 K to 3400 K
Measuring distance	200 mm – 2000 mm	900 mm	440 mm to 1000 mm
Measuring distance in comparison	f = 800 mm	f = 950 mm (2001) f = 800 mm (2003)	f = 690 mm
field of view diameter	1.4 mm at 800 mm distance	0.75 mm at 900 mm distance	0.8 mm at 690 mm distance
Size of source effect	<1 % (6 mm to 140 mm)	0.1 % (3 mm to 50 mm)	0.1 % (5 mm to 70 mm)
ITS -90 fixed-point used	Cu	Au	Au

Table 7.1: Specifications of the radiation thermometers participating in the comparisons

radiation. The radiation thermometer LP3 was focused onto the entrance aperture of the HTBB. Determination of the temperature of the HTBB with respect to the PTB primary standard gold fixed-point blackbody (using a tungsten strip lamp as transfer source for thermal radiation) yields its temperature traceable to the ITS-90. For calibration, temperatures were measured every 200 K in the range from 1200 K to 3000 K. The resulting photo-current I_{Ph} versus temperature T curve was fitted with the following equation

$$I_{Ph} = C \cdot \exp\left(-\frac{c_2}{A \cdot T + B}\right) \quad (7.1)$$

with $c_2 = 0.014388$ mK [PT90] being the second constant of Plancks law of radiation [JV73]. Using the obtained parameters A , B , and C the temperature T was calculated from the measured photo-current.

NMIJ-Topcon

The specifications of the Topcon radiation thermometer used at the NMIJ for the comparison are listed in Table 7.1. It used a combination of two interference filters, one to define the measuring wavelength and the other to further suppress the out-of-band transmittance of the first filter. The Topcon radiation thermometer was calibrated using a copper point blackbody in combination with a spectral responsivity measurement and a nonlinearity measurement. From the measured spectral

responsivity $R(\lambda)$, the output signal $V(T)$ was calculated using Planck's law and

$$V(T) = a \int L_{\lambda,s}(\lambda, T) R(\lambda) d\lambda \quad (7.2)$$

The coefficient a was determined by the calibration at the copper-point. Output signals at 2300 K and 3200 K, which were calculated with Eq. 7.2, together with the measured output at the copper point were then fitted by the following equation:

$$V(T) = \frac{C}{\exp\left(\frac{c_2}{AT+B}\right) - 1} \quad (7.3)$$

NPL-LP2

The NPL pyrometer is an IKE LP2 [Sch]; details can be found in Table 7.1. The temperature of a source is determined by using Planck's law in ratio form, with the NPL gold point as the reference source, and using the mean effective wavelength (MEW) [BBMP90]. The MEW is calculated from the effective wavelength, which is determined at a number of different temperatures from the spectral response of the instrument and the calculated Planck function at each of the temperatures. The MEW is expressed as a function of source radiance temperature, T , in the form

$$\lambda_{MEW} = a + \frac{b}{T} \quad (7.4)$$

where a and b are best fit parameters. Two or three iterations of the ITS-90 defining equation are performed with successively better approximations to T to obtain a temperature with negligible error. The LP2 is used to realise the ITS-90 above the silver point at NPL, and scale realisation with an uncertainty of about 1 K ($k = 2$) at 2800 K is readily achievable [Mac99].

7.2 Comparison of the high-temperature scales

Comparison NPL-PTB

The ITS-90 scale realisation on the NPL LP2 and the PTB LP3 were compared at the NPL over the range of 1300 K to 3000 K using the NPL furnace supplied by ThermoGauge Instruments Inc.. Details on this furnace can be found in Table 7.2.

The two thermometers were mounted on moveable stages; the NPL LP2 at a distance of 900 mm to the aperture of the cavity, the LP3 at a distance of 700 mm, corresponding to the distances during the calibration of the thermometers.

On two subsequent days temperatures between 1300 K and 3000 K were alternately measured with the two radiation thermometers. For each thermometer at least two

	NMIJ	NPL	PTB
Manufacturer	Thermo Gauge	Thermo Gauge	Vega Inc.
Type	Dual blackbody Type VII	Dual Blackbody, 24 KW	BB3200pg
Heater cavity element	Graphite	Graphite	Pyrolitic Graphite
Temperature range	1300 K to 3000 K	1200 K to 3300 K	1300 K to 3200 K
Cavity diame- ter	51 mm	25,4	37 mm
Cavity depth	227 mm	300 mm	200 mm
Aperture size	32 mm	25,4 mm	22 mm
Emissivity		0.999	0.999
Window	No, purging with Ar	No, purging with Ar	No, purging with Ar
Temperature range	1100 K to 3100 K	800 K to 3300 K	1000 K to 3400 K

Table 7.2: Furnace specifications

readings were taken at each temperature. Additional measurements at the NPL gold fixed-point were taken before and after each days measurement in order to detect instabilities of the radiation thermometers. Both instruments used interference filters with an effective wavelength around 650 nm, the NPL-LP2 used additionally a neutral density filter for temperature measurements above 2100 K. For the PTB - LP3 no neutral density filter was applied over the whole temperature range. The results together with the overall uncertainty of the comparison are plotted in Fig. 7.1, showing an agreement between the two laboratories within 0.2 K at 1300 K and within 0.7 K at 2000 K. Even at 3000 K the agreement is within 0.3 K. These results are well within the overall uncertainty of the comparison.

Table 7.3 summarizes the uncertainty contributions to the comparison. The overall uncertainty u_{total} was expressed as

$$u_{total} = \sqrt{u_{ptb}^2 + u_{npl}^2 + u_{nmij}^2} \quad (7.5)$$

with u_{PTB} and u_{NPL} , the standard uncertainties of the PTB and NPL radiation thermometers and u_{comp} the standard uncertainty of the comparison. The uncertainty of comparison u_{comp} expresses the influence of the homogeneity and stability of the furnace on the comparison. One contribution is the effect of a possible 1 mm misalignment, determined from scans across the furnace at various temperatures. Another contribution is the temporal stability of the furnace during and in between the measurement. The set-up during the comparison was very similar to the calibration geometry of the instruments resulting in a small SSE, which was included in the individual instruments uncertainty.

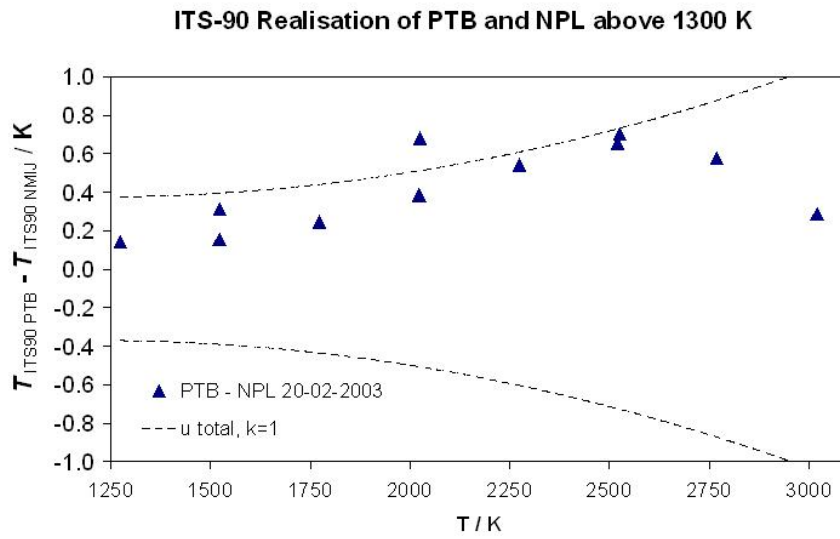


Figure 7.1: The difference in ITS-90 scale realisation above 1300 K at PTB and NPL

T / K	$u_{\text{NPL}} / \text{K} (k=1)$	$u_{\text{PTB}} / \text{K} (k=1)$	$u_{\text{comp}} / \text{K} (k=1)$	$u_{\text{total}} / \text{K} (k=1)$
1300	0.20	0.28	0.15	0.38
1530	0.13	0.32	0.19	0.39
1775	0.18	0.36	0.16	0.44
2025	0.25	0.42	0.14	0.51
2730	0.35	0.49	0.15	0.62
2520	0.41	0.57	0.18	0.72
2770	0.51	0.66	0.24	0.87
3020	0.64	0.77	0.33	1.05

Table 7.3: Uncertainty contribution to the comparison between PTB and NPL

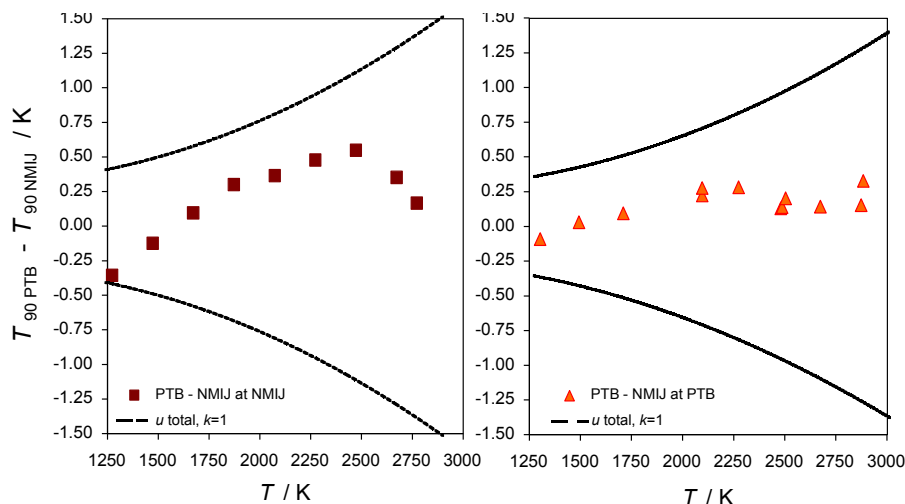


Figure 7.2: Two comparisons of ITS-90 realisation between PTB and NMIJ, left the result of a comparison at the NMIJ, on the right the result of the comparison at the PTB.

Comparison PTB - NMIJ

For the first comparison between the NMIJ and the PTB a calibrated LP3 from the PTB was sent to the NMIJ. At the NMIJ, the LP3 was additionally characterized regarding its size-of-source effect and its spectral responsivity. The blackbody used at the NMIJ was a Thermo Gauge furnace and the comparison was carried out in the temperature range from 1300 K up to 2800 K. Measuring distance to the aperture was 950 mm for the NMIJ Topcon and 690 mm for the PTB LP3. The result is shown in Figure 7.2. A good agreement within the combined uncertainty of the comparison was achieved: For temperatures between 1300 K and 2800 K the difference was within 0.4 K at 1300 K and better than 0.6 K for temperatures above 2000 K. Shortly after the comparison at the NMIJ the PTB-LP3 was improved to achieve a better stability for measurements in the high temperature range above 2000 K. For this the interference filters in the thermometer were completely exchanged as described in Chapter 6.

For a second comparison a NMIJ Topcon was hand carried to the PTB and a comparison of temperature measurement in the range from 1300 K up to 3000 K was performed on four subsequent days. The NMIJ Topcon has been calibrated directly before and after this comparison. The Topcon and the LP3 were placed on a moveable stage in front of the HTBB 3200pg furnace, the LP3 at a distance of 690 mm, the Topcon at a distance of 800 mm from the front aperture of the furnace. For temperatures between 1300 K and 3000 K a temperature, averaged over a 30 sec measurement period, was taken for each radiation thermometer. Both instruments measured alternately ten times at the respective temperatures, the results are shown in Figure 7.2. The good agreement of the first comparison was further improved.

T/K	u_{PTB}/K	u_{NMIJ}/K @NMIJ	u_{NMIJ}/K @PTB	u_{comp}/K @NMIJ	u_{comp}/K @PTB	u_{total}/K @NMIJ	u_{total}/K @PTB
1300	0.32	0.13	0.17	0.07	0.04	0.35	0.37
1500	0.35	0.17	0.22	0.07	0.06	0.4	0.43
1700	0.4	0.23	0.28	0.07	0.09	0.46	0.52
1900	0.45	0.3	0.36	0.07	0.11	0.54	0.61
2100	0.5	0.38	0.46	0.12	0.13	0.64	0.73
2300	0.57	0.48	0.56	0.18	0.15	0.76	0.86
2500	0.64	0.59	0.68	0.25	0.18	0.9	1
2700	0.72	0.71	0.82	0.3	0.2	1.05	1.16
2900	0.79	0.84	0.96	0.35	0.23	1.21	1.27

Table 7.4: Uncertainty components in NMIJ-PTB comparisons (all $k=1$).

In the second comparison an agreement within 0.4 K was achieved over the whole temperature range.

7.3 Discussion

Three bilateral comparisons of high-temperature scale realisations ranging from 1300 K to 3100 K between the PTB, the NPL and the NMIJ were presented. Each of the three NMIs was hosting one comparison, typical laboratory furnaces were used together with commercial high-accuracy radiation thermometers. Different approaches were used by the NMIs for a temperature scale realisation. The results obtained during the three comparisons all agree well within the combined uncertainties. This good agreement was achieved among three well equipped laboratories with highest level of experience in the field of high-temperature measurements. In order to disseminate the accessible low uncertainty to a wide range of users the new high temperature fixed-points using metal carbon eutectics were investigated in experiments described in the next chapters.

8 Evaluation of M-C eutectic fixed-points

This chapter presents results of different comparisons and measurements that have been performed during this work. These comparisons were aiming to proof the suitability of metal-carbon fixed-points for a future temperature scale, that is to proof their repeatability and reproducibility and to gain an understanding of the operational conditions necessary. For this a low uncertainty in the experimental realisation of the measurement is essential and guided the design and conduction of the experiments. As the detected differences between fixed-point cells are for some materials and manufacturers in the range of the day-to-day stability of the radiometers a side-by-side scheme is mandatory. In such a scheme two cells are compared using two furnaces rather than a sequential measurement scheme with one furnace and measurements of one cell per day only.

The sometimes high level of agreement between cells is also the reason for the need of comparisons. Successful filling of cells has been reported by several institutes such as NMIJ [YSSO99][Yam01][Sas02], VNIIOFI [SOK⁺03],BNM-LNE[SBF⁺05], KRISS [PKLP05], NIST [SYG⁺06] as also comparisons between the cells manufactured have been published. However, the first comparisons were often hindered by large uncertainty contributions as a considerable drift of the radiation thermometers or an unexpected large furnace effect. In this work a comparison scheme was established, that allowed a minimum measurement uncertainty.

In the next section a comparison between fixed-point cells manufactured at the NPL, the NMIJ and the BIPM at the NPL is described.

8.1 A relative comparison Pt-C, Re-C in two non-identical furnaces

This section describes a comparison of Pt-C and Re-C fixed-point cells that was held at the NPL in Teddington/UK. For this an PTB radiation thermometer LP3 was hand-carried to the NPL and the measurements were performed using additionally an NPL LP2 radiation thermometer. Two high temperature furnaces, one of type Thermogauge and one of type Nagano, were used. Eutectic metal-carbon cells of Pt-C and Re-C were investigated that had been manufactured by the NPL, the NMIJ and the BIPM with respect to differences in their melting plateau temperature.

	NPL	NMIJ	BIPM
Outer diameter /mm	24	24	24
Length /mm	40	45	45
Blackbody aperture /mm	3	3	3
Blackbody depth /mm	28	34	34
Rear cone angle	120	120	120
Isothermal emissivity	0.99965	0.9996	0.9996

Table 8.1: Differences in fixed-point cell design.

Parameter	NPL	NMIJ	BIPM
Re supplier	Alfa-Aesar	Leico Industries Inc	Alfa Aesar
Re batch-lot number	Re 22 167	R-1409	R-1409
Re nominal purity	0.99999	0.99997	0.99997
Pt supplier	Alfa-Aesar	Tanaka Kikinzoku Kogyo K.K.	Alfa Aesar
Pt batch number	CLO546	TKK 021201	CL0546
Pt nominal purity	0.99999	0.99999	0.99999
C powder supplier	Alfa-Aesar	Alfa-Aesar	Carbone Lorraine
C batch/lot number	2004-24	0157-22	133 622
C nominal purity	0.999999	0.999999	0.999999

Table 8.2: Fixed-point material data

8.1.1 Description of the eutectic fixed-point blackbody cavities

The cell design is of similar dimension as the cells built by PTB and described in chapter 5. The basic parameters of the six fixed-point cells investigated here are given as follows: all had an outer diameter of 24 mm, the NPL cells had a length of 40 mm, the cells of the BIPM and the NMIJ were 45 mm long. The blackbody aperture diameter was for all cells 3 mm. The blackbody had a depth of 28 mm (NPL) and of 34 mm (BIPM and NMIJ). The cavity was designed with a rear cone angle of 120°. The isothermal emissivity was calculated to be 0.99965 (NPL) and 0.9996 (BIPM and NMIJ), which based on values for the surface emissivity of graphite of 0.87 at the NPL (measured) and an estimated value of 0.8 for the cells of the NMIJ and the BIPM. Table 8.2 holds information about the materials that were used in the construction of the fixed-points. The nominal purities here are given as weight fraction.

The Re metal powder which was used by BIPM and NMIJ, although it was bought from different suppliers, has the same batch number, which indicates a common

source. Additionally, the Pt that has been used by NPL and BIPM was sourced from the same supplier and from the same batch. This provides useful information regarding possible contamination of the fixed-point material during the filling process.

The NPL crucibles were made of Poco Graphite, grade SFG, with nominal purity 99.9995%. After construction the crucible was baked in an argon atmosphere above the eutectic melting point to remove contaminants. The NPL crucibles were filled horizontally with a metal-carbon powder mixture near the eutectic composition. The filling took place in an argon atmosphere in a disposable glove box; a new glove box being used for each crucible to prevent cross contamination. The powder mixture was then melted in the crucible using the NPL Thermo Gauge furnace [LM04], subsequently cooled and the crucible refilled. This process was repeated until no more fixed-point material could be added .

The NMIJ crucibles were made of high purity graphite supplied by Toyo Tanso KK with a nominal purity of better than 99.9995%. The cells were purified and filled in a Nagano single zone furnace in vertical operation. Before filling, the empty crucible and furnace were purified by baking above the filling temperature for more than 30 minutes. This was done in vacuum below 2000 °C and in He above 2000 °C. To avoid cross contamination between different fixed-point materials the graphite parts of the furnace directly surrounding the cell were changed for each type of metal. The metal and graphite powders were mixed at approximately 1% hypoeutectic composition in an argon atmosphere. Approximately 10 to 15 fills were required to fill the crucible. The amount of carbon powder was gradually reduced towards the end of the filling to compensate for the carbon supplied from the graphite crucible by diffusion.

The BIPM crucibles were made of high purity graphite supplied by Carbone Lorraine, with nominal purity 99.99995%. The filling procedure was the same as that used by NMIJ described above.

8.1.2 Description of the used furnaces and the installation of the fixed-points

The **NPL Thermo Gauge** furnace is usually used with a fixed partition to form a blackbody radiator for the calibration of radiation thermometers. In order to realise eutectic fixed-points the dividing wall is removed and the crucibles are inserted centrally. Graphite foil of 0.1 mm thickness was used to wrap the crucibles in order to reduce the risk of contamination of the fixed-points and to centre the cell radially in the furnace tube. For better temperature uniformity a graphite felt insulation is used in front of and behind the crucible.

The other furnace, a **NMIJ Nagano M**, is identical to the furnace described in Chapter 4.1.2 and the same that was used in the comparison held at PTB, described in Chapter 8.2 and the investigation of small and large aperture cells, described in Chapter 8.3. This furnace was brought to NPL to investigate the influence of a

different thermal environment on the eutectic fixed-point transition. The furnace tube of this furnace is slightly larger than the ThermoGauge furnace, for this reason the cells were wrapped in 1.5 mm thick graphite felt and then installed into the furnace.

The radiation thermometers were both manufactured by KE Technologie. The NPL LP2 is described in detail in [Sch] and [MI99]. It does not feature the advanced temperature stability design developed and presented in this work. Therefore, the PTB LP3 was brought to NPL and was also used in this comparison.

8.1.3 Measurements

The eutectic fixed-point blackbody cavities were compared side by side in the high temperature graphite tube furnaces. The radiation thermometers were used to measure the transition temperature of each fixed-point. The stability of the radiation thermometer was checked each day by reference to the NPL primary standard gold point black body [CMA94].

A typical daily measurement cycle was as follows :

1. Measurement of the gold point freezing plateau with both radiation thermometers.
2. Initiation of the melt/freeze cycle for a metal-carbon eutectic in one furnace and three measurements with each radiation thermometer
3. Initiation of the melt/freeze cycle in the other furnace and three measurements with each radiation thermometer
4. Measurement of the gold point freezing plateau with both radiation thermometers.

After cooling down the furnaces the fixed-points were exchanged between the furnaces and re-measured the following day. The measurement schedule is given in Table 8.3.

Stability of the gold point

The gold point freezing temperature was measured each day to monitor any drift of the radiation thermometer. The PTB LP3 drifted by less than 50 mK at the gold point during the whole of the comparison and no correction was made, see Figure 8.1. In particular no influence of the high temperature during the days when the Re-C cells were measured and the furnaces were at a temperature of about 2500 °C was observed. For the LP2 the average of the gold point measurements at the beginning and end of the day was used as the reference photo current for each day's measurement and the uncertainty in the drift correction included in the uncertainty budget.

Day	Thermo Gauge	Nagano
5	Pt-C (NPL)	Pt-C (NMIJ)
6	Pt-C (NMIJ)	Pt-C (NPL)
7	Pt-C (NMIJ)	Pt-C (BIPM)
11	Re-C (NPL)	Re-C (BIPM)
12	Re-C (BIPM)	Re-C (NMIJ)
13	Re-C (BIPM)	Re-C (NPL)

Table 8.3: Furnace and crucible combinations tested during the measurements at the NPL.

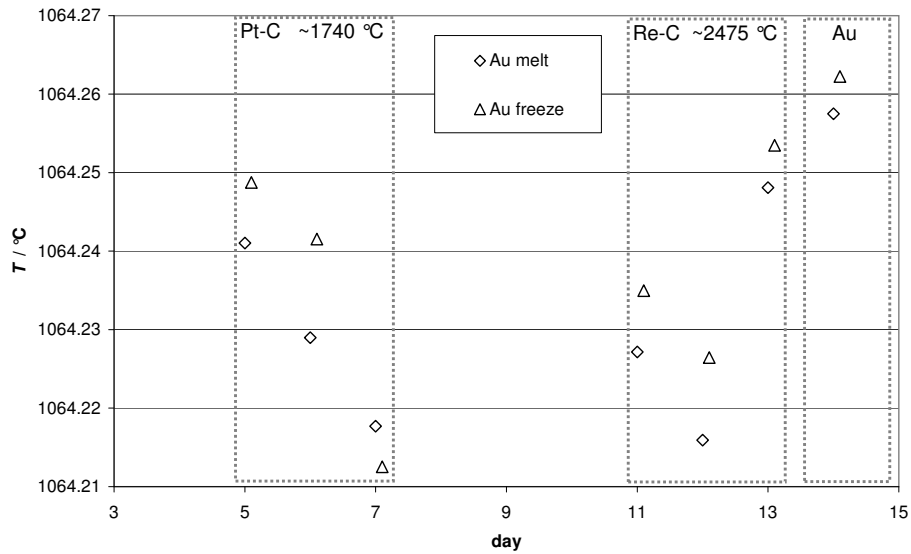


Figure 8.1: Radiation thermometer LP3s stability of the gold freezing and melting temperature during days of measurements at 1740 °C and 2500 °C.

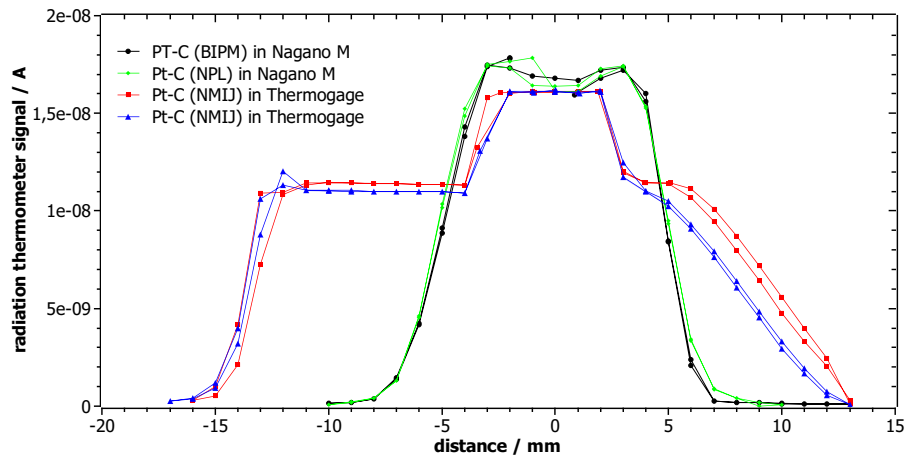


Figure 8.2: Horizontal scans of the Pt-C fixed-points in the two furnaces were used for a correction of the size of source effect.

Size-of-source correction

Horizontal scans across the blackbody aperture were performed with each radiation thermometer for the gold point and for the M-C eutectic fixed-point whilst undergoing a phase transition. Figures 8.2 and 8.3 display the scans for the PTB LP3. These auxiliary measurements were performed to enable corrections for the size-of-source-effect SSE relative to the radiance profile of the NPL gold point to be made. The resulting corrections to the temperature during the melt are listed in Table 8.4. For the PTB LP3 the maximum difference for the furnaces is around 20 mK for Pt-C and of around 50 mK for Re-C.

8.1.4 Results

Typical melt plateaus in the two furnaces are shown in Figure 8.5 and 8.4. From this not only differences between the fixed-points in the same furnace are apparent, also the same cell shows a different plateau shape when used in a different furnace. The NPL plateaus in the NPL Thermo Gauge furnace are generally shorter, after the comparison both cells were inspected. Both cells showed a non-ideal ingot formation, for the Re-C cell the ingot was only partly covering the cavity and for the Pt-C cell it was found to contain only half the expected weight of Pt although the cell appeared to be full when inspected through the filling holes. The two furnaces differ especially at higher temperatures, i.e. for Re-C, the plateaus are shorter and the melt does not end with a clear temperature rise at the end of the plateau.

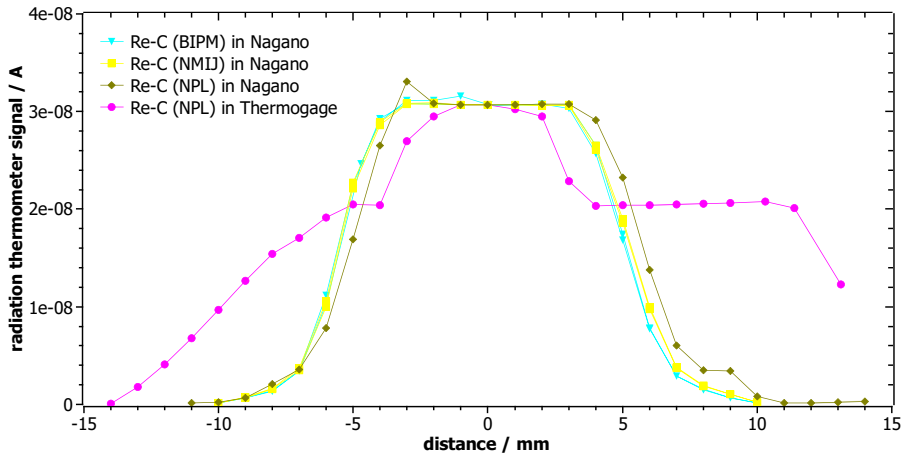


Figure 8.3: Horizontal scans of the Re-C fixed-points in the two furnaces were used for a correction of the size of source effect.

Fixed-point cell	Manufacturer	Furnace	SSE corr./ mK
Pt	NMIJ/BIPM	Nagano	39
Pt	NMIJ/BIPM	Thermo Gauge	18
Pt	NPL	Nagano	36
Pt	NPL	Thermo Gauge	21
Re	NMIJ/BIPM	Nagano	94
Re	NMIJ/BIPM	Thermo Gauge	43
Re	NPL	Nagano	88
Re	NPL	Thermogage	41

Table 8.4: Resulting correction for the radiance temperature of the fixed -point cells relative to the NPL gold point.

The inflection point of the melt was taken to indicate the transition temperature of the fixed point cell. Despite the differences between the cells and furnaces the inflection points were highly repeatable. Figures 8.6 and 8.7 summarize the observed temperature differences to a mean temperature of the various combinations.

The drift and SSE corrected data were used to calculate the temperature differences between respective cells. The differences between the cells are listed in Table 8.5.

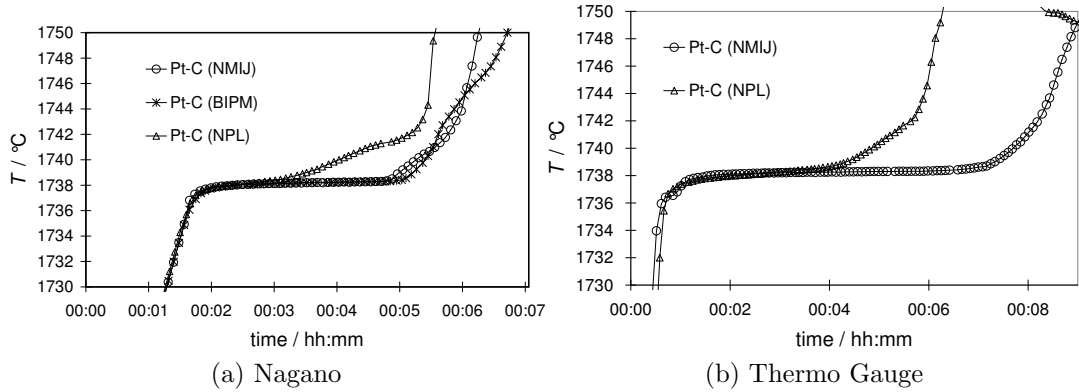


Figure 8.4: Melting curves for the Pt-C fixed-points in the Nagano and Thermo Gauge high temperature furnaces.

8.1.5 Comparison uncertainty

The uncertainty in the comparison of the cells considers the following components: u_1 , the standard deviation of the individual temperature values for the different temperatures steps used to initiate the melt/freeze cycles, which is understood to be a measure of furnace effects, u_2 , the uncertainty in determining the point of inflection of the melting curve, u_3 , the day to day repeatability of the fixed-point cell, which is an estimate for the alignment uncertainty, u_4 , the uncertainty due to Au point drift, which is a measure of the day-to-day stability of the LP3, u_5 , the uncertainty due to differences in cavity emissivity, and u_6 , the uncertainty in the SSE correction.

The components are listed in Table 8.6 for Pt-C and Re-C and the two radiation thermometers.

8.1.6 Discussion

The differences between the cells are all well below the uncertainty of the comparison. This indicates that it is possible to make M-C eutectic fixed-point cells of different designs, in different laboratories, with materials from different suppliers and batches

Day	Radiation Thermometer	Pt-C cell and furnace	Temperature difference / K	Uncertainty of comparison / K
1	LP3 (PTB)	NPL(TG)-NMIJ(NG)	0.02	0.18
2	LP3 (PTB)	NMIJ(TG)-NPL(NG)	0.12	0.18
3	LP3 (PTB)	NMIJ(TG)-BIPM(NG)	-0.12	0.18
1	LP2 (NPL)	NPL(TG)-NMIJ(NG)	-0.03	0.2
2	LP2 (NPL)	NMIJ(TG)-NPL(NG)	0.12	0.2
3	LP2 (NPL)	NMIJ(TG)-BIPM(NG)	-0.08	0.2

Day	Radiation Thermometer	Re-C cell and furnace	Temperature difference / K	Uncertainty of comparison / K
4	LP3 (PTB)	NPL(TG)-BIPM(NG)	-0.24	0.22
5	LP3 (PTB)	BIPM(TG)-NMIJ(NG)	-0.02	0.22
6	LP3 (PTB)	BIPM(TG)-NPL(NG)	-0.12	0.22
4	LP2 (NPL)	NPL(TG)-BIPM(NG)	-0.09	0.24
5	LP2 (NPL)	BIPM(TG)-NMIJ(NG)	0.01	0.24
6	LP2 (NPL)	BIPM(TG)-NPL(NG)	-0.22	0.24

Table 8.5: Temperature differences between the measurements of Pt-C and Re-C cells in the two furnaces. NPL(TG) is the NPL cell realized in the Thermogauge furnace, NMIJ(NG) is the NMIJ cell realized in the Nagano furnace etc. .

Uncertainty component	Pt-C (LP3) /K	Re-C (LP3) /K	Pt-C (LP2) /K	Re-C (LP2) /K
u_1	0.07	0.05	0.04	0.04
u_2	0.02	0.06	0.02	0.06
u_3	0.07	0.05	0.07	0.05
u_4	0.02	0.04	0.04	0.06
u_5	0.01	0.02	0.01	0.02
u_6	0.01	0.03	0.01	0.03
u , k=1	0.1	0.11	0.1	0.12

Table 8.6: Uncertainty budget for the comparison of Pt-C and Re-C fixed-point cells at the NPL.

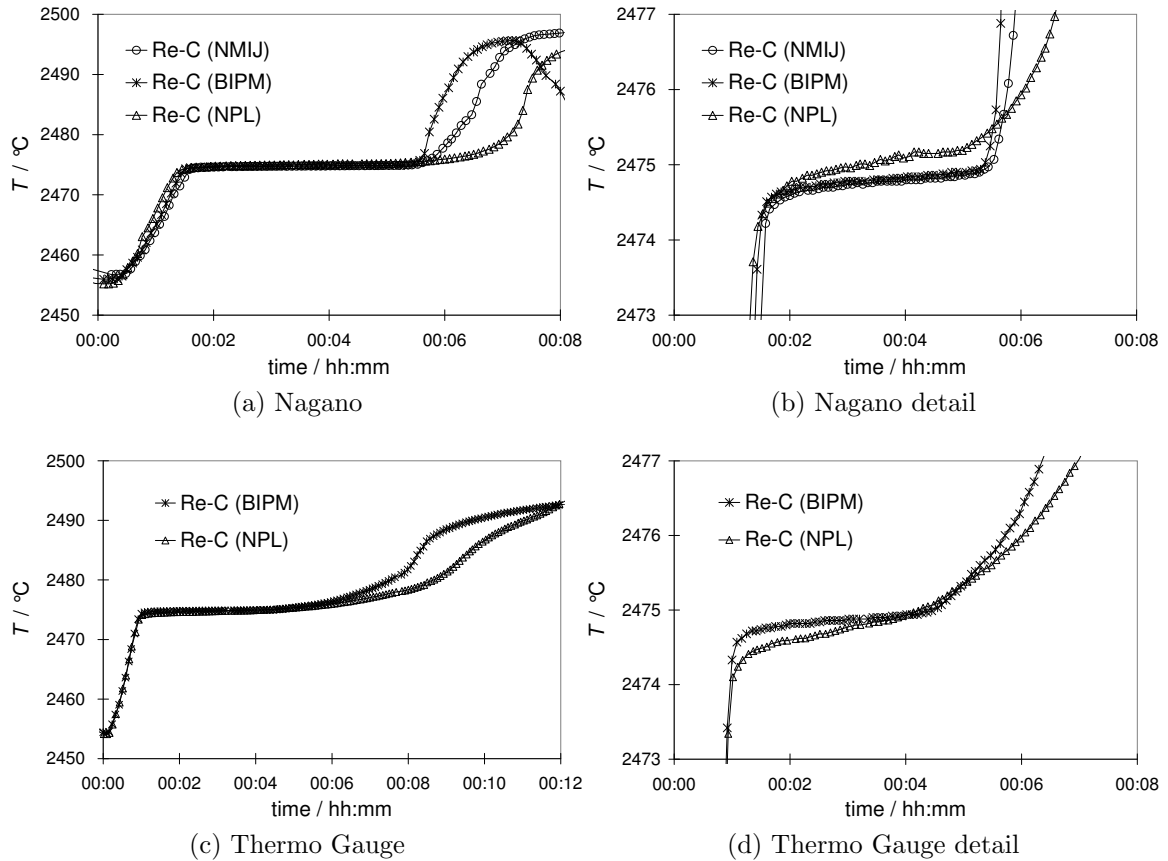


Figure 8.5: Melting curves for the Re-C fixed-points in the Nagano and Thermo Gauge high temperature furnaces.

that are in agreement within a few tenths of a degree even at 2475 °C. Moreover it means that cells can be manufactured that agree with one another to tolerances better than it can actually be measured.

Table 8.7 analyses the results with regard to the maximum temperature difference observed between all the cells in all furnaces or between only a subset of cells measured only in one furnace. The differences between all cells are smallest when only the measurements in the Nagano furnace are compared. The systematic negative differences between the Thermo Gauge and Nagano furnaces for the Re-C results are indicative of furnace effects. This is supported by the fact that there is still a negative difference even when the NPL and BIPM cells are swapped between the furnaces. It can be assumed from comparing the plateau shape, that the Thermo Gauge furnace temperature profile is less uniform than that of the Nagano furnace. This also explains why particularly for the Re-C results, the Nagano temperatures are slightly higher than those obtained when the crucibles were in the Thermo Gauge furnace.

This comparison presented for the first time with a sufficient low measurement

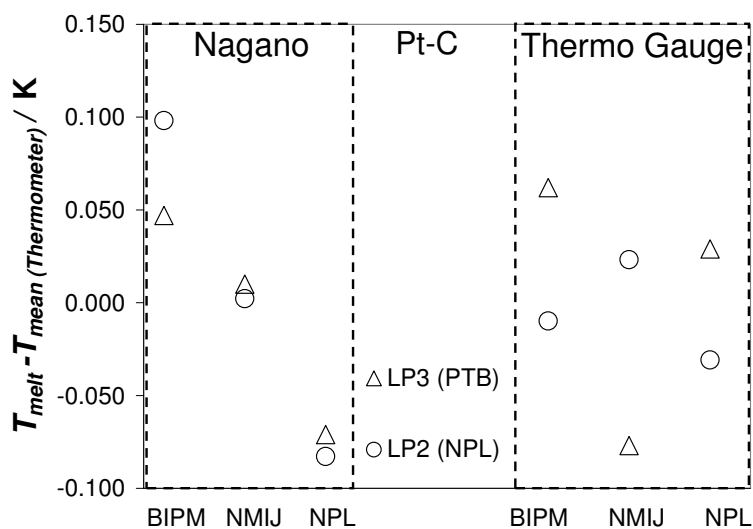


Figure 8.6: Difference of the phase transition temperature of Pt-C from a mean temperature for LP3 and LP2 for each furnace individually . The mean temperature was determined for each radiation thermometer separately.

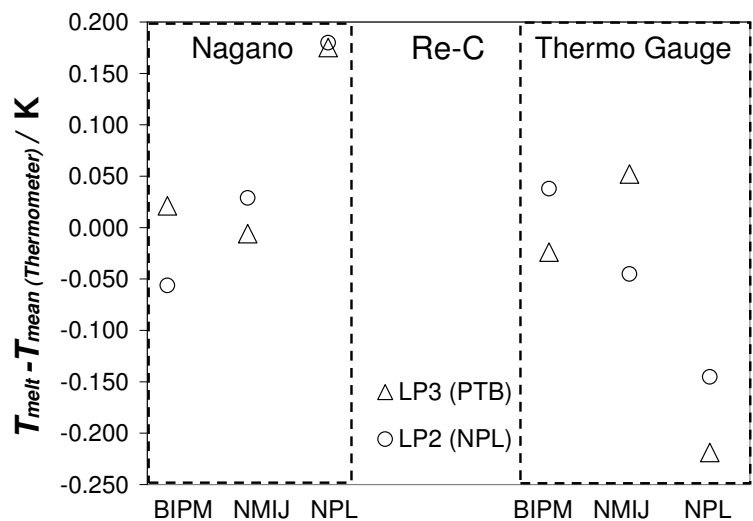


Figure 8.7: Difference of the phase transition temperature of Re-C from a mean temperature for LP3 and LP2 for each furnace individually . The mean temperature was determined for each radiation thermometer separately.

Difference between subset of cells	Used in Furnace	LP3	LP2
Pt-C			
max. ΔT (BIPM,NMIJ,NPL) / K	Thermo Gauge, Nagano	0.139	0.181
max. ΔT (BIPM,NMIJ,NPL) / K	Nagano	0.118	0.181
max. ΔT (BIPM,NMIJ) / K	Nagano	0.037	0.096
max. ΔT (BIPM,NMIJ) / K	Thermogage	0.139	0.033
Re-C			
max. ΔT (BIPM,NMIJ,NPL) / K	Thermo Gauge, Nagano	0.394	0.325
max. ΔT (BIPM,NMIJ,NPL) / K	Nagano	0.181	0.236
max. ΔT (BIPM,NMIJ) / K	Nagano	0.027	0.085
max. ΔT (BIPM,NMIJ) / K	Thermogage	0.076	0.083

Table 8.7: Maximum difference between Pt-C and Re-C cells observed in different furnaces and the same furnace.

uncertainty, that a reproducibility for M-C eutectic high temperature fixed-points at the 100 mK level above 2300 K can be achieved.

The furnace effects observed here advised later comparisons to take the comparability of the used furnaces especially into account when designing and planning a comparison. The relative comparison of M-C fixed-points held at the PTB and presented in the following chapter follows these recommendation by using two identical furnaces of type Nagano. After the comparison the NPL started to improve their furnace by improving its thermal uniformity using graphite felt around the furnace tube [Himert:report]. Furthermore it was realized, that the filling methods had to be improved. A small hole on the side is not suitable for checking whether a cell is completely filled, a filling technique that uses the full inner cell diameter as presented in Chapter 5 is a more suitable technique.

8.2 A relative comparison of Co-C, Pd-C, Pt-C, and Ru-C in two identical furnaces

8.2.1 Outline and set-up of the measurements

A relative comparison of the melting temperature of the eutectic Co-C, Pd-C, Pt-C, Ru-C, and Re-C metal carbon fixed-point cells for radiation thermometry manufactured independently by NPL, BNM-INM, and NMIJ was performed at PTB. The aim of the comparison was a relative comparison of the melting temperatures of the cells solely in order to proof M-C carbon eutectics as reproducible fixed-points. Since in the former comparison at the NPL (Chapter 8.1) effects of the furnace on the melting process could not be excluded, two Nagano furnaces were supplied by the NMIJ (one Nagano S and one Nagano M) and sent with a carrier to PTB. The two Nagano furnaces have been carefully investigated prior to the comparison by the NMIJ and showed a similar temperature homogeneity resulting in a nearly identical performance, excluding possible furnace effects during the comparison. Both furnaces have a single zone utilising carbon-fibre reinforced carbon composite (C/C) material for their heater element their design and working principle is described in Chapter 4.1.2. In order to improve the temperature uniformity across the cell the fixed-point cells were wrapped in 1 - 2 mm graphite felt before being inserted into the furnace and radiation shields were placed behind and in front of the cell.

For the measurements of the radiation temperatures two linear radiation thermometers LP3 with low size of source effect were used, the LP3 80-46 was brought to PTB by the BNM-INM, the LP3 80-05 was provided by the PTB, both with an improved interference filter set-up for measurements at high temperatures having an effective wavelength of about 650 nm (see Chapter 6).

On 14 consecutive days measurements in both furnaces were performed. Table 8.8 gives an overview of the cell-furnace combination used for each day.

For each cell in each furnace 4 melting and freezing plateaus with temperature steps of ± 30 K, ± 20 K, ± 10 K, ± 30 K were measured with each radiation thermometer resulting in a total of 16 melts and freezes per day.

The measurements of the Co-C, Pd-C, Pt-C were performed in "parallel", i.e. both furnaces were equipped with a cell of the same material and during one day the temperatures seen from the radiation thermometers never exceeded the melting temperature of the cell material under investigation by more than 50 K. For furnace temperatures higher than 2500 K the temperature homogeneity of the two furnaces are no longer identical, then only the Nagano M furnace provides the best available conditions and between day 10 to day 13 the Nagano M furnace was exclusively used for the comparison of the Re-C cells and in the Nagano S furnace the Ru-C cells were investigated.

The experimental set-up for the comparison is shown in diagram 8.8 and 8.9.

day	Fixed-point in Nagano M		Fixed-point in Nagano S	
1	Pt-C	NPL	Pt-C	NMIJ-H9
2	Pt-C	INM	Pt-C	NMIJ-H9
3	Pt-C	NMIJ-H9	Pt-C	NPL-B
4	Co-C	NPL	Co-C	NMIJ-6ST1
5	Co-C	INM	Co-C	NMIJ-6ST1
6	Pd-C	INM	Pd-C	NMIJ-6ST4
7	Pd-C	NPL	Pd-C	NMIJ-6ST4
8		-	Ru-C	NMIJ-5ST1
10	Re-C	NMIJ-6ST4	Ru-C	NPL
11	Re-C	NPL	Ru-C	INM
12	Re-C	INM	Ru-C	NMIJ-5ST1
13	Ru-C	NPL	Ru-C	NMIJ-5ST1
14	Pt-C	NPL-A	Pt-C	NMIJ-H9

Table 8.8: Time table for the comparison

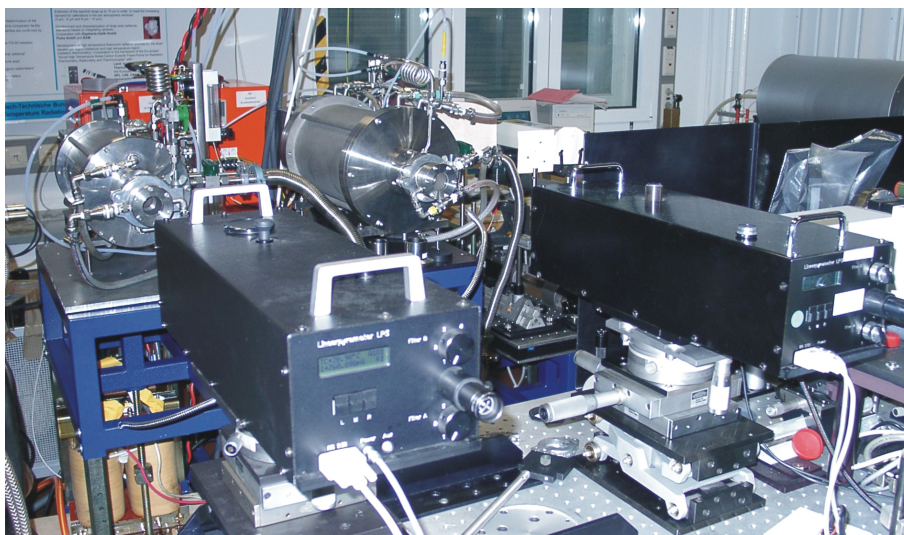


Figure 8.8: The two radiation thermometers LP3 80-45 (BNM-INM, left) and LP3 80-05 (PTB, right) in front of the two Nagano furnaces S (left) and M (right)

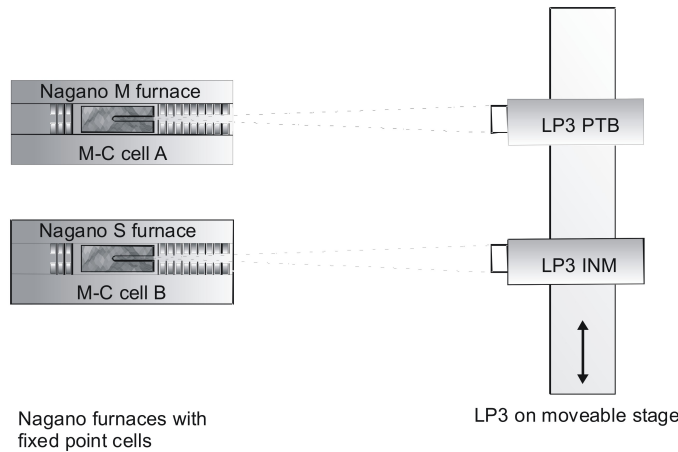


Figure 8.9: Schematics of the experimental-setup

The radiation thermometers were positioned on a movable stage with a distance of 700 mm to the aperture of the cell under investigation inside the furnace. The distance between the radiation thermometers was chosen to be the same as the distance between the two furnaces and enabled simultaneous measurements with both radiation thermometers each looking at a different furnace or cell. In this position the PTB LP3 80-05 is in front of furnace Nagano M and the BNM-INM LP3 80-46 in front of furnace Nagano S. BNM-INMs LP3 would subsequently measure 4 melts/freezes of the cell placed in the Nagano M furnace. The measurements were concluded with PTBs radiation thermometer measuring the Nagano S furnace. This measurement schedule was applied on every day of the comparison.

The Nagano furnace controls are programmable and this allowed a recording of the temperature step patterns and a succeeding identical re-run of the temperature steps for the measurements with the other radiation thermometer on the same and, moreover, on the following day with a different cell of same type, resulting the melt/freezes to be measured with equal start/end conditions for both radiation thermometers even on different days. In order to assess an eventual radiation thermometer drift during the measurements of the Pt-C, Co-C and Pd-C one cell of each type always remained in the Nagano S furnace for the days the specific material was measured. The melting temperature of this cell can be used as a measure of the day-to-day stability of the radiation thermometers during the comparison. On the last day the melting temperature of the Pt-C (NMIJ) was additionally taken to assess the stability of the radiation thermometers during the 3 weeks of measurements. Table 8.9 and Figure 8.10 show the results of this stability assessment. The uncertainty here is determined from the corresponding cells repeatability (see below).

From day 10 to day 13 cells with same filling material were no longer measured in both furnaces, since for temperatures above 2500 K the furnaces temperature

	LP3 PTB		LP3 INM	u / K
	$\Delta T/K$	u / K	$\delta T/ K$	u / K
Pt-C (day 3 - day 2)	0.01	0.03	-0.014	0.023
Co-C (day 7 - day 6)	-0.019	0.025	0.008	0.023
Pd-C (day 7 - day 6)	-0.037	0.021	0.001	0.021
Ru-C with parallel Re-C (day 13 - day 10)	-0.117	0.025	-0.089	0.027
Ru-C (NMIJ) (day 13 - day 8)	0.01	0.017	-0.16	0.022
Ru-C (NPL) (day 13 - day 12)	0.06	0.018	-	-
Pt-C (NMIJ) (day 1 - day 13)	0.014	0.03	-0.024	0.024

Table 8.9: Stability of the radiation thermometers

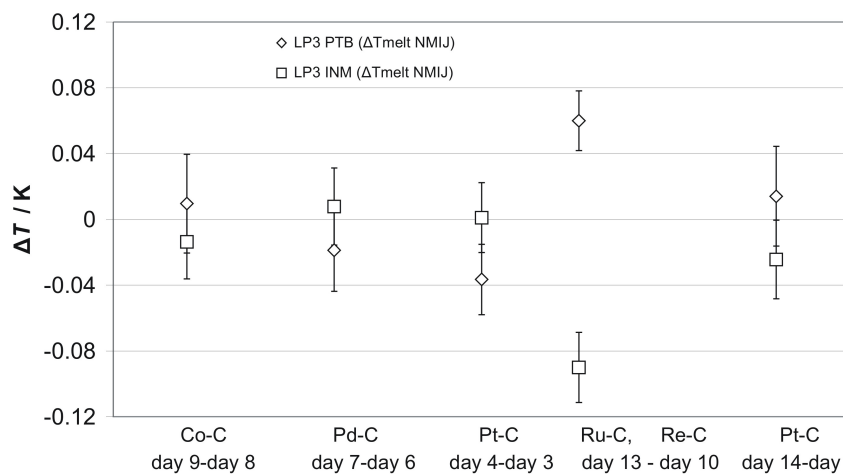


Figure 8.10: Stability of the radiation thermometers during the comparison

homogeneity is no longer identical for both furnaces. On these days the Nagano S furnace contained a Ru-C cell, the Nagano M a Re-C cell. Here no cell could remain unchanged in one furnace. The cells were changed on a day-to-day basis. During the comparison the influence of measurements of the 500 K higher temperatures for Re-C on the same day became apparent for the measurement of Ru-C. The higher temperature caused the radiation thermometer to drift by up to 100 mK at the melting temperature of Ru-C. In order to guarantee the results not to be influenced by this effect additional parallel Ru-C measurements in both furnaces were taken on day 13. However, the stability of the radiation thermometers was affected during for Re-C and Ru-C, possibly due to the use of neutral density filters at temperature measurements above 2500 K, resulting in a drift of about 90 mK.

In the analysis of the comparison only the Ru-C melting temperatures were used that were measured before a measurement of the Re-C that day.

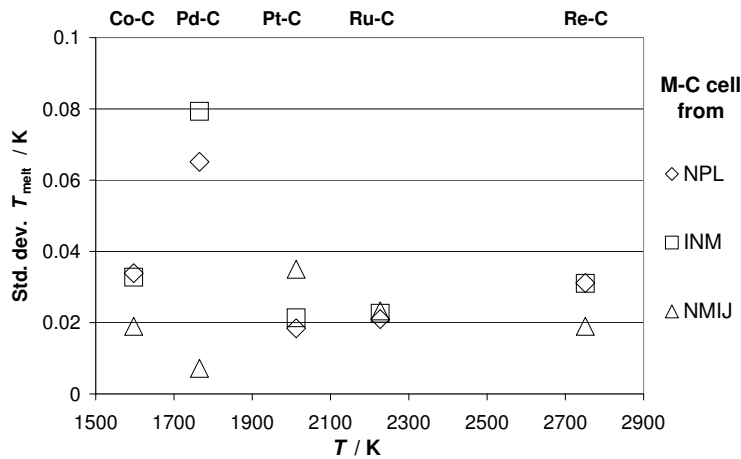


Figure 8.11: Repeatability of single cells

8.2.2 Repeatability of single cells/ effect of temperature steps on the melting

For each cell in the furnace an average melting temperature was determined from the 4 melt/freezes resulting from the temperature step experiments performed. The standard deviation of this average temperature was taken as a measure for the cells repeatability. Figure 8.11 shows the repeatability for all the cells measured in the comparison. The reproducibility for all cells from all manufacturers is better than 80 mK, and apart from the Pd-C cells of NPL and INM, even better than 40 mK.

8.2.3 Relative temperature differences for one filling material

Figure 8.12 and Table 8.10 show the difference from an average melting temperature for the different cells as measured by the different radiation thermometers.

The very similar thermal profile of both furnaces and the identical setup using radiation shields in an identical configuration results in a low size-of-source-effect (SSE) difference between the cells (maximum 15 mK for Re-C). The signal is not corrected for SSE, but the effect is included in the uncertainty budget.

Uncertainty components considered are cell repeatability, size-of-source-effect, uncertainty of inflection point determination and the radiation thermometers stability, which are responsible for the larger uncertainties for Ru-C and Re-C.

Overall the fixed-point cells showed an agreement to within 200 mK for Co-C, Pt-C and Re-C. For Ru-C and Pd-C the agreement is better than 450 mK. The differences between the radiation thermometers showed that for Co-C, Pd-C and Pt-C the melting temperatures for each cell are in good agreement to within 30 mK for both radiation thermometers. The drift of the radiation thermometer during Ru-C and

LP3 (PTB)				
	T / K	T / K	T / K	$u / \text{K} (k=1)$
Co-C	-0.001	0.043	-0.042	0.039
Pd-C	-0.069	0.21	-0.141	0.059
Pt-C	-0.056	0.034	0.022	0.047
Ru-C	-0.026	0.228	-0.202	0.121
Re-C	-0.064	0.084	-0.019	0.123
	NPL	NMIJ	INM	

LP3 (INM)				
	T / K	T / K	T / K	$u / \text{K} (k=1)$
Co-C	0.005	0.056	-0.061	0.038
Pd-C	-0.066	0.195	-0.129	0.051
Pt-C	-0.067	0.039	0.027	0.043
Ru-C	-0.013	0.164	-0.151	0.095
Re-C	-0.017	0.091	-0.074	0.097
	NPL	NMIJ	INM	

Table 8.10: Differences of cells inflection point temperature to the materials average inflection point temperature

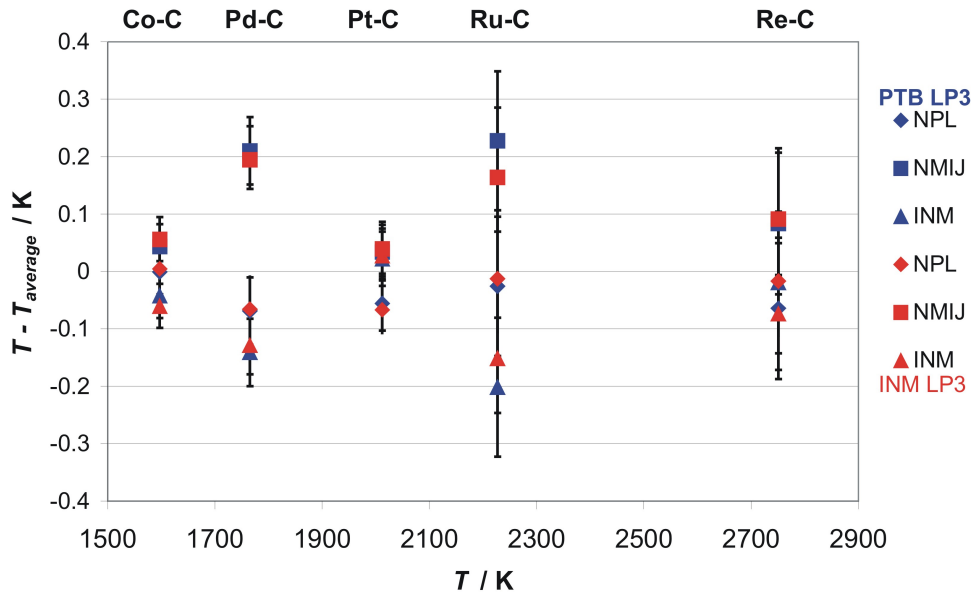


Figure 8.12: Differences of cells inflection point temperature to the materials average inflection point temperature, results from measurements of PTB LP3 in blue and INM LP3 in red

Metal powder	NPL purity available	INM purity available
Co	99.998	99.998
Pd	99.998	99.998
Pt	99.999	99.999
Ru	99.95	99.95
Re	99.999	99.999

Table 8.11: Best available purities for metal powder used for production of the cells here.

Re-C measurements is also apparent in the larger difference of 80 mK in the inflection point temperature determined with each radiation thermometer for Ru-C.

8.2.4 Discussion

A remarkable result of this comparison is the good agreement of within 200 mK of the Co-C, Pt-C and Re-C cells manufactured independently by the three institutes.

It has to be noted that the calculation of an average melting temperature can here not be understood as the approximation to the materials true melting temperature. And therefore the difference of a cells melting temperature to the average melting temperature cannot be understood as a measure for the quality of a cell. This conclusion could only be drawn if the data would scatter around an average temperature, but as can be seen from Table 8.10 and Figure 8.12 for all materials the cells which showed the highest melting temperatures were produced by the NMIJ and this hints to an understanding of the temperature between the cells as measures of purity and cell production.

Taking Pd-C as an extreme example for the differences in cell performance: for this material the melting temperature of the NMIJ cell is nearly 300 mK higher than that of INM and NPL cells, additionally the INM and NPL Pd-C cells show the poorest repeatabilities in this comparison.

The Ru-C cells show the largest differences with up to 400 mK for the melting temperatures. The nominal purity of the Ru metal powder available for cell production was significantly lower than the purities available for the other metals that were used for building M-C cells (see Table 8.11 for an example).

The radiation thermometers instabilities when changing the comparison schedule from parallel to serial show that the work presented here was performed at the limit of measurement capabilities which are available even at an NMI level. However this can not disguise the significantly larger differences of up to 450 mK for Pd-C and Ru-C, these results are confirmed in experiments on thermodynamic temperature determination of the same cells that are described in the next chapter of this work. The differences of up to 450 mK for Pd-C and Ru-C prove the demand for further

research looking at the effect of impurities on the melting temperature of M-C eutectics.

As the temperature homogeneity of the furnaces has been checked to be identical and the comparison has been performed in parallel, this result has to be attributed to the different manufacturing process of the metal-carbon cells at the different institutions. The purity of all materials used at the different institutions has nearly been the same. Therefore, probably the manufacturing process at the NMIJ has been the most sophisticated one and was adopted for the cell produced in this work.

8.3 Evaluation of two fixed-point cell designs for Cu, Pt-C and Re-C

The comparisons in the preceding chapters investigated both differences between cells of same design, and on the other hand radiometric methods of determining the materials melting temperature with low measurement uncertainties. A good agreement between cells was achieved for small aperture fixed-point cells, however for the large aperture fixed-point cells manufactured by the VNIIOFI the melting plateau duration was shorter and melting occurred over a wider temperature range. After these comparisons it remains still unclear whether these differences are due to impurity contamination of the large aperture fixed-point cells, either during handling of the pure metals or already from the supplier, or from the combination of a larger cell set-up in a furnace with a always limited temperature uniformity. Or whether an imperfect filling of the fixed-point cell can explain the observed differences. For this reason, the systematic differences between large and small aperture fixed-point cells has been assessed. Altogether six fixed-point cells were manufactured. Three cells were of small and three of large aperture design, for Cu, Pt-C and Re-C one large and one small aperture cell was manufactured. Design and manufacture of the cells are described in Chapter 5. The six Cu, Pt-C and Re-C fixed-point cells of small (SA) and large (LA) aperture design were evaluated in several different schemes, which are described in the following. In order to prove the quality of the cells and to detect impurity intake due to the filling method the small aperture cells (SA) were first compared to cells from the NMIJ, whose quality had been proven in the earlier comparisons. Then SA and LA cells of same material were compared using a radiation thermometer (i.e. in radiance mode). Finally differences for the LA cells when measured by a radiation thermometer and a filter radiometer in irradiance mode were looked at. Table 8.13 lists all the cells investigated together with the amount of metal used for filling and remarks special design features.

The presentation here focuses on a qualitative analysis of the plateau shapes during the melting for Pt-C and Re-C and the freezing for Cu.

Cell comparison with a radiation thermometer

8.3.1 Comparison of small aperture cells

To verify the quality of the small aperture cells, and thereby the quality of the material lot used, a comparison was firstly made between the SA cell pairs with a radiation thermometer. For Cu and Pt-C the Nagano M and S furnaces were used, while for Re-C the VEGA BB3500YY was used together with the Nagano M furnace.

Fixed-Point type	Cell ID	Nominal purity / Supplier	Lot #	Cell design	Number of C/C layers	Metal Mass
Cu	6ST-3	0.99999 Alfa Aesar	D25N18	SA	3	21 g
	PTB I				2	27 g
	PTB LA I		J21Q086	LA	1	113 g
Pt-C	H14	0.99999 Tanaka Kikinzoku	u09-032	SA	2	55 g
	PTB I				2	65 g
	PTB LA I		u12-085	LA	2	71 g
Re-C	6SS-6	0.99999 ZKMTW China	05-KT-001	SA	2	64 g
	PTB I				2	57 g
	PTB LA I				LA	2

Figure 8.13: Overview of cells measured and compared.

Cu

Cu PTB I was set-up in the Nagano M furnace and the Cu 6ST-3 fixed-point cell in the Nagano S furnace. The furnace temperature was varied with temperature steps of ± 20 K, ± 10 K, ± 20 K, where the temperature values are the constant furnace set-point offsets relative to the fixed-point temperature for the melt and the freeze. Figure 8.14 shows a typical melt and freeze curve initiated by a ± 20 K furnace temperature step. The repeatability of the freezing temperature, evaluated by the standard deviation of the highest temperature during the freeze, was for both cells better than 10 mK and the temperature difference between the two cells was within 20 mK.

Pt-C

Pt-C PTB I was set-up in the Nagano M furnace and Pt-C H14 in the Nagano S furnace. With temperature steps of ± 30 K, ± 20 K, ± 10 K melting and freezing cycles were initiated. Figure 8.15 shows a typical melting plateau for a temperature step of ± 20 K. The repeatability of the melting temperature, evaluated at the inflection point, for 3 melts was 22 mK for Pt-C PTB I and 11 mK for Pt-C H14, the melting temperatures differed by less than 30 mK. For both cells the melting range, evaluated as the melting plateau slope at the inflection point times the plateau duration, is below 250 mK and the melt finishes with a sharp rise in temperature, which indicates an equally good quality of the cells and the furnace temperature uniformity. Of the two cells, Pt-C PTB I contains a 20% larger metal ingot, which is directly reflected in the longer melting plateau for this cell.

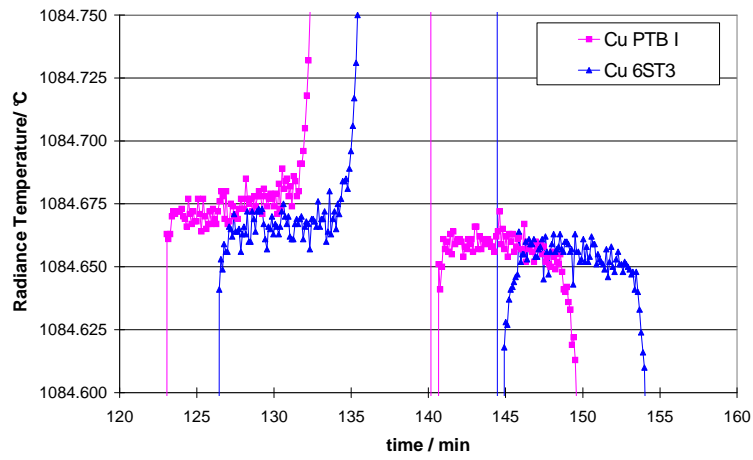


Figure 8.14: Typical melting/freezing plateau for small aperture Cu fixed-points

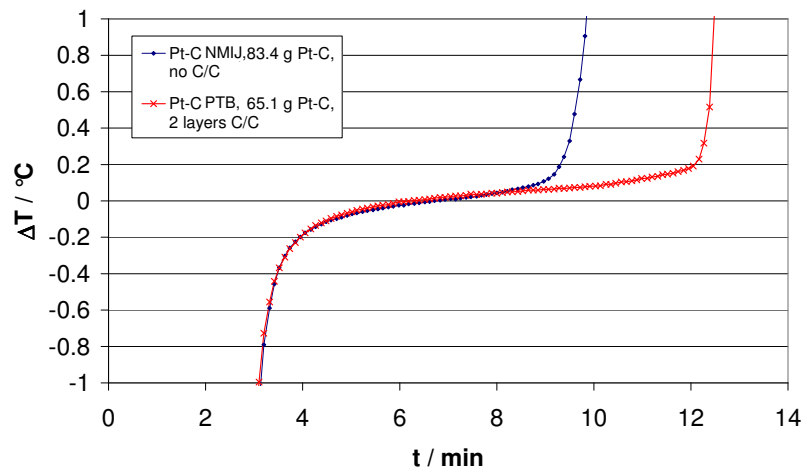


Figure 8.15: Typical melting/freezing plateau for the small aperture Pt-C fixed-points

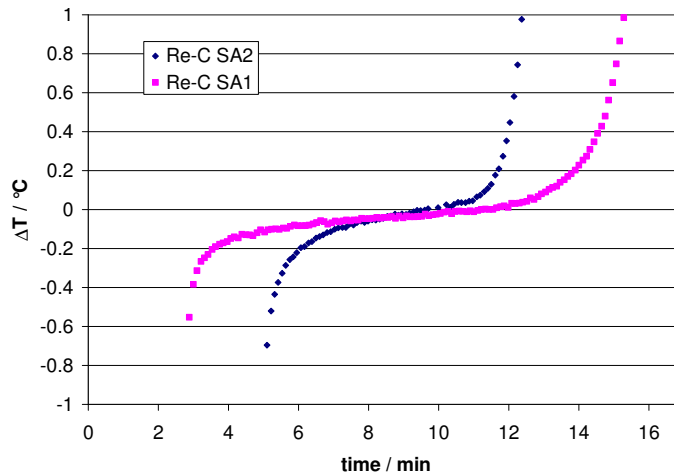


Figure 8.16: Typical melting/freezing plateau for the small aperture Re-C fixed-points.

Re-C

Here, the Re-C PTB I cell was set-up in the BB3500YY furnace and compared to the Re-C 6SS-6 cell in the Nagano M furnace. With temperature steps of ± 30 K, ± 20 K melt and freeze cycles were initiated. Figure 8.16 shows a typical melting plateau for a temperature step of ± 20 K. The repeatability was 16 mK for Re-C PTB I cell and 12 mK for Re-C 6SS-6. For both cells the melting range is below 200 mK and for both cells the melt starts and finishes sharply.

8.3.2 Comparison of small and large aperture cells for Cu, Pt-C and Re-C

In the next step the small (SA) and large aperture (LA) cells were compared with a radiation thermometer. Only cells with the same material lot were chosen, so that an effect of difference in material purity could be excluded. For this, the LA cells were placed in the VEGA BB3500YY furnace while for the SA cells the Nagano M furnace was used.

Cu

Figure 8.17 shows typical plateaus for a temperature step of ± 20 K. A similar melting and freezing behaviour for both fixed-point-cell designs is observed. For the large aperture cell the temperature is stable during the freeze within 20 mK over a period of more than 15 minutes. The repeatability of the freezing temperature observed was 5 mK for the large aperture cell. Both cells show an agreement of better than 20 mK for the freeze. Although the mass of the copper ingots differ largely for both cells, the plateau duration is similar.

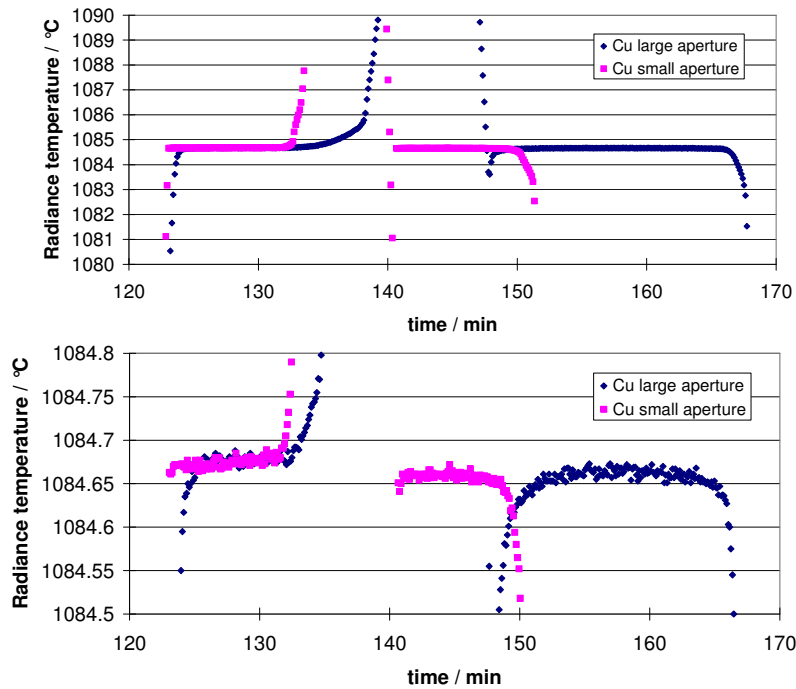


Figure 8.17: Comparison of SA and LA Cu fixed-point cell.

Pt-C

For Pt-C the observed melt and freezes are given in Figure 8.18 for step changes of the furnace temperature of ± 20 K. For the LA cell the melting and freezing plateau shows different principal features: 1) the duration is significantly shorter, 2) the melting range is larger than 1 K, 3) the temperature rise at the end of the melt is not sharp and 4) the temperature rise/fall after the melt and freeze do not start steadily with a continuous slope instead several structural features are seen. The repeatability of the melting temperature for the LA cell was found to be 74 mK. The LA cell showed a 450 mK lower temperature than the SA cell.

Re-C

For Re-C a typical melting and freezing curve is depicted in Figure 8.19 with a temperature step ± 30 K. In this case, the melt is not only shorter for the LA cell, but also several K lower in temperature for the large-aperture cell. Furthermore, the melting range is larger than 5 K. The repeatability of the Re-C LA cell was 94 mK.

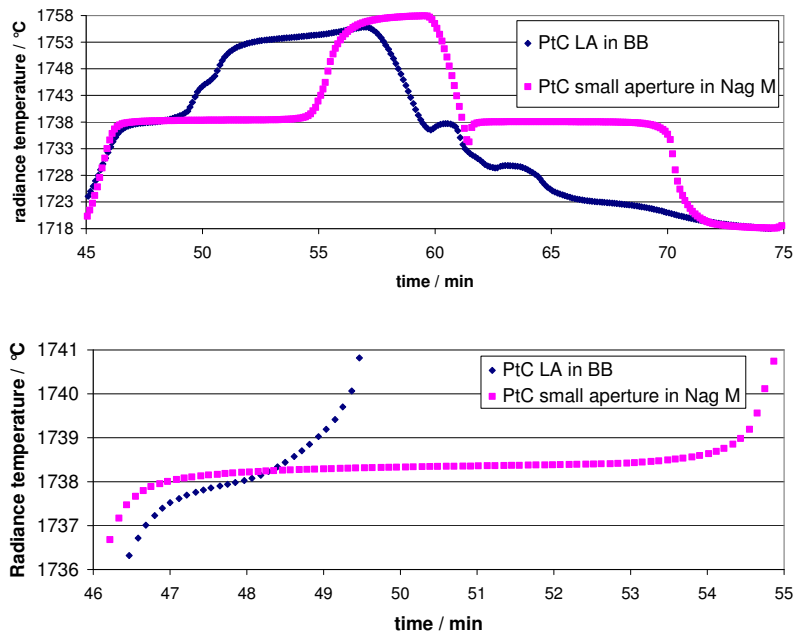


Figure 8.18: Comparison of SA and LA Pt-C fixed-point cells.

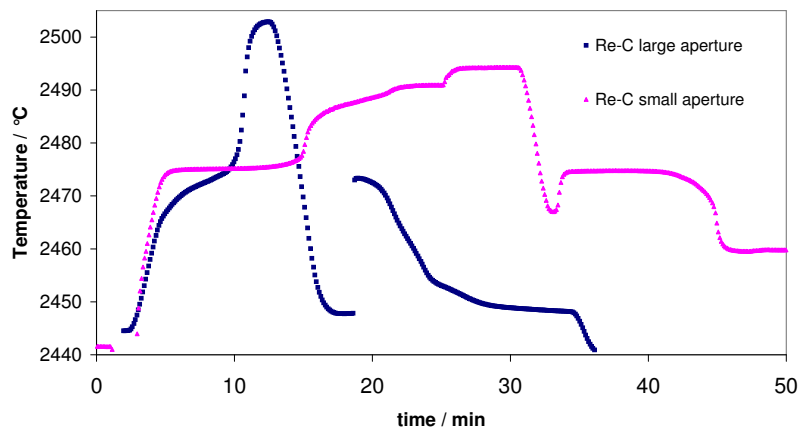


Figure 8.19: Comparison of SA and LA Re-C fixed-point cell.

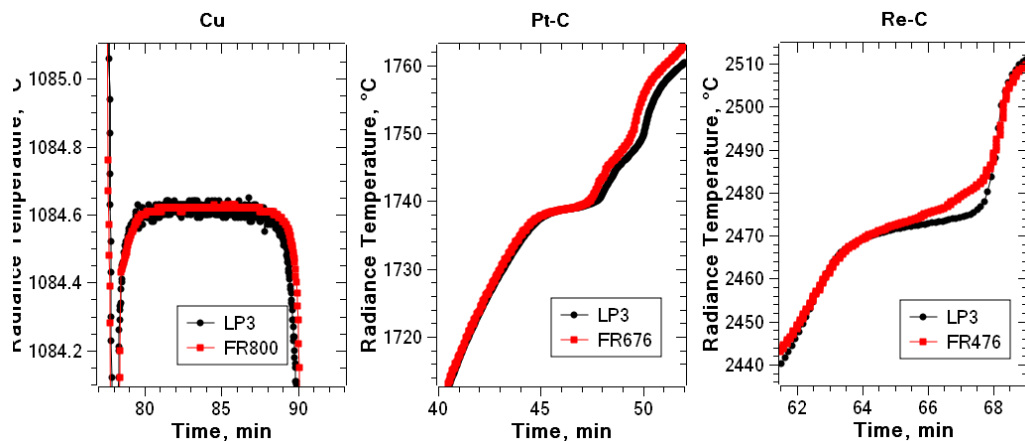


Figure 8.20: Comparison between filter radiometer and radiation thermometer measurements for the large aperture cells of Cu, Pt-C and Re-C.

8.3.3 Comparison of radiation-thermometer vs. filter-radiometer measurements for LA cells

For each material the LA cells were compared with respect to radiometric differences in plateau shape when measured in radiance (i.e. with a radiation thermometer) or irradiance (i.e. with a filter radiometer) mode. For Pt-C and Re-C the cells were measured at the NMIJ using a filter radiometer with central wavelength of 476 nm. Here, the distance between the two apertures was around 1010 mm. Cu and Pt-C cells were measured at the PTB using filter radiometers at 676 nm and 800 nm and a distance of around 1115 mm between the two apertures. The cells were first measured with the filter radiometer, then the precision aperture in front of the furnace was removed and a set of measurements with the radiation thermometer followed. Typical melting/ freezing plateaus that were initiated with step changes in the temperature furnace of ± 20 K are plotted in Figure 8.20. While for Cu nearly identical freezing plateaus are observed, differences in the melting plateau for the other two LA cells are apparent. For Pt-C the differences are pronounced at the end of the melt when the temperature rises and for Re-C the temperature plot even shows a different slope during the melt for radiation thermometer and filter radiometer.

8.3.4 Discussion

Comparison of SA cells

The aim of the comparison between the small aperture cells was to evaluate their performance in order to detect any principal problems with cell design, handling of materials in terms of impurity intakes, ingot formation and thermal uniformity and the stated purity of the used metals and graphites given by the supplier. No

principal differences in respect to poorer performance were observed between the two cells for Cu, Pt-C, and Re-C. Therefore, it can be concluded that the metals are of sufficient purity and that the routines for filling and handling were adequate to the well established procedure at the NMIJ. This conclusion is of particular importance when trying to understand the results of the comparisons between small and large aperture cells.

Comparison of SA and LA cells

The Re-C and Pt-C LA cells exhibited lower temperatures and larger melting ranges. All three showed relatively shorter plateau durations. The differences in plateau temperature and melting range between LA and SA cells have to be related with the ingot formation, impurity intake during filling and insufficient temperature homogeneity of the cavity and the furnace used for the LA cell. In contrast to the Cu point cells, which have a more uniform formation of the ingot and therefore expectedly a more homogeneous temperature distribution across the cavity during the freeze, the agreement of the two cells for Pt-C and Re-C is poor. This may be explained by the imperfect formation of the ingot around the cavity, seen in Figure 5.5.

It is likely that the large difference for Re-C moreover is caused by intake of impurities during the filling stages of the hyper-eutectic ingot LA cell. This statement is supported by an observation that for the first melts and freezes a rapid decrease for both melting and freezing temperature was observed for this cell.

In earlier studies it has been shown that the cooling of the cavity wall that sees the colder environment outside, increases drastically with temperature [JLBY⁺04]. The effect is a non-uniform temperature drop across the cavity wall that creates a temperature inhomogeneity along its inner surface. Furthermore, the effective emissivity of the radiator is affected by the temperature gradient in the furnace outside the cavity and also inside along the cavity wall [Blo07]. From an analytical model temperature drop difference and radiance temperature difference of up to 400 mK and 250 mK, respectively, between fixed-point cells with a 3 mm and an 8 mm aperture can be expected for Re-C [JimenoLargo:2004]. The temperature difference observed here for the Re-C LA and SA cells is an order of magnitude larger, even though the LA cavity is longer than the one treated in [JL07].

In case of the Re-C cells temperature drop effect and the effective emissivity effect cannot explain the observed difference. However, the model deals only with uniform temperature distribution around the ingot, and therefore it would be of interest to model the transient melting curve in the presence of non-uniform ingot shapes, or non-uniform melting of the ingot due to temperature non-uniformity. The differences observed here between large and small aperture cells are larger. However, it is likely that the large difference for Re-C moreover is caused by intake of impurities. In hindsight it can unfortunately only be speculated whether the origin of this

contamination was due to the manufacturing procedures of this cell in particular or is connected with the condition of the furnace that was used at that time. Although these cells have deficiencies in plateau shape and show large differences in melting temperature to their small aperture counterparts, their melting temperature is in both cases highly reproducible.

The plateau duration for the LA cells are only slightly longer (Cu) or shorter (Re-C, Pt-C) than the SA cells, even though it contains ingot with greater mass. However, one should realize that it is not the mass that is directly related to the plateau duration, but the ingot thickness around the cavity (and the temperature difference across it). The LA cells have roughly the same thickness (Cu, Re-C) or 30 % thinner (Pt-C) ingot as compared to the SA cells, and if one considers the porosity of the hyper-eutectic ingots (Re-C, Pt-C), the effective thickness is even thinner, and this explains the relatively short plateau durations.

Comparison of radiation-thermometer vs. filter-radiometer measurements

Obviously, these differences in plateau shape for Pt-C and Re-C will lead to different temperatures for the measurement with radiation thermometer and filter radiometer for the inflection point during the melt, which is generally taken as a measure for the melting temperature of an M-C eutectic fixed-point. Radiance and irradiance mode differed in these experiments by the area on the cavity bottom that is seen from the instrument. When focussed at the front aperture of the fixed-point cell the LP3 has a measurement spot size of around 1 mm in diameter at the bottom of the cavity. Whereas for the filter radiometer in conjunction with a 3 mm diameter precision aperture in front of the furnace irradiance from an area of around 5.5 mm in diameter at the bottom of the cavity is detected. Ideally, the temperature radiation across the aperture area of a black-body fixed-point cell is very uniform and both instruments measure an identical plateau. This assumes both, a small temperature gradient along the crucible wall and a, to the radial symmetric centre of the cavity, concentrically proceeding melt front during the phase transformation. Otherwise, any temperature difference along the cavity wall will influence the measurement with the filter radiometer because of its wider field of view, whereas for the LP3 less influence might be detectable. From the discrepancies here, a non-ideal radiance distribution during the phase change has to be concluded for the large aperture cells of Pt-C and Re-C. This finding is in contrast to earlier investigations that have been reported regarding the homogeneity of the radiation field during the phase change [Woo04] and opposes a common argument for M-C eutectic cells in radiometry, which states, that even for a non-ideal plateau shape and with a temperature gradient of the furnace, during melt and freeze the radiating field will be highly homogeneous. It has to be noted, that the fixed-point cells investigated here are special in that the metal-carbon layer that surrounds the cavity is with 3 mm particular thin and due its slim shape more easily affected by non-ideal temperature distribution in the furnace.

Conclusion

In this chapter it was demonstrated that an 8 mm cavity design could be implemented in a 25-mm-tube furnace and measured with a filter radiometer using a 3 mm precision aperture in front of the furnace. The metal-carbon eutectic LA cells showed relatively poor plateaus as compared to SA cells. Possible causes are:

1. the non-ideal cell design of the LA cells, which leaves only a narrow channel around the cavity for the metal ingot, resulting in an imperfect cell manufacture, with a non-continuous metal ingot for Pt-C and Re-C,
2. contamination during ingot handling in the hyper-eutectic filling stage, and
3. an insufficient temperature uniformity of the furnace, which has a larger effect on the longer LA cells.

The cause for the observations made here should be further investigated, and improvements in furnace-temperature homogeneity, cell design, and cell fabrication technique are necessary. When this is accomplished, a direct irradiance mode measurement to determine the M(C)-C eutectic fixed-points' thermodynamic temperature becomes possible.

9 Thermodynamic temperature determination of M-C eutectic fixed point cells

The experiments described so far focused on relative differences between the fixed point cells under investigation using a radiance mode radiation thermometer. However, for making use of metal-carbon eutectics as fixed points their absolute temperature has to be known. A measurement of the thermodynamic temperature of the phase transition above 2000 K can be performed with sufficiently small uncertainties only by radiometric methods. And for this, in principle, two different approaches are possible: measurement of spectral radiance or irradiance of the eutectic cell. Once a radiometer is calibrated radiometrically with sufficient low uncertainties, both methods can be applied for determining the phase transition temperature.

Due to the small diameters of the radiating cavities of eutectic fixed-points, so far only measurements in the radiance mode have been performed. However, a precise radiometric calibration of a radiometer that measures spectral radiance such as radiation thermometer is complex [Yoo06]. The development of eutectic fixed-points with sufficiently large radiating cavities at the VNIIOFI have made non-imaging irradiance measurements of the transition temperature of eutectic fixed-points possible. These measurements are described in the first part of this chapter. In the second part low uncertainty filter radiometry is connected to small aperture cells via a radiance comparison of two blackbody sources using a radiation thermometer.

9.1 Measurements of thermodynamic temperatures using large aperture fixed-point cells of Re-C, ZrC-C and TiC-C

In this section the first absolute irradiance measurements of the large aperture eutectic fixed-point cells are presented. First these special fixed-point cells developed at the VNIIOFI are described, and then the experimental set-up and the applied detectors are introduced. The measurement in this chapter instigated further studies on the comparability of the large and small aperture cell design described in the Chapter 8.3.

Material	Purity	Mixture Metal - Carbon in parts of weight	Supplier
Re	0.99995	1.9 %	Lanhit Ltd.
Ti	0.9998	25 %	Lanhit Ltd.
Zr	0.9994	20 %	Lanhit Ltd.
C	0.999998		Grafi Ltd.

Table 9.1: Material purities and mixture proportions

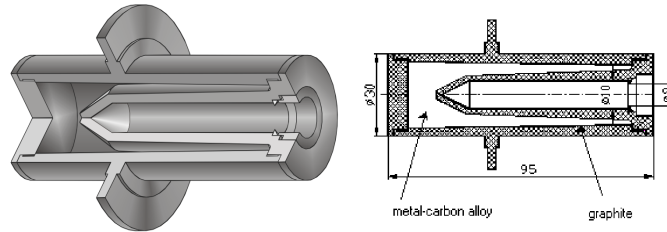


Figure 9.1: Schematics of the blackbody configuration, showing the eutectic fixed-point, the stray light baffles and the precision aperture.

The large aperture eutectic fixed-point cells were developed by the VNIIOFI [SKS⁺05] and designed to fit in the high temperature blackbody BB3200pg[SKK⁺97]. In contrast to the commonly used eutectic fixed-points, which have geometrical dimensions of approx. 25 mm x 45 mm, the cells used here have a length of approx. 95 mm and a diameter of 30 mm, as can be seen in Fig. 9.1 and a radiating cavity of 10 mm in diameter, which allows an irradiance measurement based on a filter-radiometer and a 3 mm precision aperture in front of the furnace. The cavity bottom opening angle is about 53 deg. The emissivity of the crucibles was calculated to be 0.9997, assuming an isothermal cavity and a 0.15 diffuse reflection of graphite [KSO⁺05]. All crucibles were made from fine-grained pure graphite (> 99.995%) and then filled with pure carbon and metal powders with the purities given in Table 9.1 as certified by the suppliers.

The cells can be set-up in the HTBB3200pg furnace without an additional holder directly as part of the pyrolytic graphite ring system, see Fig.9.2.

A radiating cavity of 10 mm is realized in this cell, which is more than a factor of three larger than the 3 mm diameter usually obtained with smaller cells. This large radiating area offers the possibility to perform irradiance measurements using absolutely calibrated filter radiometers. If the spectral irradiance is measured in absolute units under a well-defined geometry and the emissivity of the cavity is known, it is possible to determine the thermodynamic transition temperature of the eutectic material via Planck's law of thermal radiation as described in Chapter 2.1.

Three eutectic fixed-point materials have been investigated. One metal-carbon eutectic, namely Rhenium-Carbon, with a melting and freezing temperature around

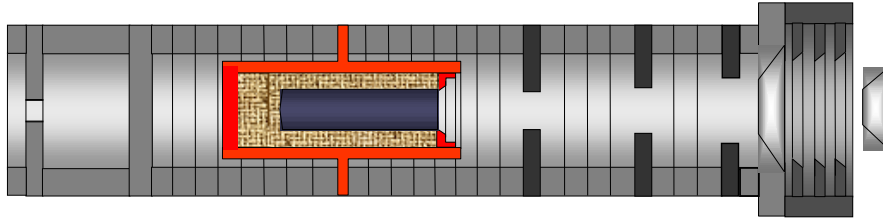


Figure 9.2: Design of the large area irradiance cells made by VNIIOFI

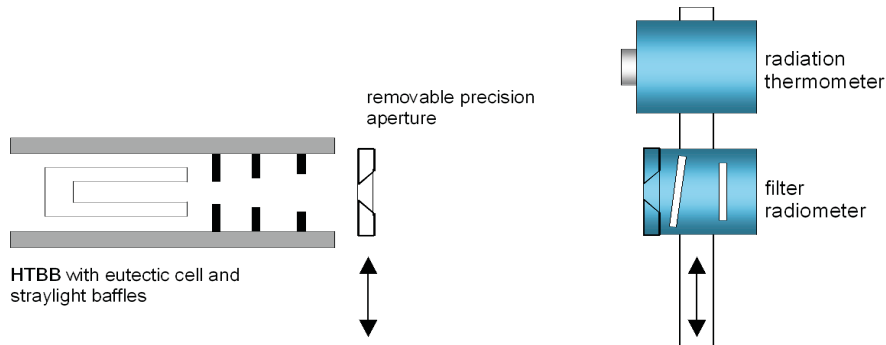


Figure 9.3: Schematics of the blackbody configuration, showing the eutectic fixed-point, the stray light baffles and the precision aperture on the left and the two types of detectors on the right.

2745 K and two metal carbide-carbon eutectics, namely Titanium carbide-Carbon and Zirconium carbide-Carbon, with melting and freezing temperatures around 3030 K and 3150 K. More details about the cells and the fixed-point materials can be found in (Khlevnoy 2005).

The large cavity diameter allows a precision aperture of around 3 mm in diameter to be positioned in front of the cavity outside the furnace, defining the radiating area. A schematic of the experimental set-up is given in Fig. 9.3.

The precision aperture, defining the radiating area of the fixed-point is positioned outside the HTBB cavity to enable a good temperature stabilisation and is for this reason also placed in a water cooled housing which allows a temperature controlling of typically 23 °C. Due to the long distance between the aperture and the fixed-point cell, the precision aperture has to be as small as 3 mm in diameter, to view only the bottom of the radiating fixed-point cell. The large distance between the radiating cell and the precision aperture requires the application of straylight baffles, which, are even more important for the additional radiance temperature measurement using the radiation thermometer LP3. For these radiance temperature measurements the precision aperture is removed from the blackbody and the LP3 is focused onto the entrance aperture of the fixed-point cell. The stray light baffles inside the HTBB

minimize the radiation originating from outside the fixed-point cell and reaching the filter radiometer and the radiation thermometer.

Two types of detectors have been used for the determination of the melting and freezing temperatures. A radiation thermometer LP3 for measuring temperatures according to the International Temperature Scale of 1990 (ITS-90) and filter radiometers for measuring thermodynamic temperatures.

The radiation thermometer LP3 has been calibrated traceable to the ITS-90. The standard uncertainty of the temperature measurement using the LP3 is given in Table 9.2. This table also shows the standard uncertainty of a radiation thermometer TSP of the VNIIOFI, which was used for measurements of the same cells at the VNIIOFI in Russia shortly before the measurements at PTB.

T / K	u(TSP) / K	u(LP3) / K
2800	0.6	0.75
3000	0.75	0.86
3200	0.8	0.98

Table 9.2: Standard uncertainty (k=1) of the ITS-90 temperature measured with the TSP and the LP3

The spectral irradiance responsivity of the filter radiometers has been calibrated traceable to the cryogenic radiometer of the PTB (Chapter 2.1), therefore yielding thermodynamic temperatures. Two different types of filter radiometers were used: Three narrow-band interference filter radiometers with center wavelengths around 676 nm, 800 nm, and 900 nm, and one broad-band glass filter radiometer, having a center wavelength around 550 nm [FFS96].

The standard uncertainty of the thermodynamic temperatures measured with the filter radiometers, including the uncertainty in the spectral responsivity of the filter radiometers, ranging from $5 \cdot 10^{-4}$ up to $2.5 \cdot 10^{-3}$, the uncertainty of the diffraction correction, and the uncertainty due to the geometry is given in Table 9.3.

T / K	u(FD17) / K	u(FR 676) / K	u(FR 800) / K	u(FR 900) / K
2800	0.32	0.39	0.46	0.51
3000	0.36	0.45	0.52	0.58
3200	0.41	0.5	0.59	0.66

Table 9.3: Standard uncertainty (k=1) of the thermodynamic temperature measured with the filter radiometers

Temperature drop

Due to the large radiating aperture of the irradiance mode cells the temperature drop at the bottom due to radiative cooling has to be taken into account. This temperature drop has been measured to 70 mK for ZrC-C. The measured values were not corrected for this temperature drop, but the value has been included in the uncertainty budget.

9.1.1 Measurements

In a first step, the TiC-C and ZrC-C eutectic fixed-point cells were measured at the VNIIOFI using the broad-band filter radiometer FD17 from the PTB and the TSP radiation thermometer from the VNIIOFI. Then the TiC-C and ZrC-C cells, and additionally Re-C eutectic fixed-point cells, were measured at the PTB using the broad-band filter radiometer, three narrow-band interference filter radiometers and an LP3 radiation thermometer. A schematics of the experimental set-up used at the VNIIOFI and the PTB is presented in Figure 9.3. The precision aperture in front of the HTBB has a diameter of 3 mm, while the apertures of the filter radiometers are approx. 5 mm in diameter, the distance between the two apertures was about 1110 mm. For the measurements at the VNIIOFI and the PTB the same 3 mm aperture was used. During the measurements with the radiation thermometers the aperture was removed from the HTBB.

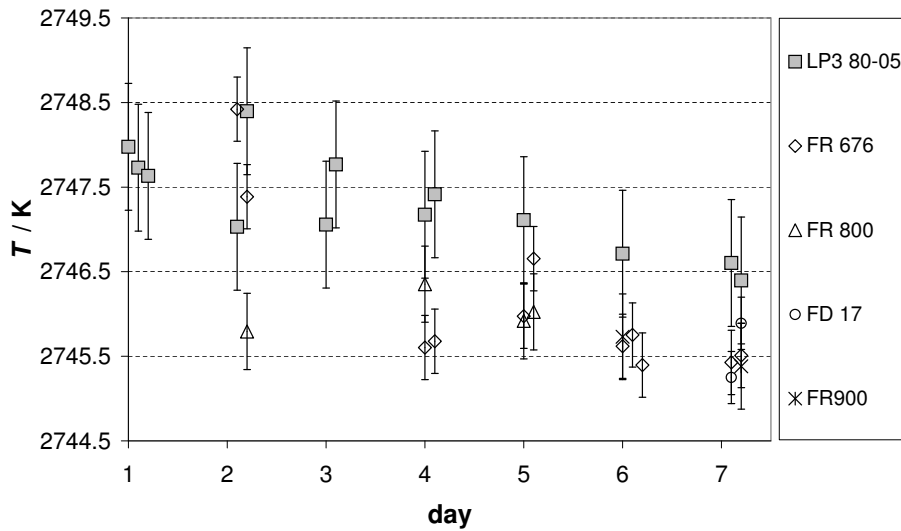
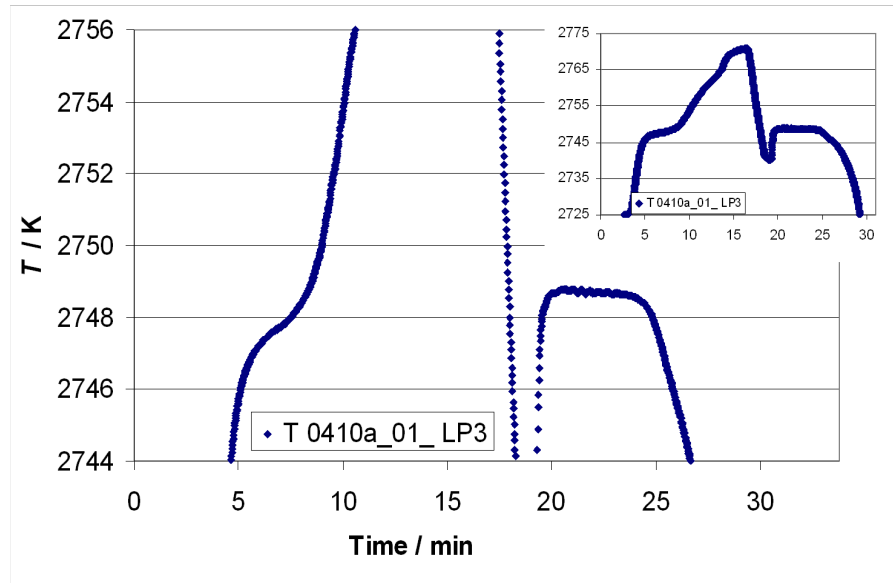
After heating the HTBB, the furnace was stabilized at a temperature approx. 25 K below the melting temperature of the eutectic material. The melting process was initiated by a step-like current increase of approx. 40 A after which the furnace was stabilized at a temperature of about 25 K above the melting temperature. For the freezing of the eutectic alloy the temperature in the furnace was suddenly reduced and stabilized at a temperature of about 25 K below the freezing temperature. Altogether more than 100 melting/freezing cycles were measured. Typical melting curves are given in Figure 9.4, Figure 9.6, and Figure 9.5.

From these profiles the point of inflection was taken as the transition temperature of the cell. For the filter radiometers the obtained temperatures were additionally corrected for diffraction loss, occurring at each of the two precision apertures. The overall correction due to this effect is given in Table 9.4.

9.1.2 Results

On seven days altogether 37 melt/freeze cycles of the Re-C fixed point cell were measured with either the LP3 or one of the four radiometers.

On four days altogether 31 melt/freeze cycles of the TiC-C fixed-point cell were measured with either the LP3 or one of the four radiometers.



	Re-C	FD17	FR 676	FR 800	FR 900	LP3
No. melts/freezes		2	6	10	2	17
average		2745.55	2746.15	2745.81	2745.48	2747.40
$\pm u, k = 1$		± 0.32	± 0.39	± 0.46	± 0.51	± 0.75
Std. dev.		0.45	0.72	0.33	0.25	0.49

Figure 9.4: Typical plateaus and temperatures in Kelvin for the melting temperature of the VNIIOFI large area fixed point Re-C cells.

	FD17	FR 676	FR 800	FR 900
Re-C	0.48	0.65	0.77	0.87
TiC-C	0.55	0.75	0.89	1
ZrC-C	0.63	0.85	1.01	1.14

Table 9.4: Correction in Kelvin due to diffraction effects for the measurements at the PTB

On three days altogether 14 melt/freeze cycles of the Re-C fixed-point cell were measured with either the LP3 or a filter radiometer at 676 nm or 800 nm.

The results of each instrument are presented in Figure 9.6, 9.5 and 9.4. The standard deviation shown is an indication of the repeatability of the cells and it can be seen that in all except of three cases the standard deviation is significantly smaller than the uncertainty of the thermodynamic temperature measurement showing the good repeatability of the irradiance mode fixed-point cells. All temperatures were determined considering the emissivity for the cells to be $\varepsilon = 0.9996$.

The results presented here are the first thermodynamic temperature measurements of eutectic fixed-point cells measured by absolute radiometry using filter radiometers in the irradiance mode. The results obtained at the VNIIOFI and the PTB all agree within their combined uncertainty, indicating that the reproducibility of the large irradiance cells in different furnaces measured with different detectors is very good. Especially all measurements using the filter radiometers are in very good agreement.

The systematically higher temperatures measured with the radiation thermometers are partly attributed to additional straylight effects, originating from the stray light baffles. Instead of knife edges, these baffles have a thick land of 5 mm, at which reflections of the radiation coming from the cavity may occur. This additionally reflected light is blocked by the 3 mm aperture, therefore has less influence on the thermodynamic temperature measurements. As the 3 mm aperture is removed for the radiance measurements reflections from the straylight baffles might have an significant influence on the measurements with the LP3.

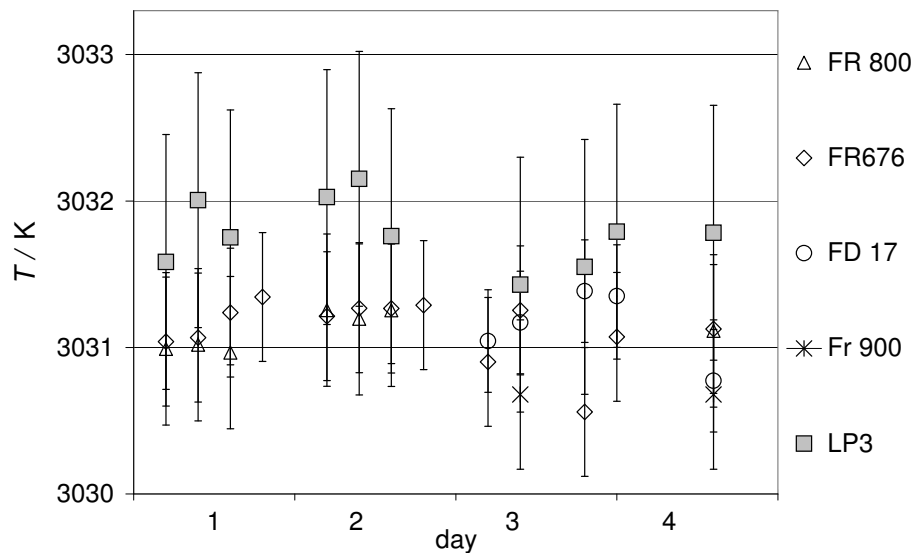
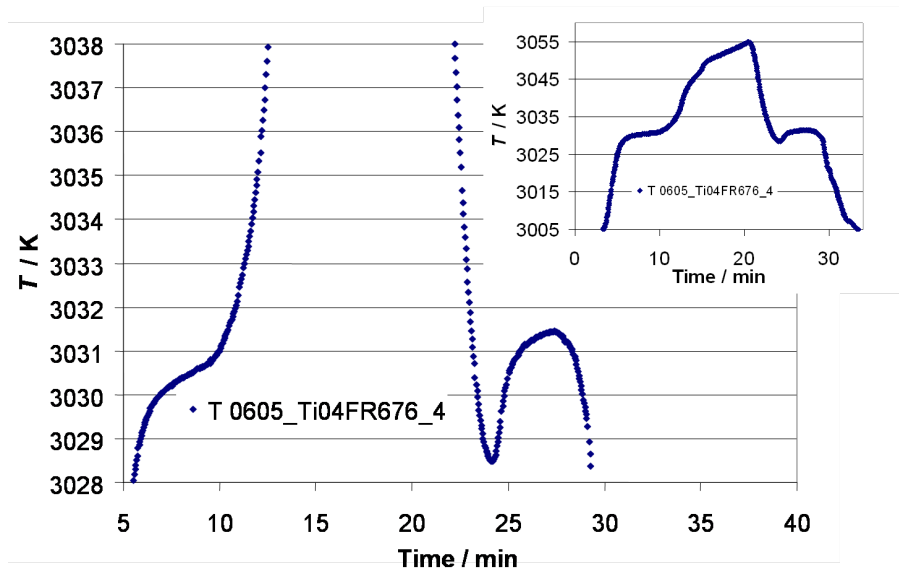
Despite the good agreement of the obtained results the measured melting temperatures are significantly lower than previously obtained temperatures using small radiance eutectic cells [Khl01a]. This may partly be explained by the large dimensions of the irradiance cells and a possible inhomogenous temperature distribution inside the HTBB. It has already been shown in literature [YB04] and section 8.1 that a non-uniform temperature distribution over the length of the eutectic fixed-point cells significantly effects the obtained melting and freezing plateau shapes. As the irradiance cells are about a factor of two longer than the radiance cells they are more sensitive to temperature inhomogeneities inside the furnace. Due to the special design of the HTBB, which requires a total reassemble in order to exchange the eutectic cells, the temperature distribution might have changed after reassembling,

although the ring configuration has not been changed. Beside the temperature inhomogeneity across the large eutectic fixed-point cells additional effects, e.g. impurity of the eutectic or geometrical effects, may also affect the measured temperatures.

9.1.3 Conclusion

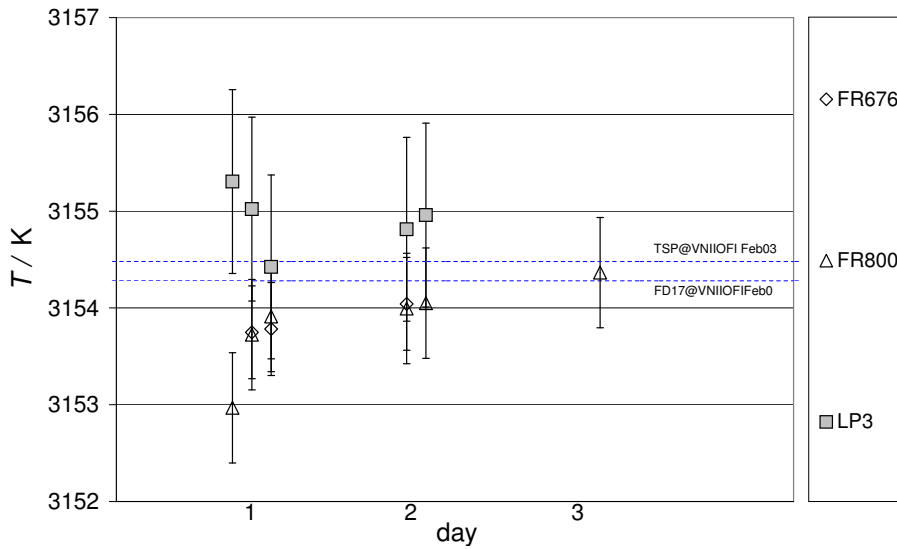
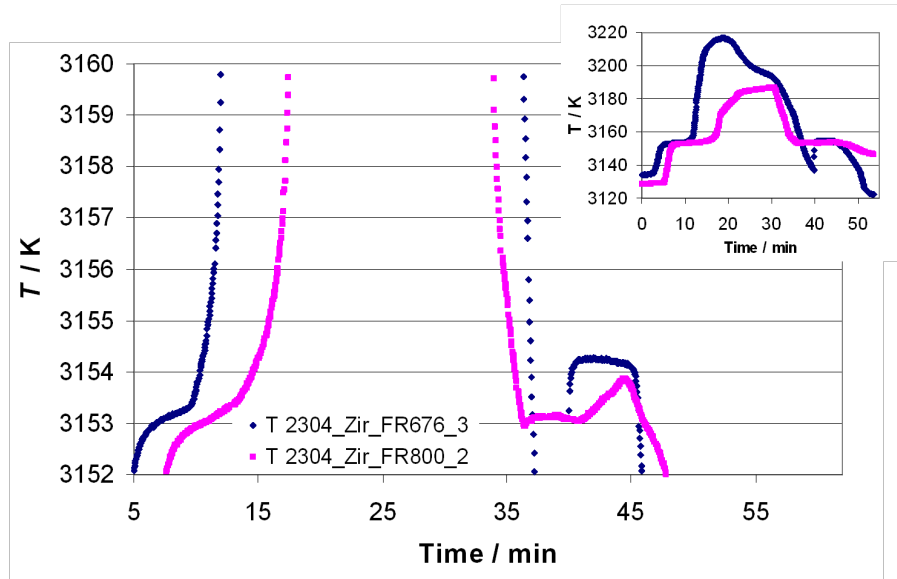
The results presented show that the temperatures of the phase transition of eutectic fixed-point materials can be obtained by absolute irradiance measurements using filter radiometers with their spectral responsivity calibrated traceable to the cryogenic radiometer. Presently the accuracy of such measurements is partly limited by the large dimensions of the inevitable larger irradiance cells setting special demands to the applied high-temperature furnaces.

These results lead to further investigations on systematic differences between small and large aperture cells in Chapter 8.3 and an investigation of the radiation field for a large aperture cell with a radiometric camera, see Chapter 10.



TiC-C	FD17	FR 676	FR 800	FR 900	LP3
No. melts/freezes	5	11	6	1	8
average	3031.22	3031.13	3031.00	3030.53	3031.78
$\pm u, k = 1$	± 0.36	± 0.45	± 0.52	± 0.58	± 0.86
Std. dev.	0.16	0.22	0.14	-	0.24

Figure 9.5: Typical plateaus, temperatures in Kelvin for the melting temperature of the VNIIOFI large area TiC-C fixed-point cells.



ZrC-C	FR 676	FR 800	LP3
No. melts/freezes	3	6	5
	3153.86	3153.78	3154.80
$\pm u, k = 1$	± 0.50	± 0.59	± 0.98
Std. dev.	0.16	0.47	0.27

Figure 9.6: Typical plateaus, temperatures in Kelvin for the melting temperature of the VNIIOFI large area ZrC-C fixed-point cells.

9.2 Thermodynamic temperature measurements of radiance cells by using an irradiance mode filter radiometer

At PTB the use of precision apertures in conjunction with absolutely calibrated filter radiometers is a well established approach for the determination of thermodynamic temperature by irradiance measurements [SFF⁺96], [Tau03]. However, an irradiance measurement involving precision apertures requires radiating cavities with a minimum aperture diameter of 8 mm, necessitating rather large fixed-point cells and the use of at least a 3 mm diameter precision aperture as it is shown in Chapter 9.1.1. With such small apertures the measurement uncertainty of the spectral irradiance is increased due to larger diffraction effects and uncertainty in the knowledge of the absolute area 9.1.3.

From the comparisons in Chapter 8.1 follows that for the determination of the fixed-point's melting temperature the temperature homogeneity across the cell is critically important. Even for the best furnace systems the temperature homogeneity is such that only cells at most 50 mm in length can be measured with lowest uncertainties. To ensure good emissivities even with such small-cell-designs the apertures of the radiating cavity of the eutectic fixed-point cells investigated here are 3 mm in diameter only. Since due to the above mentioned aperture problems such cells can only be measured in radiance mode a new radiance/irradiance comparison scheme was developed to determine the thermodynamic temperature of such small eutectic fixed-point cells.

9.2.1 Measurement principle

Two high-temperature furnace systems are used: one which holds the eutectic fixed-point cells and a second as a reference source of thermal radiation. The thermodynamic temperature T_{HTBB} of the reference source is determined by a direct spectral irradiance measurement with absolutely calibrated interference filter radiometers. The thermodynamic temperature of the eutectic fixed-point, $T_{\text{melt}}(\text{M} - \text{C})$, can be derived by comparing the spectral radiance emitted by the eutectic fixed-point at $T_{\text{melt}}(\text{M} - \text{C})$ and the reference blackbody at T_{HTBB} via a spectral radiance comparison by means of a radiation thermometer on the basis of Planck's law of blackbody radiation in ratio form:

$$\frac{\varepsilon(\text{M}-\text{C}) L_{\lambda}(\lambda, T_{\text{melt}}(\text{M}-\text{C}))}{\varepsilon(\text{HTBB}) L_{\lambda}(\lambda, T_{\text{HTBB}})} = \frac{\exp(c_2/(\lambda T_{\text{HTBB}})) - 1}{\exp(c_2/(\lambda T_{\text{melt}}(\text{M}-\text{C}))) - 1}$$

with $\varepsilon(\text{HTBB})$ and $\varepsilon(\text{M}-\text{C})$ the emissivity of the eutectic fixed-point and the reference blackbody and c_2 the second radiometric constant, respectively. An overview of the experimental set-up is given in Figure 9.7.

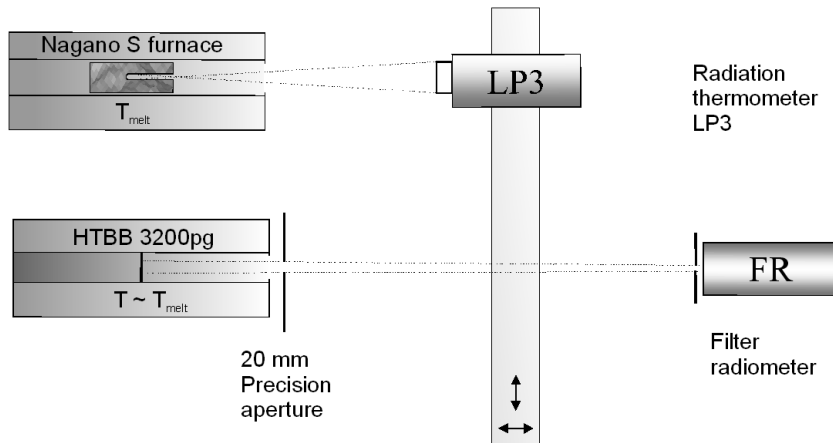


Figure 9.7: Experimental set-up for the thermodynamic temperature measurement of M-C fixed-point cells

PTB's high-temperature blackbody HTBB3200pg was used as the reference source of thermal radiation (for a detailed description see Chapter 4.1.1). The length of the radiating cavity of the HTBB is about 200 mm at a diameter of 37 mm. The eutectic cells were placed in the NMIJ Nagano S furnace described in [YSGS02] and Chapter 4.1.2.

The investigated Co-C, Pd-C, Pt-C, and Ru-C eutectic fixed-point cells were manufactured by BNM-INM/CNAM, NPL, and NMIJ. Their outer dimensions were similar: approximately 25 mm in diameter, 40-50 mm in length, and having a cavity aperture of 3 mm in diameter. The same fixed-point cells were used in the relative comparison described in Chapter 8.2 and details on differences in plateau shape and repeatability can be found there.

The nominal purities of the metals used by the different institutes were nearly the same: Pd (99.99 % , only NMIJ 99.999 %), Ru (99.95 %), Co (99.998 %) and Pt (99.999 %).

The emissivity of the cells was calculated to 0.9998 (BNM-INM), 0.99965 (NPL), 0.9996 (NMIJ).

9.2.2 Measurement scheme

For the thermodynamic temperature determination on the eutectic fixed-points an irradiance measurement with two different filter radiometers of the high temperature blackbody HTBB3200pg was followed by a radiance comparison of the eutectic fixed-point cell in the Nagano S furnace and the HTBB3200pg. The different steps are described below.

Two narrow-bandwidth interference filter radiometers with center wavelengths around 676 nm and 800 nm have been used to determine the thermodynamic temperature

of the HTBB. The spectral irradiance responsivity of these filter radiometers has been calibrated traceable to the cryogenic radiometer of the PTB , see Chapter 6.2.

The high-temperature furnace HTBB3200pg was operated at a temperature close to the melting temperature of the fixed-points under investigation. A 20 mm precision aperture in front of the HTBB defines the radiating area for measurements with the filter radiometers at a distance of about 1110 mm from this aperture. The irradiance measurement was corrected for diffraction effects at the precision apertures. Once the spectral irradiance is measured in absolute units, it is possible to determine the thermodynamic temperature of the HTBB via Planck's law of thermal radiation.

The radiometer used for the radiance comparison was an IKE LP3 radiation thermometer with an effective wavelength of around 650 nm. For the radiance measurement it was positioned 700 mm in front of the HTBB and focused onto its entrance such that both, LP3 and filter radiometer, saw a nearly equivalent area at the bottom of the HTBB's cavity. The radiation field of the HTBB is typically homogeneous better than 0.1 %, with a radial decreasing gradient towards the center. A correction for the effect of a different geometry in radiance and irradiance mode has been applied. To exclude effects of a temperature drift of the HTBB the LP3 was mounted on a moveable stage and the measurements with the filter radiometers and the LP3 were repeated alternately. For the radiance measurement at the metal-carbon eutectic melting curve the LP3 was repositioned in front of the Nagano S furnace at a distance of 700 mm from the aperture of the fixed-point cell, and aligned to the center of this aperture. For each fixed-point cell four melts and freezes were initiated with temperature steps of ± 30 K, ± 20 K, ± 10 K, ± 30 K with respect to the temperature of the point of inflection of the melting curve. The inflection point during the melt was taken as an indication of the materials melting temperature.

9.2.3 Stability measurements and SSE

The radiance and irradiance measurements of the HTBB were repeated after the M-C cell measurement with both filter radiometers and radiation thermometer to check the within-day stability of the LP3 and the reproducibility of the radiometers alignment during the radiance comparison. As the geometry of the two radiating sources differs, the measurements were corrected for size-of-source effects (SSE)[Blo99]. For assessing the SSE corrections the spectral radiance across the aperture of the HTBB and the fixed-point cells in the Nagano S furnace was scanned in horizontal direction.

This procedure was applied during 12 days for the Co-C, Pd-C, Pt-C, and Ru-C eutectic fixed-point cells constructed by NPL, LNE-INM/CNAM, and NMIJ.

	u (FR 676) / 10^{-4}	u (FR 800) / 10^{-4}
Diffraction	5	5
Distance	1	1
Aperture area	1	1
Spectral irradiance	2.1	2.3
Emissivity HTBB	3	3
u total	6	7

Table 9.5: Relative standard uncertainty components ($k=1$) for the spectral irradiance measurement of the HTBB using

9.2.4 Measurement Uncertainties

In the assignment of thermodynamic temperatures to the eutectic fixed-points both, the irradiance measurement at the HTBB and the radiance comparison via the radiation thermometer LP3, contribute to the measurement uncertainty and will be treated separately in the following. For the thermodynamic temperature determination of the HTBB uncertainty components originate from diffraction losses occurring at the two precision apertures, the measurement of the distance between the two apertures, the uncertainty of the aperture areas, the spectral irradiance calibration of the filter radiometers, and the HTBB emissivity. Table 9.5 gives the relative uncertainty components of the spectral irradiance measurement at the HTBB.

The corresponding uncertainty for a thermodynamic temperature measurement of the high temperature blackbody HTBB3200pg can be found in Table 9.6.

T_{HTBB}	Corresponding M-C fixed-point	FR 676 $u/\text{K}, k = 1$	FR 800 $u/\text{K}, k = 1$
2227 K	Ru-C	0.150	0.177
2012 K	Pt-C	0.124	0.146
1765 K	Pd-C	0.095	0.112
1597 K	Co-C	0.080	0.094

Table 9.6: Standard uncertainty in thermodynamic temperature of the HTBB with FR 676 and FR 800

For the radiance comparison between the fixed-point cell in the Nagano furnace and the HTBB additional sources of uncertainty were considered:

- The difference between the filter radiometers FR676 and FR800 as a measure for the effect of misalignment in the irradiance measurement,
- the influence of non-uniformity in the radiation field of the HTBB on the radiance/irradiance measurement, i.e. different field of view for radiation and filter radiometer,

- the within-day stability of the radiation thermometer expressed as maximum difference between the sets of HTBB measurements with the LP3 during one day, which also is a measure for the temperature stability of the HTTB,
- the size-of-source correction for the radiance measurement between Nagano and HTBB furnace,
- the emissivity of the M-C cells, a measure of the calculated differences between the cells,
- uncertainty in determining the point of inflection during the melt of the eutectic fixed-point,
- the standard deviation of four inflection point measurements, a measure for the repeatability of a single cell.

These uncertainty contributions were determined for each cell separately. A detailed overview of relative uncertainty components for the radiance measurement can be found in Table 9.8 . The total uncertainty is then determined from the uncertainty contributions of the irradiance and radiance measurement.

		R_{abs} Preampl.	Emmis.	SSE	Diffraction	Δ Irrad. HTBB profile (0.1%)
Ru-C	NMIJ	0.02	0.09	0.057	0.140	-0.233
Ru-C	NPL	0.02	0.08	0.051	0.140	-0.233
Ru-C	BNM	0.02	0.04	0.060	0.140	-0.233
Pt-C	NMIJ	-0.02	0.07	0.031	0.114	-0.190
Pt-C	NPL	-0.02	0.06	0.023	0.114	-0.190
Pt-C	BNM	-0.02	0.04	0.027	0.114	-0.190
Pd-C	NMIJ	-0.02	0.06	0.031	0.088	-0.146
Pd-C	NPL	-0.02	0.05	0.029	0.088	-0.146
Pd-C	BNM	-0.02	0.03	0.035	0.088	-0.146
Co-C	NMIJ	-0.001	0.05	0.026	0.072	-0.120
Co-C	NPL	-0.001	0.04	0.024	0.072	-0.120
Co-C	BNM	-0.001	0.02	0.028	0.072	-0.120

Table 9.7: Overview of the applied corrections to the radiance temperature, all in K

9.2.5 Results

The temperatures were obtained from Planck's law of thermal radiation in ratio form and were corrected for differences in size-of-source-effect due to the significant differences of the radiating source geometry for the HTBB and fixed-point cell in

$u, (k=1)$	Ru-C			Pt-C			Pd-C			Co-C		
	NMJ	NPL	INM	NMJ	NPL	INM	NPL	NPL	INM	NMJ	NPL	INM
u FR 676	6.7	6.7	6.7	6.8	6.8	6.8	6.8	6.8	6.8	6.9	6.9	6.9
u FR 800	7.9	7.9	7.9	8.0	8.0	8.0	8.0	8.0	8.0	8.1	8.1	8.1
ΔT FR	0.9	3.1	0.4	3.1	0.0	1.0	0.5	0.2	0.2	0.0	1.8	0.1
Inhom.Irr.HTTB	1.0	1.0	1.0	0.8	0.8	0.8	0.7	0.7	0.7	0.5	0.5	0.5
LP3 stability	2.2	2.2	2.2	2.7	2.7	2.7	3.5	3.5	3.5	4.3	4.3	0.0
SSE	1.5	1.3	1.5	1.0	0.7	0.9	1.3	1.2	1.4	1.3	1.2	1.4
Emiss. M-C cell	4.0	3.5	2.0	4.0	3.5	2.0	4.0	3.5	2.0	4.0	3.5	2.0
Infl. Point	0.4	0.5	0.8	0.4	0.5	1.1	0.9	1.4	1.8	0.3	1.3	0.4
Std. dev. 4 melts	1.0	0.6	0.7	0.3	0.7	0.6	0.3	2.5	2.2	0.5	1.2	1.0
Total	8.9	9.1	8.2	9.5	8.9	8.4	9.3	9.5	9.0	9.7	9.8	9.2

Table 9.8: Relative Uncertainty components / 1×10^{-4}

	Ru-C			Pt-C			Pd-C			Co-C		
	NMIJ	NPL	BNM									
FR	0.150	0.150	0.150	0.124	0.124	0.124	0.095	0.095	0.095	0.080	0.080	0.080
ΔT FR	0.013	0.038	0.024	0.056	0.030	0.019	0.008	0.003	0.003	0.002	0.021	0.002
Diff. correct.	0.056	0.056	0.056	0.046	0.046	0.046	0.035	0.035	0.035	0.029	0.029	0.029
LP3 stability	0.050	0.050	0.050	0.050	0.050	0.050	0.050	0.050	0.050	0.050	0.050	0.050
SSE	0.033	0.029	0.035	0.018	0.013	0.016	0.018	0.017	0.020	0.015	0.014	0.016
Emiss. M-C cell	0.090	0.078	0.045	0.073	0.064	0.037	0.056	0.049	0.028	0.046	0.040	0.023
Infl. Point	0.010	0.012	0.017	0.008	0.010	0.020	0.012	0.020	0.025	0.004	0.015	0.005
Std.dev. 3 Melt / $\sqrt{3}$	0.023	0.014	0.016	0.005	0.013	0.010	0.004	0.035	0.031	0.005	0.013	0.011
Inhom.Irr.HTTB	0.023	0.023	0.023	0.019	0.019	0.019	0.015	0.015	0.015	0.012	0.012	0.012
Std. dev. 3 Melt	0.040	0.024	0.028	0.008	0.022	0.018	0.007	0.060	0.054	0.009	0.023	0.019
Total, u / K, k=1	0.200	0.195	0.183	0.171	0.162	0.152	0.130	0.145	0.137	0.111	0.117	0.110

Table 9.9: Uncertainty components / K, k=1

		T / K	U / K
			k=2
Ru-C	NMIJ	2227.44	0.4
Ru-C	NPL	2227.22	0.39
Ru-C	BNM	2226.96	0.37
Pt-C	NMIJ	2011.88	0.33
Pt-C	NPL	2011.74	0.32
Pt-C	BNM	2011.74	0.3
Pd-C	NMIJ	1765.19	0.26
Pd-C	NPL	1765.07	0.27
Pd-C	BNM	1765	0.26
Co-C	NMIJ	1597.3	0.23
Co-C	NPL	1597.16	0.22
Co-C	BNM	1597.23	0.21

Table 9.10: Thermodynamic melting temperatures of Co-C, Pd-C, Pt-C, Ru-C manufactured by NPL, BNM-INM and NMJ

the Nagano furnace. Other correction that were considered are due to differences in emissivity between the cells, diffraction at the furnace aperture for the irradiance measurement, a non-uniform radiation profile across the aperture of the HTBB and for the photo-current measurement of the filter radiometer differences in the various feed-back resistors to the nominal gain value. An overview of the temperature values of these corrections is given in 9.7.

The resulting melting temperatures for Co-C, Pd-C, Pt-C, and Ru-C are given in Table 9.10.

9.2.6 Temperature differences between cells of one material

The results of the thermodynamic temperature measurements of the 12 eutectic fixed-point cells can be compared with the previous studies on differences in radiance temperature and with a previous thermodynamic temperature determination for a subset of the fixed-point cells [MAH⁺05]. The critical part in the comparison of the same material fixed-points measured on separate days is the day-to-day reproducibility of the simultaneous radiance and irradiance measurement of the HTBB with the radiation thermometer and the filter radiometer. Great care was taken during the experiments to ensure the pyrolytic graphite ring system of the HTBB was consistently aligned every day. It is therefore interesting to compare the results to a previous study in which the same set of fixed-point cells were investigated with regard to differences in radiance melting temperature at the same day, and that

		Radiometr. temperature meas.	Relative comparison
		ΔT to $T_{\text{average}} / \text{K}$	ΔT to $T_{\text{average}} / \text{K}$
Ru-C	NMIJ	0.231	0.167
Ru-C	NPL	0.012	0.017
Ru-C	BNM	-0.243	-0.183
Pt-C	NMIJ	0.094	0.067
Pt-C	NPL	-0.046	-0.033
Pt-C	BNM	-0.048	-0.033
Pd-C	NMIJ	0.102	0.197
Pd-C	NPL	-0.014	-0.063
Pd-C	BNM	-0.088	-0.133
Co-C	NMIJ	0.072	0.05
Co-C	NPL	-0.072	0
Co-C	BNM	0	-0.05

Table 9.11: Comparison of relative differences to an material average melting temperature measured in the two experiments described in this report

excludes the day-to-day reproducibility of the set-up. These measurements are described in Chapter 8.2 and were performed under identical thermal conditions with the Nagano S furnace used here and one additional Nagano M furnace. From the results in Table 9.10 the difference to a materials average temperature can be calculated and compared to the results of the relative radiance comparison. For each cell differences to an average temperature are shown for both experimental set-ups in Table 9.11 and Figure 9.8.

Within the combined uncertainties the earlier results are confirmed by the work presented here. The largest temperature differences between cells are seen for Pd-C and Ru-C, the two eutectic materials with the lowest metal purities available for cell production. The cells produced by the NMIJ always showed the highest melting temperatures, a result that led to further studies on the different methods used for cell filling [LY06]. Keeping in mind the complexity of the thermodynamic temperature determination and the considerable time delay between the measurements compared to the study on radiance temperature differences this is a remarkable result, which shows the applicability of the presented technique. As the measurements were performed over a period of several weeks it additionally shows the long- and mid-term stability and reproducibility of the set-up and measurement scheme.

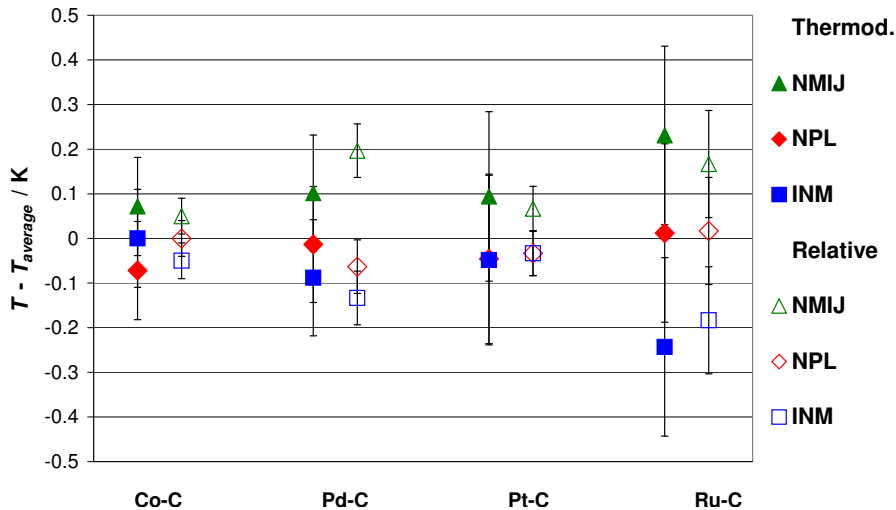
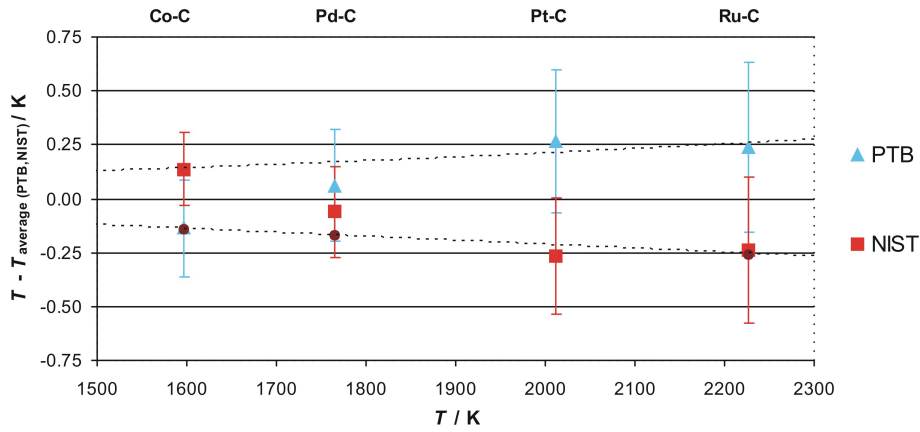


Figure 9.8: Comparison of the relative differences to an material average melting temperature as measured by the relative comparison and from the determination of thermodynamic temperatures.

9.2.7 Thermodynamic temperature scale comparison

Nine months prior to the measurements described here the NPL fixed-point cells thermodynamic melting temperatures were determined at NIST using a Thermo-Gauge furnace and an absolutely calibrated radiation thermometer [MAH⁺05]. Figure 9.9 displays the thermodynamic temperatures for the measurement sets at PTB and NIST, the difference between them and the combined expanded uncertainty. The agreement between these data and the measurement presented here is better than 500 mK over the whole temperature range. For Ru-C and Pd-C the agreement is within the combined extended uncertainty ($k=2$), for Pt-C and Co-C the temperature difference of 0.46 K and 0.32 K, respectively, only slightly exceeds the combined extended uncertainty by 0.04 K.

It has to be noted, that even for the same fixed-point cells, such a comparison with reported temperatures alone does not include a treatment of effects which are due to the differences in temperature homogeneity of the furnaces used at PTB and NIST. Additionally, the stability of fixed-point cells itself over the period of nine months between the two measurements is presumed here, an analysis of changes in the fixed-point behaviour was not taken into account. However, the extremely good agreement is a strong indicator of the stability of the cells and the negligible influence of the other effects.



	PTB		NIST		PTB – NIST	Combined <i>U</i>
NPL cell	<i>T</i> /K	<i>U</i> (<i>k</i> =2)/K	<i>T</i> /K	<i>U</i> (<i>k</i> =2)/K	ΔT /K	<i>U</i> (<i>k</i> =2)/K
Ru-C	2227.22	0.39	2226.74	0.34	0.48	0.52
Pt-C	2011.74	0.32	2011.21	0.27	0.53	0.42
Pd-C	1765.07	0.27	1764.95	0.21	0.12	0.34
Co-C	1597.16	0.22	1597.43	0.17	-0.27	0.28

Figure 9.9: Thermodynamic melting temperatures of the NPL cells determined by this work at PTB and NIST[MAH⁺05]. The figure shows the difference to the averaged melting temperature of both measurements and the combined measurement uncertainty ($k = 2$)

10 Investigation of the radiance distribution along the fixed-point aperture using a radiometric camera system

In the last chapter unexpected differences were observed between measurements in the radiance and irradiance mode at the same large area fixed-point cell. These are manifested in slight changes of the melting curve for the large aperture cells of Pt-C and Re-C, most prominent at the melts run-off. Such a "deformation" of the melting curve can lead to a different fixed-point temperature, which is determined via the curve's inflection point. Radiance and irradiance mode measurements differ in the area seen by the radiation thermometer or filter radiometer. While for the radiation thermometer LP3 focused in a distance of 700 mm to the aperture the target size at the bottom of the cavity is around 1.5 mm in diameter, the filter radiometer in a typical set-up with a 3 mm furnace aperture sees an area of around 5.5 mm in diameter of the cavity bottom. Ideally during the melting and freezing of the fixed-point material the cavity is held at a uniform temperature along its cavity walls, thus filter radiometer and radiation thermometer should measure the same temperature. If however, the temperature distribution is non-uniform along the furnace axis or across the aperture this will be sensed by different plateau shapes in the radiance and irradiance mode measurement. Numerical simulation have shown that the temperature distribution at the cavity bottom is non-uniform and significantly dependent on the surrounding [JL07]. However, up to now no experimental investigation of this phenomenon has been performed. Yet, it is difficult to measure such a difference, for on the one hand the temperature distribution is changing dynamically with the progressing phase transformation and this excludes e.g. a scan with the measurement spot of a radiation thermometer. On the other hand filter radiometer and radiation thermometer can not measure the same object simultaneously, as both have to be aligned centric to the fixed-point axis, and furnace settings are often subject to drift, especially furnaces used to hold large area fixed-point cells. [Woo04] concluded from a simplified scan of only three measurement points an improved radiation uniformity across the aperture of a large aperture Re-C cell. A solution was found in applying a radiometric camera system *TechnoTeam LMK 98-3* [KS04, tec08].

Designed to this problem and calibrated to measure luminance in photometric ap-

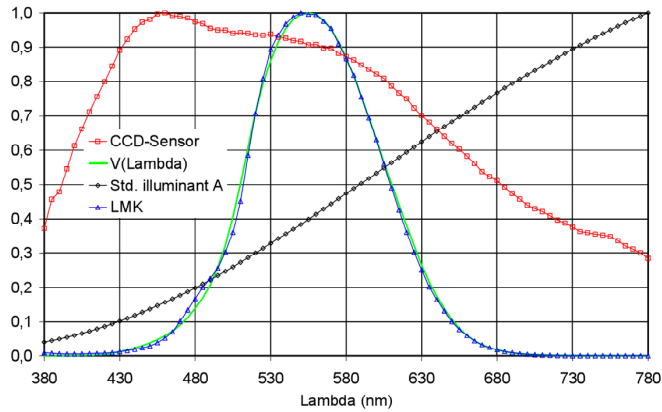


Figure 10.1: $V(\lambda)$ Adaption of the luminance camera system [tec08]

plications it features a set of optical filters to match the photopic function $V(\lambda)$. In this photometer a Si CCD chip with resolution of 1380×1080 pixel converts the incident radiant flux into signal charges according to the CCDs spectral sensitivity. For a photometric measurement, the spectral sensitivity of the overall system must match the $V(\lambda)$ curve. In order to ensure this, filters - which together with the spectral sensitivity of the respective CCD-matrix and the spectral transmission of the lens - provide the sensitivity of the human eye in comply with a standard, namely $V(\lambda)$, see Figure 10.1.

The camera can be used with and without the photometric filters. The camera is radiometrically characterized for non-linearity of the CCD and imaging errors of the optical components by the manufacturer [Kru06]. Luminance can be measured over a wide dynamic range of up to 140 dB. However, with the installed broadband filters the camera system has not been calibrated to measure radiation temperatures directly. However for a measurement of relative radiance differences, i.e. temperature differences, it can be used directly with or without filters installed. By changing the integration time and by using neutral density filters the high signal levels of a high temperature source can be adjusted to match the cameras sensitivity.

An example of how a camera system can be used to analyse the melt and freeze of eutectic fixed-points is shown in Figure 10.2. A small aperture Pt-C fixed-point cell is installed in the Nagano M furnace and during the phase transformation the photometric camera measures in a 5 sec. interval with a integration time of 200 ms. The varying furnace temperature distribution before, during and after the melt becomes clearly apparent. Before the melt, the fixed-point cell is in thermal equilibrium with the furnace surroundings, different radiant levels in the Figure 10.2(1) origin also from differences in emissivity of the viewed surfaces. While for the melt the furnace temperature is increased up to 20 K above the melting temperature, the fixed-point cavity remains at the melting temperature until the melting is finished,

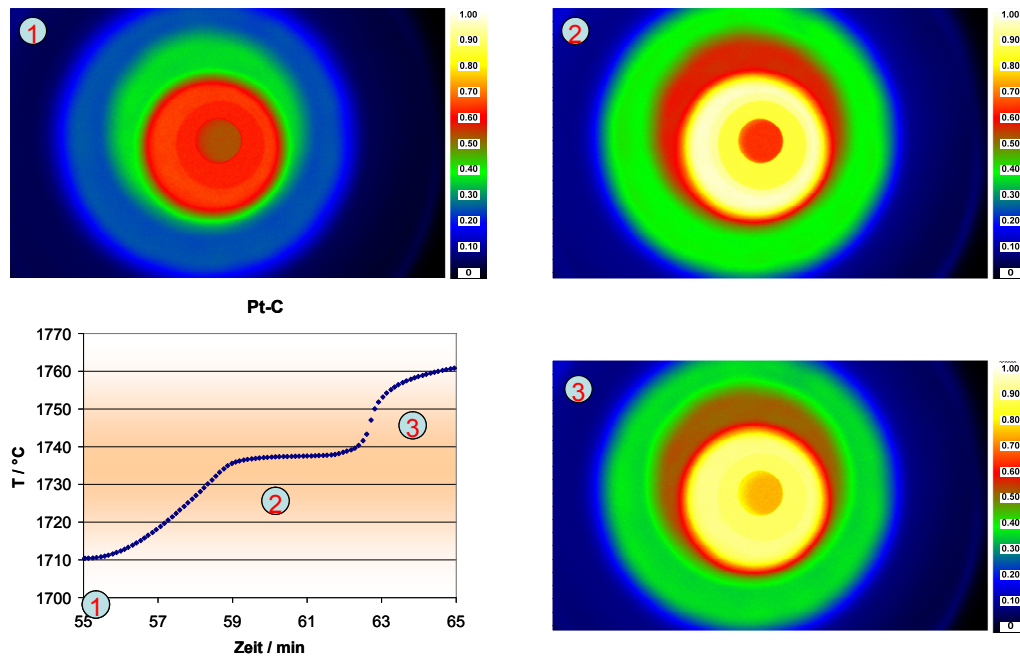


Figure 10.2: Radiance distribution inside furnace during the phase transformation of a small aperture Pt-C fixed-point cell with 3 mm opening aperture as seen by a luminance camera LMK 98-3

figure 10.2(3), and fixed-point cell and furnace surrounding are again in thermal equilibrium at a temperature 30 K above the melting temperature, thus appearing hotter.

From recorded luminance images radiance profiles across the cell diameter can be investigated. In Figure 10.3 and Figure 10.4 the radiance per pixel along a horizontal line is plotted for different stages of the melt/freeze process of 9 mm large aperture cells for Pt-C and ZrC-C. The plotted luminance signal is normalized to the centre area for each plot, as the overall level is changing with changes in the furnace temperature.

For Pt-C the luminance signal along a horizontal line across the aperture appears to be uniform within 1 %. However, for the ZrC-C cell during the melt only a center zone with a width of 1.2 mm emits a uniform luminance signal. As the melt progresses across the cell, the outer part of the cell - the cavity walls - are heating up, while the center remains colder, and the non-uniformity increases to about 3 %.

In a typical set-up the radiation thermometer LP3 has a measurement distance of about 700 mm to the aperture of the fixed-point cell, the measurement spot size of the instrument is then about 1.5 mm in diameter. When the filter radiometer is set-up in a distance of about 1100 mm to a 3 mm furnace aperture that is placed 300 mm in front of the opening of the fixed-points cavity, the filter radiometer detects an area of about 5.5 mm on the cavity bottom. The effect of the non-uniform luminance profile in Figure 10.4 can then be evaluated by integrating over the luminance of the

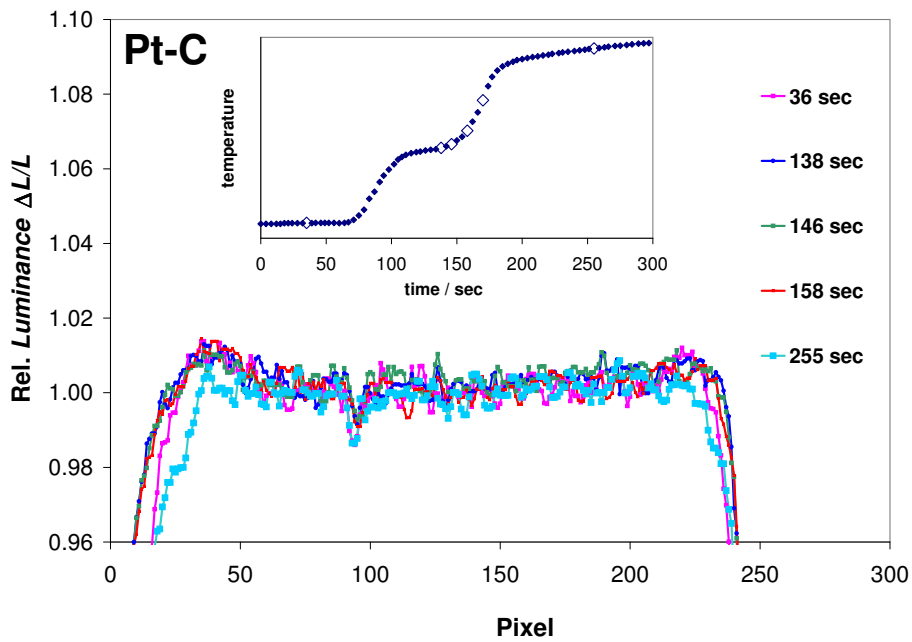


Figure 10.3: Horizontal luminance profile at different stages of the phase transformation for a large aperture Pt-C cell.

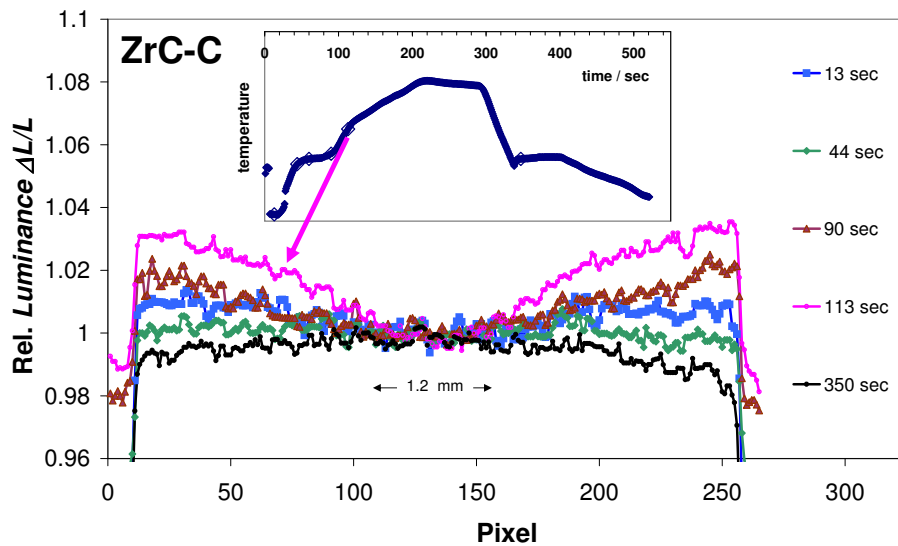


Figure 10.4: Horizontal luminance profile at different stages of the phase transformation for a large aperture ZrC-C cell.

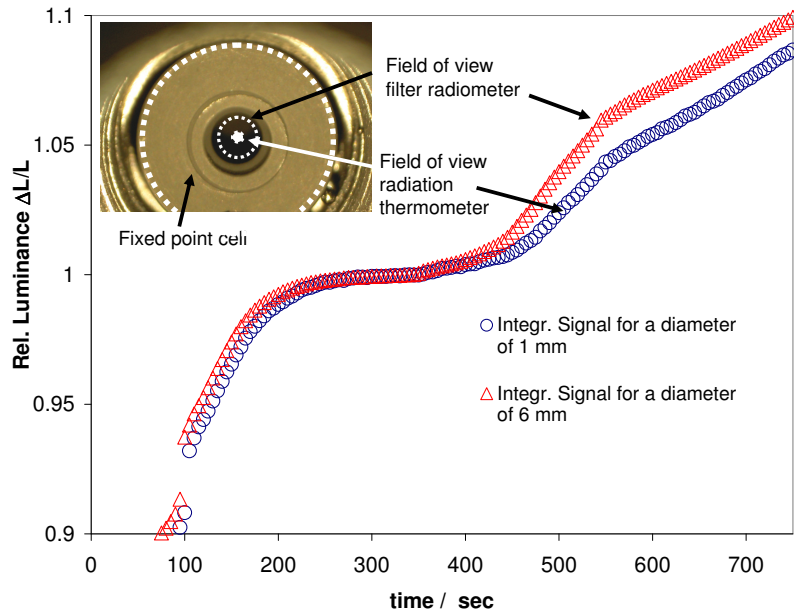


Figure 10.5: Integrated camera signal for a measurement spot size of 1 mm and 6 mm in diameter, which represents the difference in field of view for radiation thermometer and filter radiometer.

measurement areas for filter radiometer and radiation thermometer, respectively. Figure 10.5 shows such an integration for the large aperture ZrC-C cell, the result is a typical melt plateau. Differences in plateau shape become clearly visible. The increase of the signal for the 6 mm spot size is sharper at the end of melt, as was expected from the horizontal profiles. This affects the slope of the melting plateau and consequently the inflection point differs for the two data sets. For the larger measurement spot an increase of the inflection point by about 0.04 % in luminance is observed.

11 An investigation of the thermal annealing effect on the melting behaviour of Co-C and Fe-C using differential scanning calorimetry

Differential scanning calorimetry (DSC) is a technique for thermal analysis, and is widely used for studying endo- or exothermic phenomena. In DSC the temperature difference (ΔT) between the sample and a reference material is measured while both are subjected to the same temperature regimes in an environment heated or cooled at a controlled rate. DSC also allows to obtain the heat capacity of the sample by detecting the energy input into the sample and reference.

Typically a calorimeter for DSC contains two identical containers, one for the sample material under investigation and an empty one as the reference. Both containers are connected by a low-resistance heat-flow path (e.g. a metal disc) and are enclosed in a single furnace. Heating up the two probes and measuring the temperature difference between them allows to measure enthalpy or heat capacity changes in the sample relative to the reference. Figure 11.1 shows the schematics of the set-up for a heat flux DSC. Details on the measurement technique can be found in [Sor05], [HHF03].

In this work DSC was used to investigate the effect of thermal annealing on the melting of eutectic fixed-points for Fe-C and Co-C. In [SYBO05] an annealing effect of up to 200 mK for the melting temperature of Fe-C was observed. This effect was with around 50 K less pronounced for Co-C. Such effects of annealing are connected with changes in the micro-structure of the eutectic alloy. However it remained unclear whether the changes are due to a change in heat of melting or melting temperature. For this reason the effect of annealing on melting temperature was further investigated using differential scanning calorimetry for samples of Fe-C and Co-C. Furthermore extending M-C eutectic materials to high-temperature-calorimetry aims to show the potential of these fixed-point systems for temperature traceability.

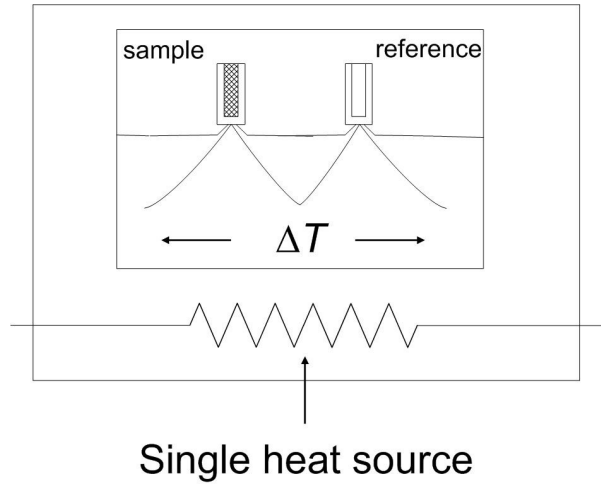


Figure 11.1: Schematics of a heat flux DSC.

Fe	-22 mesh, Puratronic, 99.998 % metals basis, Alfa Aesar, LOT Nr. 23111
C	natural, high purity, -200 mesh, 99.9999 % metals basis, Alfa Aesar, LOT 265-02-17

Table 11.1: Details on the metal and graphite used for the manufacture of the DSC sample

11.1 Manufacture of Fe-C and Co-C samples for DSC

For the experiments a commercial DSC of type Setaram MHTC96 was used, the cylindrical graphite crucibles for the samples were designed to fit into this calorimeter and had outer dimensions of 19 mm × 6.2 mm. Using the Nagano M furnace the DSC crucibles were baked and filled with the techniques described in Chapter 5 to prevent contamination of the pure materials during sample manufacture. Table 11.1 lists the used materials for the two samples.

These samples were then investigated at a PTB DSC facility. A typical measurement scheme is displayed in Figure 11.2. The sample is heated at a fast rate of 10 K/min to a temperature around 20 K above the melting temperature (I in the diagram) , the melt is observed (II) and then for solidification held at a temperature around 3 K below the freezing temperature for 150 min (IV). The temperature is then reduced to $T_{melt} - 40$ K (VI) and the sample was molten from starting from this temperature with a rate of 1 K/min (VII) and successively held for a fast freezing cooled to $T_{melt} - 40$ K and held there for 150 min (X) and another melt with a heat rate of 1K/min was realized (XI).

The results are shown in Table 11.2 for Fe-C and Table 11.3 for Co-C. For Fe-C a difference in the melting temperature of about 0.4 K was observed for the

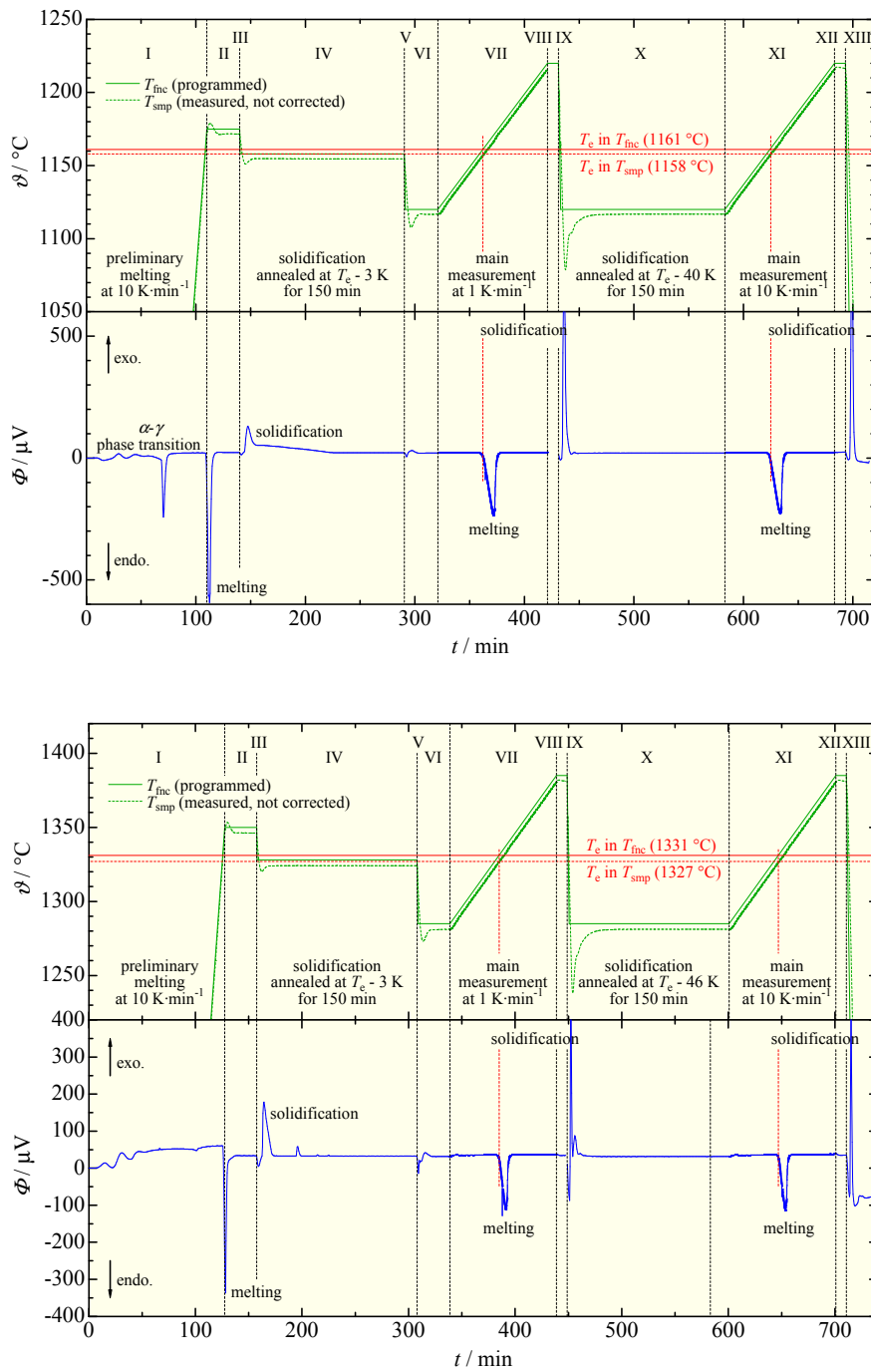


Figure 11.2: Experimental scheme of the DSC experiments showing DSC furnace temperature θ and measurement signal Φ for samples of Fe-C (above) and Co-C (below). In order to investigate the influence of thermal history on the melting temperature the samples were frozen with furnace temperatures of around 3 K and 45 K below the melting temperature.

Fe-C	Average Onset Temperature for of 6 melts / °C
Annealed at $T_{melt} - 3$ K	1157.05
Std. Dev.	0.08
Annealed at $T_{melt} - 40$ K	1156.63
Std. Dev.	0.07

Table 11.2: Effect of annealing for Fe-C at different temperatures below the melting temperature on the onset temperature during the melt.

Co-C	Average Onset Temperature for 6 melts / °C
Annealed at $T_{melt} - 3$ K	1327.04
Std. Dev.	0.2
Annealed at $T_{melt} - 46$ K	1326.8
Std. Dev.	0.18

Table 11.3: Effect of annealing for Co-C at different temperatures below the melting temperature on the onset temperature during the melt.

two annealing conditions, while for Co-C the observed influence on the melting temperature was with 0.2 K smaller. This result confirms earlier measurements by radiation thermometry.

Yet, the Fe-C samples show a better reproducibility while in the measurements of the Co-C sample a constant temperature drift can be detected. It remains unclear whether this drift stems from an unstable thermocouple in the DSC apparatus at the higher temperature or is caused by an ongoing impurity intake of the Co-C sample with each melt.

12 Impact of metal-carbon fixed-points for thermometry, radiometry and photometry

12.1 Radiation thermometry

With stable and reproducible high-temperature fixed-points the realization and dissemination of a temperature scale can be significantly simplified. The current routine for realizing the temperature scale above 1084 °C is based on a relative spectral characterization of a radiation thermometer and successive calibration at one fixed-point of either Ag, Au or Cu and in this extrapolation scheme the measurement uncertainty increases toward higher temperatures. Here, the accurate spectral characterisation of bandpass and out-of-band transmission of the radiation thermometer introduce routinely the largest sources of uncertainty [Fis02].

One single fixed-point at a higher temperature would reduce the calibration uncertainty only around the fixed-point temperature, the overall ITS-90 uncertainty would yet not be improved. With three or more fixed-points, it is no longer necessary to measure the spectral responsivity of the radiation thermometer at all, instead a multi-point fit equation with a physical model for the radiation thermometer can be used for calibration. However, in such a case the measurement uncertainty increases rapidly outside the range of fixed-point temperatures. As a compromise a scheme that employs only two fixed-points has been proposed [BYSH02], in which the exact shape of the spectral responsivity does not need to be known. An estimate for the shape of the spectral responsivity is sufficient, and for calibration the assumed integral of the spectral responsivity is iterated using the respective blackbody spectra to match the measured signal at the two fixed-points.

The resulting uncertainties for the different calibration schemes are elaborated in [SBW05], Figure 12.1 summarizes these findings. Best and normal accuracy in this diagram refers to the accuracy of the experimental set-up, fixed-points and radiation thermometers. The total uncertainty for the two fixed-point scheme $n = 2$ (Au 1337.33 K and TiC-C 3034 K) is lower than for all the other schemes, significantly so compared to ITS-90 with one fixed-point, $n = 1$, Au. For three fixed-points, $n = 3$, no determination of spectral responsivity is needed, but compared to the other schemes, the uncertainty does increase drastically for temperature above and below the fixed-point temperatures used for calibration.

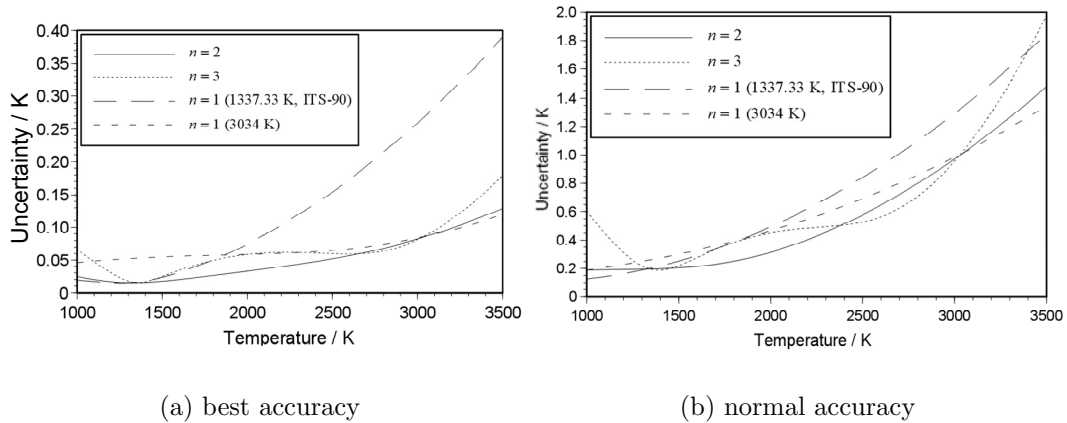


Figure 12.1: Comparison of total uncertainties for different schemes with $n=1, 2$ or 3 fixed-points for best and normal uncertainty [SBW05]

Therefore, and with regard to the variety of eutectic metal-carbon fixed-points available in the temperature range between 1300 K and 3500 K, a simpler and more accurate realisation compared to the ITS-90 can be provided with the thermodynamic temperature measurements of the eutectic materials investigated in this work, as the fixed-point temperature is now set at low uncertainty. For the described two fixed-point scheme, which can be realised in a variety of subranges using different M-C fixed-points, the measurement uncertainty is no longer relying on absolute wavelength determination.

12.2 Radiometry and photometry

Yet, the envisaged impact of metal-carbon fixed-points is even wider as they can be utilized to check stability and calibration not only for radiation thermometers, but also for photometers and radiometers. With the stable phase transition temperature and designed as a blackbody-cavity-cell the radiant properties during the phase transformation are that of a reproducible planckian radiator. Metal-carbon fixed-points can be used in addition or even to replace conventional transfer standards with similar radiant output and temperature range as tungsten strip lamps for radiance and FEL-type lamps for irradiance measurements. Both lamp types are connected with restriction to the user.

A tungsten strip lamp requires a careful alignment of the measurement instrument to a small measurement spot often only 0.8 mm wide and 0.8 mm tall which allows only instruments with small field-of-view to be used. Radiation emitted from the tungsten strip and transmitted by the quartz window is highly polarized and dependent on the location on the tungsten strip, the angle of emission and on the wavelength. In a FEL lamp a coiled-coil of the tungsten wire increases the emittance. Yet, the

coiled structure for an FEL lamp and also the tungsten ribbon is changing with the lamps on-off-cycles due to alteration in the tungsten micro-structure. Consequently, frequent re-calibration of such lamps is necessary [FH99].

In addition to that, such lamps suffer from poor mechanical and calibration stability when they are used as transfer standards and sent around between different laboratories. The instability often limits the uncertainty in international comparisons for checking the agreement of the realisation of radiometric and photometric units between national metrology institutes [HTH⁺06, BIP08, WFC⁺06].

In contrast, as M(C)-C eutectics prove to be stable, reproducible and robust, their emitted radiation is not polarized and the emission characteristic is that of an ideal lambertian source and the emissivity is wavelength independent. The irradiance output of some high temperature fixed-points is compared to that of FEL and Deuterium lamps for typical set-ups in Figure 12.2.

This figure illustrates the requirements of high-temperature fixed-points for radiometry.

- A high temperature is required, preferably higher than 2500 °C, this can be realized with M(C)-C eutectic fixed-points.
- For an irradiance measurement the fixed-point-cell must have a large aperture. This can be realized as is shown by the large aperture cells in this work.
- For spectral calibrations, the plateau duration must be long enough for a wavelength scan at a monochromator based set-up.

The required aperture size of 9 mm in diameter and larger, makes the overall cell dimension relatively too large for current furnace systems. Developments are therefore on the way to improve the temperature uniformity, overall size and temperature range of commercial high temperature furnaces [AKS⁺06, KOS⁺07, KOS⁺05b, KOS⁺05a, CBRM08].

As a result of this work, a re-definition of the SI unit for luminous intensity, the candela by a fixed-point blackbody seems possible. Originally, in 1948 the first definition of the *candela*, for the realisation for luminous intensity, was based on the freezing and melting temperature of Platinum by using a planckian radiator similar to the fixed-point cells used with this work, defined as [Ter68]

... candela is the luminous intensity, in the perpendicular direction, of a surface of 1/600 000 square meter of a black body at the temperature of freezing platinum under a pressure of 101 325 newtons per square meter.

However, due to instabilities and contamination of the platinum metal with the crucible material a new definition was introduced in 1979 by the CIPM [Gia80]:

The candela is the luminous intensity, in a given direction, of a source that emits monochromatic radiation of frequency 540 x 10¹² Hertz and that has a radiant intensity in that direction of 1/683 Watt per steradian.

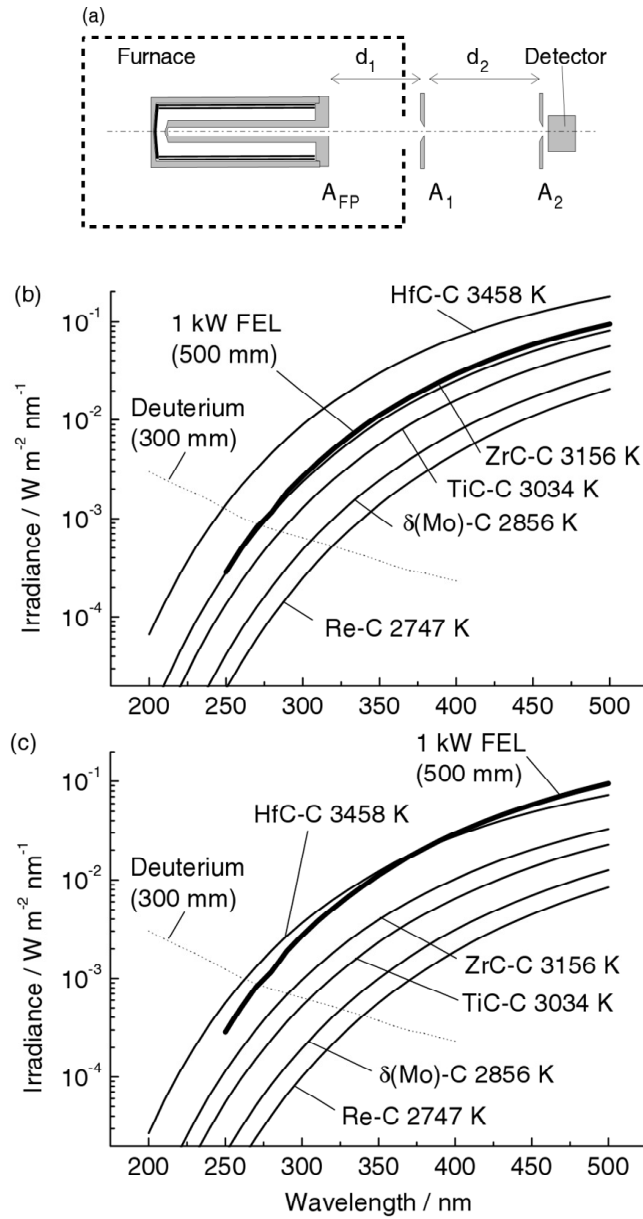


Figure 12.2: Estimated spectral irradiance obtained in the A_2 plane in comparison with lamps. (The distances for the FEL lamp and the deuterium lamp are 500 mm and 300 mm, respectively.) (a) Configuration of the irradiance measurement. (b) $A_{FP} = \varnothing 13 \text{ mm}$, $A_1 = \varnothing 8 \text{ mm}$, $A_2 = \varnothing 5 \text{ mm}$, $d_1 = 200 \text{ mm}$, $d_2 = 500 \text{ mm}$. (c) $A_{FP} = \varnothing 9 \text{ mm}$, $A_1 = \varnothing 5 \text{ mm}$, $A_2 = \varnothing 5 \text{ mm}$, $d_1 = 200 \text{ mm}$, $d_2 = 500 \text{ mm}$. [YKW⁺06]

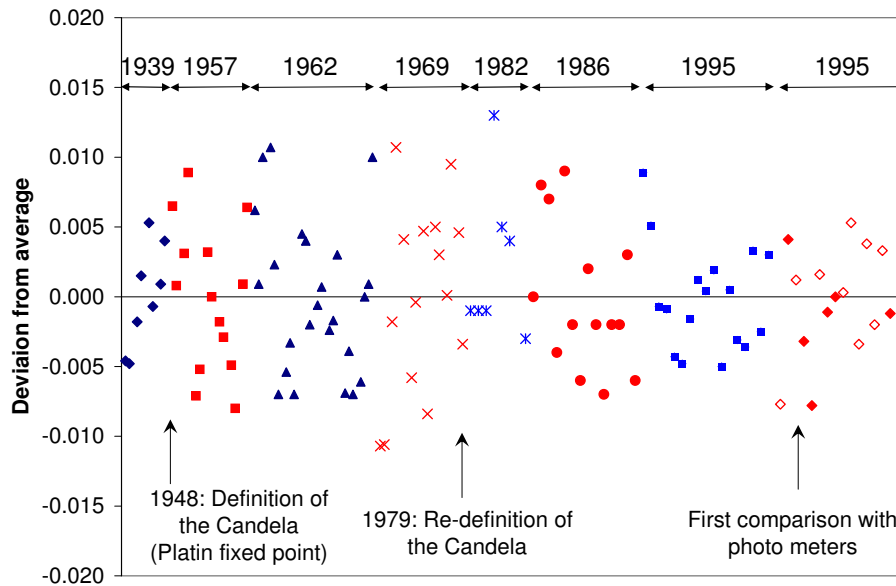


Figure 12.3: Results of international comparisons of the Candela between 1939 and 1995 [Stoht]

Yet, even with the new definition the uncertainty in the realization of the candela did not improve significantly as can be seen when graphing the reported measurement values of various international comparisons of the candela in Figure 12.3 [Stoht]. In this figure the reported values scatter by about 1 %.

For a practical realization of the candela, fixed-points can be re-utilized, because M-C eutectic fixed-points offer an improved mechanical and thermal stability over the conventional Pt-fixed-point. Their higher temperature results in significantly higher spectral radiance and consequently lower calibration uncertainty. A measurement uncertainty of 0.5 K at 3156 K (ZrC-C) relates to a measurement in spectral radiance at 555 nm of 0.1 %. This indicates a straight-forward improvement for the realization of the candela by an order of magnitude.

12.3 Contact thermometry

In industrial processes the temperatures above 1000 °C are often measured using thermocouples. These sensors make use of the thermoelectric or *Seebeck* effect, i.e. in metals a voltage is generated when the metal is subjected to a thermal gradient. To measure this voltage another conductor has to be connected to the hotter end. The thermoelement is normally realized as two wires with one end at the hot spot, the other at a fixed reference temperature. In order to measure the voltage, the second wire is of dissimilar metal and connected at the hot end. Different types of thermocouples are categorized by the metallic composition of the wires, which are for Type S, R and B thermocouples made from Platinum and Platinum/Rhodium

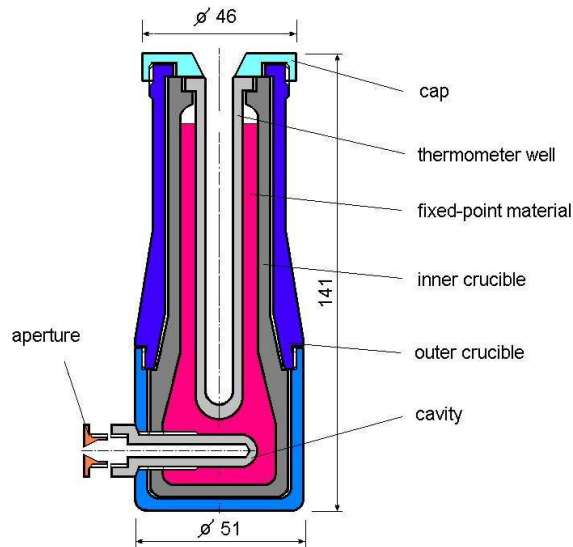


Figure 12.4: Schematic diagram of a fixed-point cell design for the simultaneous measurement of radiation thermometer and thermocouple [EH07]

alloy of varying composition for one of the wires.

Thermocouples can be calibrated against references which have in turn be calibrated using fixed-points. Direct calibration against a secondary fixed-point as Palladium or Platinum is hindered by non-stability of this fixed-points and the high melting temperature of these two materials, which is often too close to the melting temperature of the thermocouple wires. Above the copper point a wire bridge method can be used for calibration of type R and S thermocouples using Palladium (1554 °C) as secondary reference point. This method is destructive and consists of breaking the thermocouple hot junction and welding a Pd wire between the thermoelements. This assembly is subsequently heated in a furnace with a slow heating rate and the thermovoltage (emf) is monitored. At the Pd melting temperature the voltage signal drops and the last data point is used as reference for calibration. For any measurement the thermoelements have to be reconnected subsequently. The achievable uncertainty with this method are even on a NMI level in the order of around 1.5 K at 1500 °C. Dissemination of the temperature scale to the user then increases the uncertainty up to several 10 K.

Pt/Pd thermocouples cannot be calibrated directly at any fixed-point above the copper point. Fixed-points based on M-C eutectics promise to improve the calibration of high-temperature thermocouples and to provide a means for characterizing their properties [FMM03]. The fixed-point temperatures of Fe-C , Ni-C, Co-C and Pd-C are below the melting of Palladium and offer convenient calibration points for temperatures up to nearly 1500 °C. Beyond that temperature W-Re thermocouples can be used up to 2300 °C, and these also can only be calibrated by using eutectic M-C or M(C)-C fixed-points. The design of the eutectic cells for thermocouple measurement are similar to those for radiation thermometry, with the cavity replaced

by a thermometer well and their outer dimensions somewhat larger. However, additional issues must be considered when measuring eutectic phase transitions with thermocouples as the immersion depth of the thermocouple within the well is important and special sheath materials had to be found to avoid a chemical reaction of the thermocouple with graphite crucible [MEP⁺08].

A special fixed-point design has been developed at PTB to simultaneously measure a M-C fixed-point cell with radiation thermometer and thermocouple for a calibration traceable to the ITS-90 of the thermocouple [EKT04, EH07]. Figure 12.4 shows a schematic diagram of this fixed-point design, which features a vertical thermometer well for the calibration of a thermocouple and a horizontal cavity for measurements with a radiation thermometer.

In an industrial environment the measurement uncertainty for temperatures of around 1300 °C promises to be reduced by 1 - 2 K using Co-C fixed-points [PMSF08].

13 Summary

The International Temperature Scale of 1990 (ITS-90) principally limits the temperature measurement accuracy above the freezing temperature of copper (1084 °C) due to the lack of long-term stable high-temperature fixed points. Fixed-points made from metal-carbon eutectics in a graphite crucible offer a solution, as their phase transition temperature can be as high as 3000 °C and they would allow to use an interpolation function for temperature measurements between the fixed-points temperatures. The work presented investigates the potential of metal-carbon (M-C) eutectic materials as high-temperature fixed points comprehensively and develops measuring techniques to determine their stability, reproducibility and thermodynamic phase transition temperature with lowest uncertainties using absolute radiometric methods.

Essential prerequisite was the understanding and optimisation of the three relevant elements: the M-C eutectic fixed-point cells, the furnaces used and the applied radiometric methods and devices.

For the measurement of eutectic fixed point cells with lowest uncertainties two different types of radiation detection systems at different operating wavelengths were used and had to be optimized: a radiation thermometer LP3 with an effective wavelength around 650 nm and Silicon photodiode based filter radiometers with effective wavelengths around 476 nm, 676 nm, 800 nm and 900 nm. Using the well established spectral responsivity scale developed and maintained at PTB the spectral responsivity of the Silicon photodiode based filter radiometers at 676 nm, 800 nm and 900 nm was calibrated with an uncertainty as low as $2.5 \cdot 10^{-4}$. The main improvement in this area was the construction and implementation of a silicon photodiode based filter radiometer at 476 nm. The calibration of a filter radiometer at 476 nm wavelength required the improvement of the stray-light suppression of the spectral comparator in the short wavelength range in order to obtain lowest uncertainties. Applying the mentioned absolutely calibrated filter radiometers now allows world leading thermodynamic temperature measurements with uncertainties as low as 130 mK at temperatures of 3000 °C. For radiance measurements the radiation thermometer LP3 was advanced for the application at temperatures above 1084 °C. It appeared at the beginning, that the original optical design of this instrument caused a small but significant drift of several 100 mK when measuring a temperature at 2500 °C. A solution to this drawback was found in a new filter design, separating the glass filter from the interference filter, which prevents the interference layers from being heated up. The dependence of the instruments signal from the area surround-

ing the radiating spot, the so-called Size-of-Source-Effect, SSE, is one of the main sources of uncertainty in precision radiation thermometry. To accurately measure the crucial influence on the signal of the LP3 a SSE measurement facility has been improved fundamentally within this work. The SSE was measured for the radiation thermometer LP3 using a direct and indirect method and compared with results obtained using a setup at the National Physical Laboratory/ NPL (UK).

With these significant improvements the LP3 could be used as transfer instrument to show the high level of agreement between the different realizations of the ITS-90 at three National Metrology Institutes (NMI), the PTB, the NPL (UK) and the National Measurement Institute of Japan (AIST/NMIJ) in the high temperature range between 1000 °C and 2800 °C. For the comparison with the NPL a maximum difference of 0.64 K was observed at 2750 °C with a standard measurement uncertainty ($k=1$) of 1.04 K. For the comparison with the NMIJ an agreement within 0.4 K was achieved within the whole temperature range with a measurement uncertainty of 1.1 K ($k=1$).

The radiation thermometer was then applied to optimize the high temperature furnaces for the application of M-C eutectics. This required the measurement and optimisation of the temperature distribution inside the cavity and design improvements of the radiating cavity. Two special high-temperature furnaces were optimized and then applied to measure M-C fixed-point cells. For that purpose special methods have been developed to measure the temperature distribution along the radiating cavity. The result of these optimisation was a cavity with a temperature inhomogeneity of less than 5 K at 2500 °C over the length of the fixed-point-cell. Besides in radiation thermometry, high temperature fixed-points are of great interest also for radiometry. Yet, the fixed-point cavity for radiometric sources is often required to have a larger radiating aperture compared to radiation thermometry and with radiometric applications often in the UV spectral range the fixed-point temperature should exceed 2500 °C.

An important factor that influences the filling process, the mechanical stability and the radiating properties of the fixed-point cell as well as the requirements for the furnace is the fixed-point design. With two principally different cell designs, fixed-point cells for Cu, Pt-C and Re-C were constructed using the same high-purity material. One cell type with a 3 mm aperture is optimized for a radiance mode measurement, the other cell type has an 8 mm large aperture for an irradiance mode measurement. In different comparisons the smaller-aperture cells always showed a better repeatability and a smaller melting range, hence this cell design allows to determine the fixed-point temperature with lower uncertainties. In a next step small aperture fixed-point cells of Co-C, Pd-C, Pt-C, Ru-C and Re-C of different origin were investigated with respect to the fixed-points stability and reproducibility in order to point out the best filling technique and fixed-point material. The reproducibility of the material combinations above manufactured by different laboratories was better than ± 200 mK, and in case of Co-C, Pt-C and Re-C it was better than ± 100 mK. The repeatability of all cells and all investigated material combinations was in every case

better than ± 50 mK. The fundamental result of these investigations was the identification of Co-C, Pt-C and Re-C as the best suited fixed-points for implementation in an improved high-temperature scale.

The stability and reproducibility results are a major step for the implementation of the M-C eutectic fixed-points in a new temperature scale. However, the final and most important point is the determination of the thermodynamic temperature of the phase transition with lowest uncertainties. For this, a measurement scheme had to be developed that combines the good performance of the small aperture fixed-point cells with the small measurement uncertainty of the radiometric temperature measurement using filter radiometers. The measurement scheme realizes this, based on a radiance comparison between two blackbody cavities, by using a radiation thermometer LP3. Using this scheme, the melting temperature was determined exemplarily for Co-C, Pd-C, Pt-C and Ru-C with standard uncertainties below 200 mK. These results were confirmed by a recent, independent measurement of the thermodynamic temperature at the NIST and the NPL.

The thermodynamic temperature of fixed-point cells designed for radiometric application with a large aperture was measured for the first time for Re-C, TiC-C and ZrC-C with radiometric methods and with standard uncertainties below 500 mK for temperatures up to 2880 °C.

The presented work has proven that metal-carbon eutectic fixed-points are the most promising candidates to be included in a revised, new International Temperature Scale (ITS-201X) towards an improved and facilitated temperature measurement above the highest fixed-point of the ITS-90, the freezing temperature of copper (1084.6 °C). A temperature measurement exceeding this temperature is now no longer connected with inevitable large measurement uncertainties due to the extrapolation of the temperature scale towards higher temperatures. The results of the present work open for the first time the possibility of an interpolation function for fixed-points between 1100 °C and 2500 °C reducing the measurement uncertainties of the new improved temperature scale significantly.

Bibliography

- [AKS⁺06] K. Anhalt, B. Khlevnoy, M. K. Sakharov, M. Burdakin, S. A. Ogarev, V. I. Sapritsky, Y. Yamada, and P. Sperfeld. New high-temperature furnaces for metal (carbide)–carbon eutectic fixed points. In Physikalisch Technische Bundesanstalt, editor, *Proceedings of Temperatur 2006: Verfahren und Geräte in der Temperatur- und Feuchtemessung*, pages 277–284, 2006.
- [BB71] G. Bauer and K. Bischoff. Evaluation of the emissivity of a cavity source by reflection measurements. *Applied Optics*, (10 (12)):2639–2643, 1971.
- [BBMP90] R. E. Bedford, G. Bonnier, H. Maas, and F. Pavese. *Techniques for approximating the International Temperature Scale of 1990*. Bureau International des Poids et Mesures, Sèvres, 1990.
- [BBMP96] R. E. Bedford, G. Bonnier, H. Maas, and F. Pavese. Recommended values of temperature on the International Temperature Scale of 1990 for a selected set of secondary reference points. *Metrologia*, 33(2):133–154, 1996.
- [BIP08] BIPM. Key comparison database, 2008.
- [Ble70] W.R. Blevin. A precise measurement of the Stefan-Boltzmann constant. *Metrologia*, pages 15–29, 1970.
- [Blo99] P. Bloembergen. On the correction for the size-of-source effect corrupted by background radiation. *TEMPMEKO Proceedings*, pages 607–612, 1999.
- [Blo07] P. Bloembergen. Temperature drop xxxxxx. *TEMPMEKO Proceedings*, page XL, 2007.
- [BM74] R.E. Bedford and C.K. Ma. Emissivities of diffuse cavities: Isothermal and nonisothermal cones and cylinders. *Journal of the Optical Society of America*, (64 (3)):339–349, 1974.
- [Bro66] S.C. Brown. *Introduction to electrical Discharges in gases*. John Wiley & Sons Inc, New York, 1966.
- [Bro97] C.E. Brookley. Blackbody type heating element for calibration furnace with pyrolytic graphite coating disposed on end cap electrode members. Technical Report 5608838, United States Patent 5608838, 1997.

- [BY06] P. Bloembergen and Y. Yamada. SIE and OME as tools to estimate the uncertainty in the correction for the effect of impurities applied to metal-carbon eutectic systems. *Metrologia*, 43(5):371–382, 2006.
- [BYSH02] P. Bloembergen, Y. Yamada, F. Sakuma, and J. Hartmann. Realizing the high-temperature part of a future ITS with the aid of eutectic metal-carbon fixed-points. In D. C. Ripple, editor, *Temperature: aip conference proceedings*, pages 291–296, 2002.
- [CA78] L. Crovini and A. Actis. Noise thermometry in the range 630 °C- 962 °C. *Metrologia*, (14):69–78, 1978.
- [Cal99] H. L. Callendar. On a practical thermometric standard. *Phil. Mag.*, 48:519–547, 1899.
- [Car03] A.C. Carter. Improved broad band blackbody calibrations at NIST for low-background infrared applications. *Metrologia*, (40):S1 – S4, 2003.
- [CBRM08] Khaled Chahine, Mark Ballico, John Reizes, and Jafar Madadnia. Optimization of a graphite tube blackbody heater for a thermogage furnace. *International Journal of Thermophysics*, 2008.
- [Cha64] B. Chalmers. *Principles of solidification*. Wiley series on the science and technology of materials. Wiley, New York, NY, 1964.
- [CMA94] B. Chu, H.C. McEvoy, and J.W. Andrews. The NPL reference sources of blackbody radiation. *Measurement Science Technology*, (5):12–19, 1994.
- [Cou94] National Research Council, editor. *Solar influences on global change*. National Academy Press, Washington D.C., 1994.
- [Del01] Pierre Delhaès. *Graphite and precursors*, volume 1 of *World of carbon*. Gordon and Breach, Amsterdam u.a, 2001.
- [EH07] F. Edler and J. Hartmann. Simultaneous contact and non-contact measurements of the melting temperature of a Ni-C fixed-point cell. *International Journal of Thermophysics*, 28(6):2002–2008, 2007.
- [EKT04] F. Edler, M. Kuhne, and E. Tegeler. Noise temperature measurements for the determination of the thermodynamic temperature of the melting point of palladium. *Metrologia*, 41(1):47–55, 2004.
- [Ell83] R. Elliott. *Eutectic Solidification Processing: Crystalline and glassy alloys*. Butterworths monographs in materials. Butterworth, London, 1983.
- [ES89] R.E. Edsinger and J.F. Schooley. Differences between thermodynamic temperature and $t_{\text{ITS}-68}$ in the range 230 °C to 660 °C. *Metrologia*, (26):95–106, 1989.
- [Eul60] J. Euler. *Arbeitsmethoden der optischen Pyrometrie*. Braun, Karlsruhe, 1960.

- [Fel03] B. Fellmuth. Comments on the underestimation of the change of fixed-point temperatures by impurities due to a non-justified application of Raoult's law. (CCT/03-12), 2003.
- [FFBS05] J. Fischer, B. Fellmuth, W. Buck, and J. Seidel. Towards a new definition of the kelvin: ways to go. In D. Zvizdic, editor, *9th International Symposium on Temperature and Thermal Measurements in Industry and Science: Cavtat – Dubrovnik, 22 – 25 June 2004*, 2005.
- [FFS96] R. Friedrich, J. Fischer, and M. Stock. Accurate calibration of filter radiometers against a cryogenic radiometer using a trap detector. *Metrologia*, (32):509–513, 1995 / 96.
- [FH99] J. Fischer and J. Hartmann. Calibration of tungsten strip lamps as transfer standards for temperature. In M. de Groot and J. Dubbeldam, editors, *Proceedings of Tempmeko 99*, pages 561–566. IMEKO, 1999.
- [FH06] B. Fellmuth and K. D. Hill. Estimating the influence of impurities on the freezing point of tin. *Metrologia*, 43(1):71–83, 2006.
- [Fis02] J. Fischer. Uncertainty budgets for realization of ITS-90 by radiation thermometry. In D. C. Ripple, editor, *Temperature: AIP conference proceedings*, pages 631–638, 2002.
- [Fle66] J. C. Flemming. An evaluation of an high temperature blackbody as a working standard of spectral radiance. *Applied Optics*, (5):195–200, 1966.
- [FMM03] G. Fourrez, R. Morice, and G. Machin. HIMERT: Industrial calibration of type S, B and C thermocouples by comparison to metal-carbon eutectic cells: interest and perspectives. *Proc. 11th Int. Metrology Conf. Metrologie 03, Toulon, France*, 2003.
- [FNST01] J. Fischer, G. Neuer, E. Schreiber, and R. Thomas. Metrological characterisation of a new transfer standard radiation thermometer. In B. Fellmuth, J. Seidel, and G. Scholz, editors, *Proc. of Tempmeko 2001*, pages 801–806. VDE Verlag, 2001.
- [Fox95] N.P. Fox. Radiometry with cryogenic radiometers and semiconductor photodiodes. *Metrologia*, (32):535–543, 1995.
- [FTM96] N. P. Prior T.R. Fox, E. Theocharous, and S. N. Mekhontsev. Solid-state detectors for infrared radiometry. *Metrologia*, (32):609–613, 1995/96.
- [Fu93] L. Fu. Characterization of photodiodes in the uv and visible spectral region based on cryogenic radiometry. *Metrologia*, (30):297–303, 1993.
- [Gia80] P. Giacomo. News from the BIPM. *Metrologia*, 16(1):55–61, 1980.
- [HAH⁺03] J. Hartmann, K. Anhalt, J. Hollandt, E. Schreiber, and Y. Yamada. Improved thermal stability of the linear pyrometer LP3 for high temper-

- ature measurements within the EU–Project HIMERT. In VDI, editor, *Temperatur 2003: VDI Berichte*, pages 135–141. VDI, 2003.
- [Har02] J. Hartmann, 2002.
- [HHF03] Günther Walther Heinrich Höhne, Wolfgang Hemminger, and Hans-Jürgen Flammersheim. *Differential scanning calorimetry: With 19 tables*. Springer, Berlin, 2., revised and enl. ed edition, 2003.
- [HM77] Henning and Moser. *Temperaturmessung*. Johann Ambrosius Barth, Leipzig, 1977.
- [HT02] J. Hartmann and D. R. Taubert. Assessing blackbody emissivity by monte carlo simulation. *Proc. of the Int. Conference of Infrared Sensors and Systems, Erfurt, Germany*, pages 133–138, 2002.
- [HTH⁺06] J. Hartmann, R. Thomas, K.D. Hill, A.G. Steele, and C.K. Ma. Bilateral comparison of the NRC and PTB local realizations of the ITS–90 between the silver point and 1700 °C using vacuum tungsten strip lamps as transfer standards. *Metrologia*, 43(1A):03003–03003, 2006.
- [JL07] P. Jimeno Largo. *Novel high–temperature metal–carbon eutectic fixed points: Influence of impurities and of the temperature distribution at the radiant cavity: PhD thesis*. PhD thesis, Universidad de Valladolid, Valladolid, Spain, February 2007.
- [JLBY⁺04] P. Jimeno-Largo, P. Bloembergen, Y. Yamada, M. Villamanan, and G. Machin. Numerical analysis of the temperature drop across the cavity bottom of high temperature fixed points for radiation thermometry. *Proceedings of TEMPMEKO*, pages 335–340, 2004.
- [Jon79] T.P. Jones. The suitability of Tungsten strip lamps as secondary standard sources below 1064 °C. *Metrologia*, (15):135–141, 1979.
- [JT76] T. P. Jones and J. Tapping. Freezing–point of platinum. *Metrologia*, 12(1):19–26, 1976.
- [Jun86] H. J. Jung. A measurement of thermodynamic temperatures between 683 K and 933 K by an infrared pyrometer. *Metrologia*, (23):19–31, 1986.
- [JV73] H. J. Jung and J. Verch. Ein Rechenverfahren zur Auswertung pyrometrischer Messungen. *Optik*, (38):95–109, 1973.
- [KF98] W. Kurz and D. J. Fisher. *Fundamentals of solidification*. Trans Tech Publications, Uetikon–Zürich, 4. rev. ed edition, 1998.
- [KGG99] Y. G. Kim, K. S. Gam, and K. H. Kang. Realization of the palladium freezing point for thermocouple calibrations. *Metrologia*, 36(5):465–472, 1999.
- [KGG00] Y. G. Kim, K. S. Gam, and K. H. Kang. Fabrication of a nickel freezing–point cell and preliminary study of its behaviour. *Metrologia*, 37(3):243–245, 2000.

- [Khl01a] B. B. Khlevnoi. Methods of measuring the thermodynamic temperature of a high-temperature blackbody. *Meas. Tech.*, 44(3):308–314, 2001.
- [Khl01b] B. B. Khlevnoy. Use of high-temperature phase transitions of eutectics for precision reproduction of radiometric quantities in the visible and ultraviolet regions. *Meas. Tech.*, 44(5):461–466, 2001.
- [Kir60] G. Kirchhoff. Ueber das Verhältniß zwischen dem Emissionsvermögen und dem Absorptionsvermögen der Körper für Wärme und Licht. *Annalen der Physik*, 109:275–301, 1860.
- [KK75] H. Kunz and H. J. Kaufmann. Photoelectric direct current standard pyrometers and their calibration at ptb: Inst. phys. conf. ser., 1975.
- [KOS⁺05a] B. Khlevnoy, S. A. Ogarev, V. I. Sapritsky, K. Anhalt, and Y. Yamada. Furnace for high-temperature metal (carbide)-carbon eutectic fixed-point. In Gröbner, editor, *Proc. of Newrad 2005*, pages 277–278, 2005.
- [KOS⁺05b] B. B. Khlevnoy, S. A. Ogarev, V. I. Sapritskii, S. P. Morozova, M. L. Samoilov, M. K. Sakharov, V. B. Khromchenko, and V. I. Shapoval. Reference blackbody sources in the 100–3500 K range for precision measurements in radiometry, photometry, and optical thermometry. *Meas. Tech.*, 48(11):1083–1089, 2005.
- [KOS⁺07] B. B. Khlevnoy, S. A. Ogarev, V. I. Sapritsky, K. Anhalt, Y. Yamada, and M. K. Sakharov. Investigation of furnace uniformity and its effect on high-temperature fixed point performance. *International Journal of Thermophysics*, page submitted, 2007.
- [Kru06] Udo Krueger. Bestimmung ausgewählter Parameter und Kennwerte digitaler Kamerasysteme. *Photonik*, (2):66–69, 2006.
- [KS04] Udo Krüger and Franz Schmidt. *Ausgewählte Aspekte der ortsaufgelösten Erfassung stationärer Licht- und Farbverteilungen*, volume 6 of *Publikationsreihe des Fachgebiets Lichttechnik in Ilmenau*. Der Andere Verl., Osnabrück, 2004.
- [KSO⁺05] B. Khlevnoy, V. I. Sapritskii, S. A. Ogarev, M. K. Sakharov, M. L. Samoylov, and Y. A. Pikalev. Development of fixed points above 2700 K based on M-C and MC-C eutectics at VNIIOFI for radiation thermometry and radiometry. In D. Zvizdic, editor, *9th International Symposium on Temperature and Thermal Measurements in Industry and Science: Cavtat – Dubrovnik, 22 – 25 June 2004*, pages 203–208, 2005.
- [KSO⁺08] B. Khlevnoy, M. Sakharov, S. Ogarev, V. Sapritsky, Y. Yamada, and K. Anhalt. Investigation of furnace uniformity and its effect on high-temperature fixed-point performance. *International Journal of Thermophysics*, 29(1):271–284, 2008.
- [LE00] O. Lummer and Pringsheim E. Über die Strahlung des schwarzen

Körpers für lange Wellen. *Verhandlung der Deutschen Physikalischen Gesellschaft*, (2):163–180, 1900.

- [Lie76] Fritz Lieneweg. *Handbuch Technische Temperaturmessung*. Vieweg, Braunschweig, 1976.
- [LLK67] B. Lersmacher, H. Lydtin, and W. F. Knippenberg. Zur Technologie der pyrolytischen Graphit-Herstellung. *Chemie Ingenieur Technik CIT*, 39(14):833–842, 1967.
- [LM04] D. Lowe and G. Machin. High-temperature fixed-points at the National Physical Laboratory. *SICE 2004 Annual Conference*, pages 802–806, 2004.
- [LY06] D. Lowe and Y. Yamada. Reproducible metal-carbon eutectic fixed-points. *Metrologia*, 43(2):S135–S139, 2006.
- [Mac99] G. Machin. The NPL high temperature calibration facility (1200 K to 3100 K). In *9th Congress International de Metrologie*, pages 556–559, 1999.
- [MAH⁺05] G. Machin, K. Anhalt, J. Hartmann, D. Lowe, N. Sasajima, and Y. Yamada. A comparison of high temperature fixed-points of Pt-C and Re-C constructed by BIPM, NMIJ and NPL. In D. Zvizdic, editor, *9th International Symposium on Temperature and Thermal Measurements in Industry and Science: Cavtat – Dubrovnik, 22 – 25 June 2004*, 2005.
- [MEP⁺08] R. Morice, F. Edler, J. Pearce, G. Machin, J. Fischer, and J. Filtz. High-temperature fixed-point facilities for improved thermocouple calibration—euromet project 857. *International Journal of Thermophysics*, 2008.
- [MI99] G. Machin and M. Ibrahim. Size of source effect and temperature uncertainty: I-high temperature systems. *TEMPMEKO Proceedings*, pages 681–686, 1999.
- [MMB] G. Machin, H. McEvoy, and S.J. Boyes. A realisation of their Pd point at NPL. In Piero Marcarino, editor, *Proc. of Tempmeko 96*, pages 301–303. Levrotto & Bella.
- [Mod03] Michael F. Modest. *Radiative heat transfer*. Academic Press, Amsterdam, 2. ed. edition, 2003.
- [Mol99] M.R. Moldover. Primary acoustic thermometry from 217 k to 303 k. *Proceedings of TEMPMEKO 1999*, pages 412–417, 1999.
- [MYL⁺] G. Machin, Y. Yamada, D. Lowe, N. Sasajima, F. Sakuma, and F. Kai. A comparison of metal-carbon eutectic blackbody cavities of rhenium, iridium, platinum and palladium between NPL and NMIJ. In *Proc. Of Tempmeko2001*.

- [NFET01] G. Neuer, J. Fischer, F. Edler, and R. Thomas. Comparison of temperature measurement by noise thermometry and radiation thermometry. *Measurement*, 30(3):211–221, 2001.
- [Oka90] T. B. Massalski ; H. Okamoto, editor. *Binary Alloy Phase Diagrams*. ASM International, 1990.
- [Pal93] J. Palmer. Alternative configurations for trap detectors. *Metrologia*, 30:327–333, 1993.
- [PE04] David A. Porter and Kenneth E. Easterling. *Phase transformations in metals and alloys*. CRC Press, Boca Raton, Fla., 2. ed., repr edition, 2004.
- [Pfa78] W. G. Pfann. *Zone melting*. Krieger, Huntington NY, 1978.
- [PKLP05] C. W. Park, B. H. Kim, D.-H. Lee, and S. N. Park. Realization of a nickel carbon eutectic fixed point with an optimized filling process monitored by the melting–freezing temperature difference measurement. *Metrologia : international journal of pure and applied metrology*, pages Vol. 42, No. 1 (2005), L5–L9, 2005.
- [PMSF08] J.V. Pearce, G. Machin, S. Swardle, and T. Ford. Optimising heat treatment of gas turbine blades with a Co–c fixed point for improved in–service thermocouples. *Int. J. Thermophys.*, page to be published, 2008.
- [Pro98] A.V. Prokhorov. Monte-Carlo method in optical radiometry. *Metrologia*, (35):465–471, 1998.
- [PT90] H. Preston-Thomas. The International Temperature Scale of 1990 (ITS–90). *Metrologia*, (27):3–10, 1990.
- [PTB03a] Calibration certificate FR 676 , Ser. No. FR2/10–676, Calibration mark 2123 PTB 03. Technical report, PTB, 2003.
- [PTB03b] Calibration certificate FR 800, Ser. Nr. FR5/12–800. Technical Report 2124 PTB 03, PTB, 2003.
- [PTB03c] Calibration FR 800, Ser. Nr. FR5/12–900, Cal. mark 2125 PTB 03: Calibration certificate. Technical Report 7.21–1.4–03–3, PTB, 2003.
- [PTB05] Calibration certificate FR 476 , Calibration mark 1939 PTB 05. Technical report, PTB, 2005.
- [QF99] T. J. Quinn and C. Fröhlich. Accurate radiometers should measure the output of the sun. *Nature*, 401:841, 1999.
- [Qui91] T. J. Quinn. *Temperature*. Academic Press, London, 1991.
- [Qui97] T. J. Quinn. News from the BIPM. *Metrologia*, (34):187–194, 1997.
- [RDGM99] D. C. Ripple, D. R. Defibaugh, K. A. Gillis, and M. R. Moldover. Primary acoustic thermometer for use up to 800 k. *Proceedings of TEMP-MEKO 1999*, pages 418–423, 1999.

- [RJK⁺00] M. Richter, U. Johannsen, P. Kuschnerus, U. Kroth, H. Rabus, G. Ulm, and L. Werner. The PTB high-accuracy scale in the ultraviolet. *Metrologia*, 37:515–518, 2000.
- [Sap96] V.I. Sapritskii. Black-body radiometry. *Metrologia*, (32):411–417, 1995 / 96.
- [Sas02] N. Sasajima. Metal-carbon and metal carbide-carbon eutectic fixed points as high-temperature standard. *SICE*, (August 5–7):1431 – 1423, 2002.
- [SBF⁺05] M. Sadli, F. Bourson, M. Fanjeaux, S. Briadeau, B. Rougie, and G. Bonnier. Study of metal-carbon eutectic points: from construction to temperature determination. In D. Zvizdic, editor, *9th International Symposium on Temperature and Thermal Measurements in Industry and Science: Cavtat – Dubrovnik, 22 – 25 June 2004*, pages 611–616, 2005.
- [SBW05] P. Saunders, P. Bloembergen, and D. R. White. Uncertainty in temperature realised by radiation thermometry using two fixed points. In D. Zvizdic, editor, *9th International Symposium on Temperature and Thermal Measurements in Industry and Science: Cavtat – Dubrovnik, 22 – 25 June 2004*, pages 193–199, 2005.
- [Sch] E. Schreiber. Considerations for the realisation of the temperature scale above 2000c by means of radiation thermometry.
- [SDB72] W.H. Steele, M. De, and J.A. Bell. Diffraction corrections in radiometry. *Journal of the Optical Society of America*, (62 (9)):1099–1103, 1972.
- [SFF⁺96] M. Stock, J. Fischer, R. Friedrich, H. J. Jung, L. Werner, and B. Wende. Measurement of $T - T_{90}$ in the range from 660 °C to 962 °C by absolute spectral radiometry employing a cryogenic radiometer and a double heatpipe black body. *Proceedings of TEMPMEKO 1996, Torino*, 1996.
- [SKK⁺97] V. I. Sapritskii, B. B. Khlevnoy, V. B. Khromchenko, B. E. Lisiansky, S. N. Mekhontsev, U. A. Melenevsky, and S. P. Morozova. Precision blackbody sources for radiometric standards. *Applied Optics*, (36 (22)):5403–5408, 1997.
- [SKS⁺05] M. K. Sakharov, B. B. Khlevnoy, V. I. Sapritskii, M. L. Samoylov, and S. A. Ogarev. Development and Investigation of high-temperature fixed point based on TiC-C eutectics. In D. Zvizdic, editor, *9th International Symposium on Temperature and Thermal Measurements in Industry and Science: Cavtat – Dubrovnik, 22 – 25 June 2004*, pages 319–324, 2005.
- [SMY01] F. Sakuma, L. Ma, and Z. Yuan. Distance effect and size-of-source effect of radiation thermometers. In B. Fellmuth, J. Seidel, and G. Scholz, editors, *Proc. of Tempmeko 2001*, pages 161–166. VDE Verlag, 2001.
- [SOK⁺03] V. I. Sapritsky, S. A. Ogarev, B. B. Khlevnoy, M. L. Samoylov, and V. B. Khromchenko. Development of metal-carbon high-temperature fixed-

- point blackbodies for precision photometry and radiometry. *Metrologia*, 40(1):S128–S131, 2003.
- [Sor05] Michio Sorai, editor. *Comprehensive handbook of calorimetry and thermal analysis*. Wiley & Sons and Wiley, Chichester, engl. language ed., reprinted with corr edition, 2005.
- [Spe98] P. Sperfeld. Investigation of high-temperature blackbody BB3200. *Metrologia*, (35):419–422, 1998.
- [SSO95] H. Sakate, F. Sakuma, and A. Ono. Observation of also melting and freezing plateaus using a cavity type tungsten crucible. *Metrologia*, 32:129–131, 1995.
- [Sto95] M. Stock. *Realisierung und Vergleich von drei radiometrischen Primärnormalen im sichtbaren Spektralbereich: Kryoradiometer, Elektronenspeicherring BESSY I und Hohlraumstrahlung: Dissertation*. PhD thesis, TU Berlin, Berlin, 1995.
- [Stoth] M. Stock. Zwei Jahrzehnte Kryoradiometrie – Erfolge und Herausforderungen. Presentation at PTB Berlin - 23 May 2003, 2003, May 23th.
- [SYB03] N. Sasajima, Y. Yamada, and P. Bloembergen. Effect of gaseous impurities on the melting curve of iron-carbon eutectic fixed points. In Society of Instrument and Control Engineers, editors, *SICE 2003 annual conference: Fukui, Japan, August 4 - 6, 2003*, volume 2, pages 2191–2194. Society of Instrument and Control Engineers, 2003.
- [SYBO05] N. Sasajima, Y. Yamada, P. Bloembergen, and Y. Ono. Dependence of iron-carbon eutectic melting on pre-freezing rate and annealing conditions. In D. Zvizdic, editor, *9th International Symposium on Temperature and Thermal Measurements in Industry and Science: Cavtat - Dubrovnik, 22 - 25 June 2004*, 2005.
- [SYG+06] N. Sasajima, H. W. Yoon, C. E. Gibson, V. Khromchenko, F. Sakuma, and Y. Yamada. The NIST eutectic project: Construction of Co-C, Pt-C and Re-C fixed-point cells and their comparison with the NMIJ. *Metrologia*, 43(2):S109–S114, 2006.
- [Tau03] D. R. Taubert. *Radiometrische Messung thermodynamischer Temperaturen und Vergleich mit der Internationalen Temperaturskala (ITS-90) im Bereich von 419 °C bis 660 °C: Dissertation*. PhD thesis, TU Berlin, Berlin, 2003.
- [tec08] technoteam.de, 2008.
- [Ter68] J. Terrien. News from the International Bureau of Weights and Measures. *Metrologia*, 4(1):41–45, 1968.
- [TFH+05] D. R. Taubert, R. Friedrich, J. Hollandt, P. Sperfeld, and J. Hartmann. Long-term stability of the spectral responsivity of filter radiometers at

- the ptb. In D. Zvizdic, editor, *9th International Symposium on Temperature and Thermal Measurements in Industry and Science: Cavtat – Dubrovnik, 22 – 25 June 2004*, pages 977–983, 2005.
- [TFHH03] D. R. Taubert, R. Friedrich, J. Hartmann, and J. Hollandt. Improved calibration of the spectral responsivity of interference filter radiometers in the visible and near infrared spectral range at PTB. *Metrologia*, 40:S35–S38, 2003.
- [WFC⁺06] Emma R. Woolliams, Nigel P. Fox, Maurice G. Cox, Peter M. Harris, and Neil J. Harrison. The CCPR K1—a key comparison of spectral irradiance from 250 nm to 2500 nm: measurements, analysis and results. *Metrologia*, 43(2):S98–S104, 2006.
- [WGA⁺96] D. R. White, R. Galleano, A. Actis, H. Brixy, M. de Groot, J. Dubbeldam, A. L. Reesink, F. Edler, H. Sakurai, R. L. Shepard, and J. C. Gallop. The status of Johnson noise thermometry. *Metrologia*, (33):325–335, 1996.
- [Woe82] B. Woerner. A photoelectric direct current spectral pyrometer with linear characteristics. In J. F. Schooley, editor, *Temperature – Its Measurement and control in Science and Industry*, pages 429–432, 1982.
- [Woo04] E. R. Woolliams. *Development and evaluation of a high-temperature blackbody source for the realisation of NPL’s primary spectral irradiance scale*. PhD thesis, University of Manchester, Manchester / UK, 2004.
- [Yam01] Y. Yamada. High-temperature fixed points in the range 1150 °C to 2500 °C using metal-carbon eutectics. *Metrologia*, (38):213–219, 2001.
- [Yam05] Y. Yamada. Advances in High Temperature Standards above 1000 °C. *MAPAN Journal of Metrology Society of India*, (20 (2)):183–191, 2005.
- [YAS05] H. W. Yoon, D. W. Allen, and R. D. Saunders. Methods to reduce the size-of-source effect in radiometers. *Metrologia*, 42(2):89–96, 2005.
- [YB04] Y. Yamada and P. Bloembergen. High-temperature metal-carbon eutectic fixed-point cells with improved robustness. *SICE 2004 Annual Conference*, 2:1027–1030, 2004.
- [YBS⁺02] Y. Yamada, P. Bloembergen, N. Sasajima, S. Torizuka, N. Yoshida, and N. Yamamoto. On the effect of impurities on the melting curve of the metal-carbon eutectic systems. *SICE 2002. Proceedings of the 41st SICE Annual Conference*, 4:2441–2443, 2002.
- [YDB⁺01] Y. Yamada, Y. Duan, M. Ballico, S. N. Park, F. Sakuma, and A. Ono. {Measurement of Rh-C, Pt-C and Ru-C eutectic points by four national metrology institutes}. *Metrologia*, 38(3):203–212, 2001.
- [Yin01] C. Yinghang. A medium temperature radiation calibration facility using a new design of heatpipe blackbody as a standard source. *Measurement Science and Technology*, (12):491–494, 2001.

- [YKW⁺06] Y. Yamada, B. B. Khlevnoy, Y. F. Wang, T. J. Wang, and K. Anhalt. Application of metal (carbide)–carbon eutectic fixed points in radiometry. *Metrologia*, 43(2):S140–S144, 2006.
- [Yoo06] H. W. Yoon. The realization and the dissemination of thermodynamic temperature scales. *Metrologia*, 43(2):S22–S26, 2006.
- [YSGS02] Y. Yamada, N. Sasajima, H. Gomi, and T. Sugai. High–temperature furnace systems for realizing metal–carbon eutectic fixed points. In D. C. Ripple, editor, *Temperature: aip conference proceedings*, pages 985–990, 2002.
- [YSSO99] Y. Yamada, H. Sakate, F. Sakuma, and A. Ono. Radiometric observation of melting and freezing plateaus for a series of metal–carbon eutectic points in the range 1130 °C to 1950 °C. *Metrologia*, (36):207–209, 1999.
- [YWS06] Y. Yamada, Y. Wang, and N. Sasajima. Metal carbide–carbon peritectic systems as high–temperature fixed points in thermometry. *Metrologia*, 43(5):L23–L27, 2006.
- [Zal83] E.F. Zalewski. Silicon photodiode device with 100% external quantum efficiency. *Applied Optics*, 22:2867–2873, 1983.

A Phase diagrams and physical properties of binary metal-carbon alloys

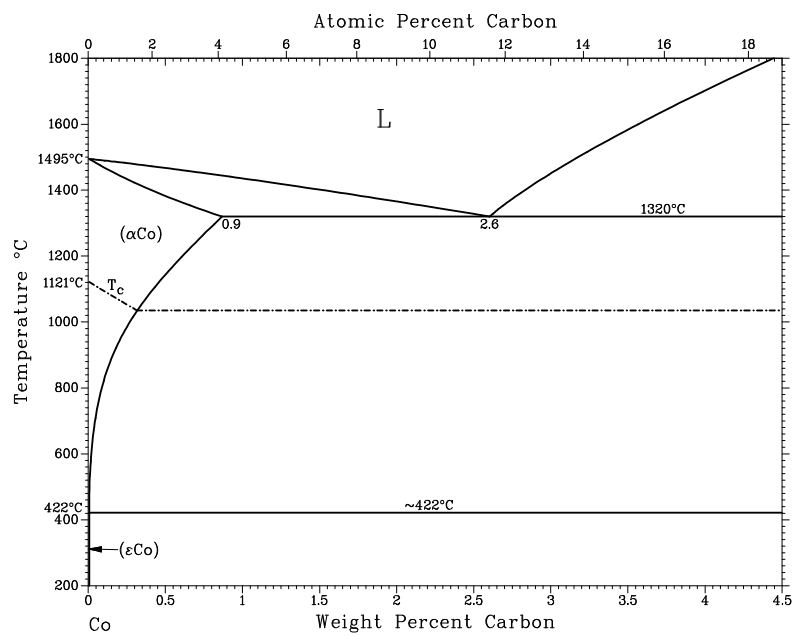


Figure A.1: Co-C [Oka90]

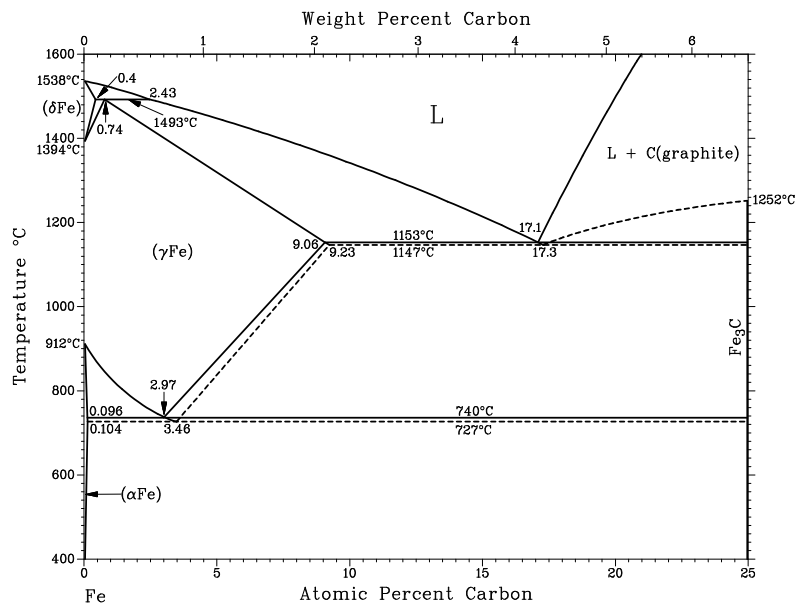


Figure A.2: Fe-C [Oka90]

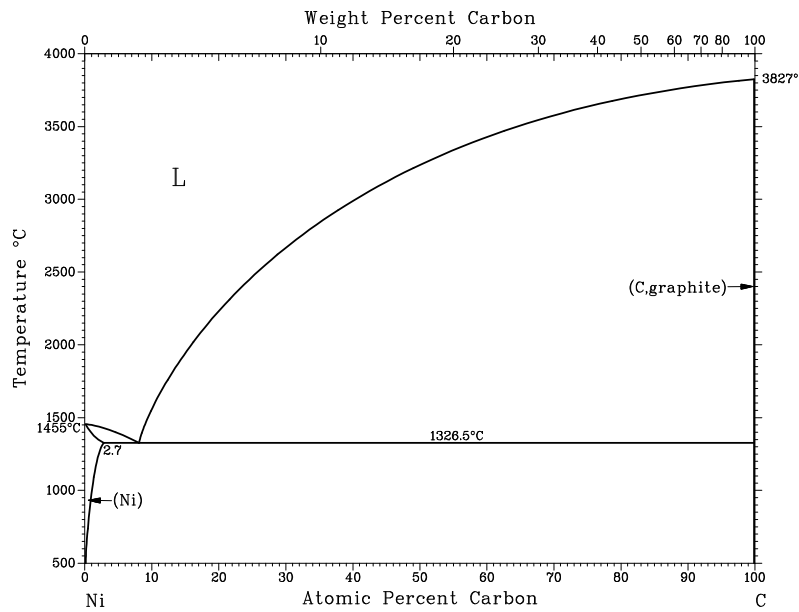


Figure A.3: Ni-C [Oka90]

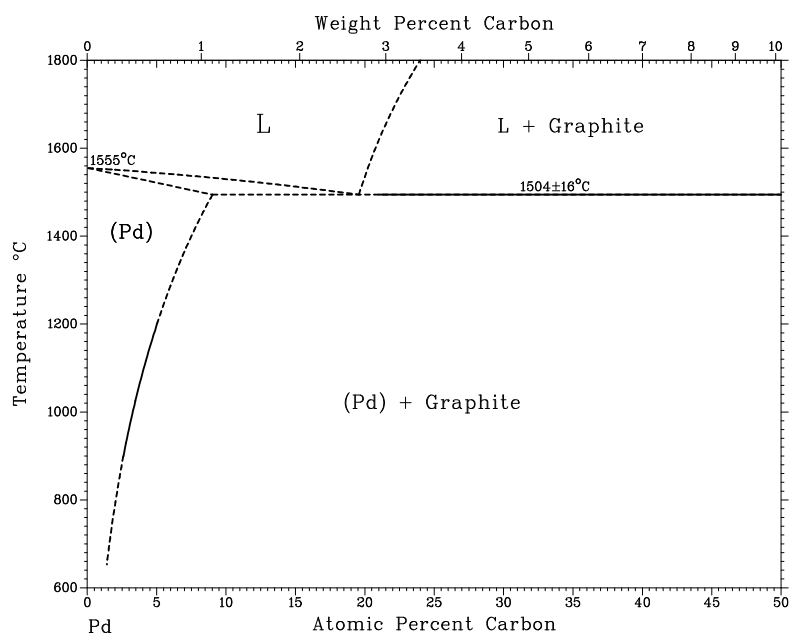


Figure A.4: Pd-C [Oka90]

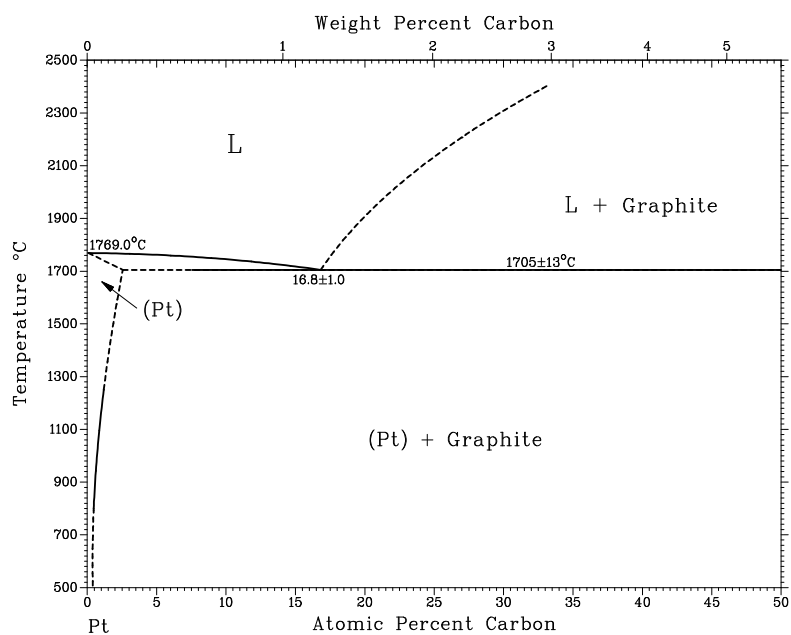


Figure A.5: Pt-C [Oka90]

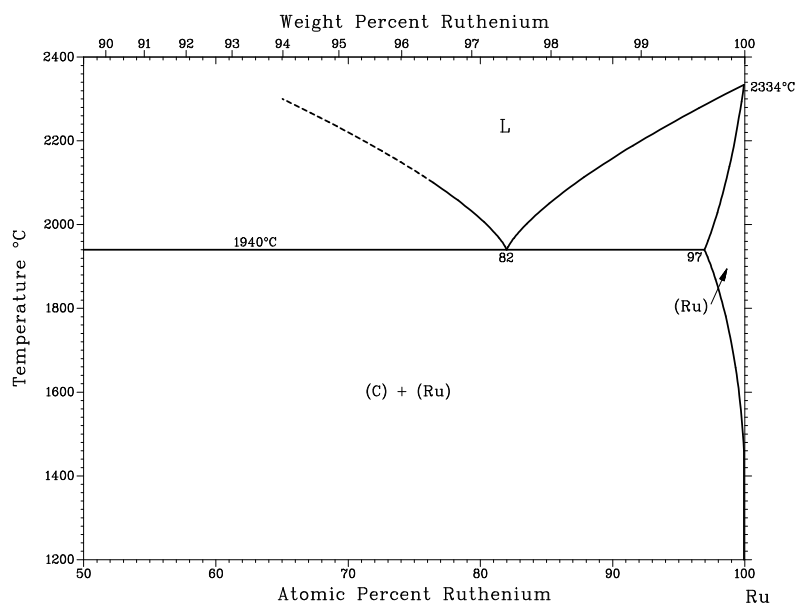


Figure A.6: Ru-C [Oka90]

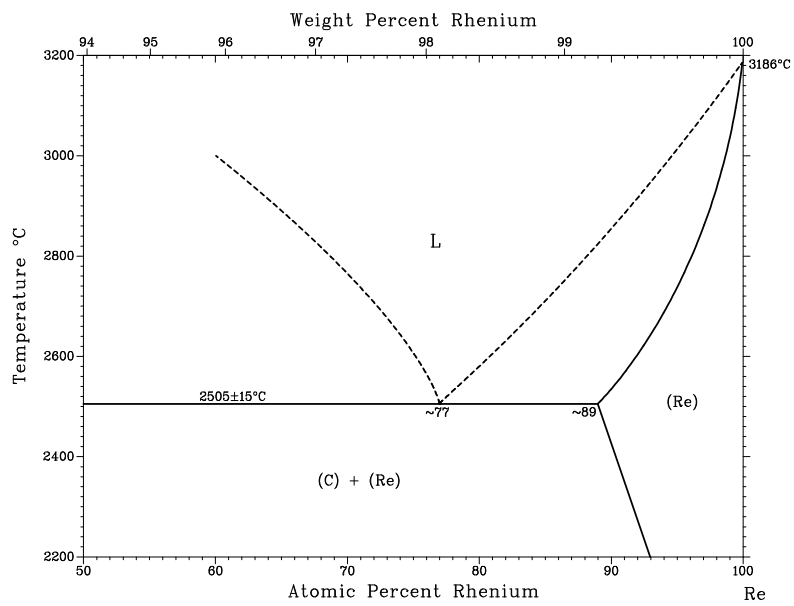


Figure A.7: Re-C [Oka90]

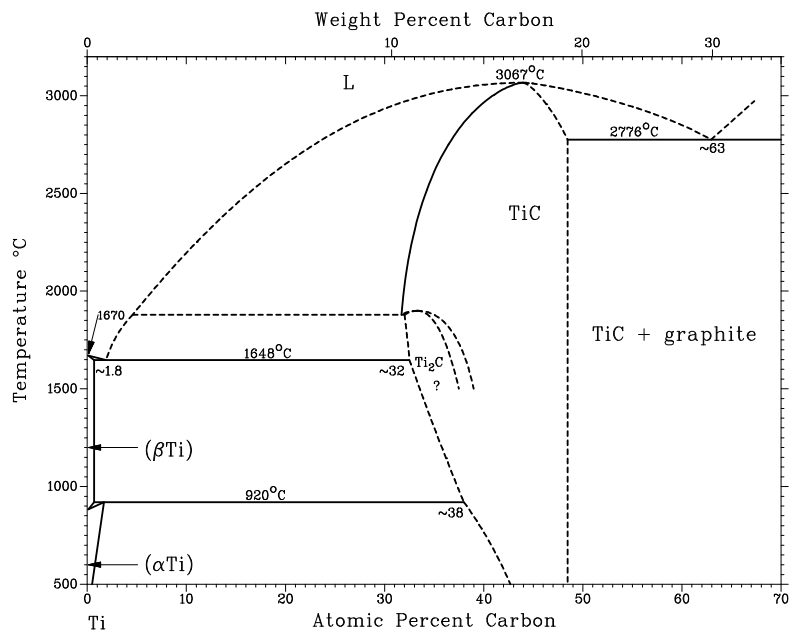


Figure A.8: TiC-C [Oka90]

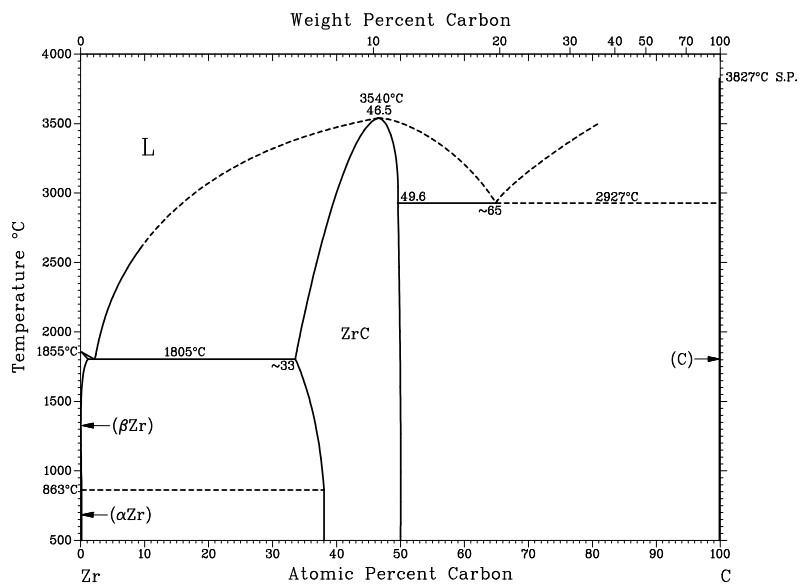


Figure A.9: ZrC-C [Oka90]

	Pure substance			M-C eutectic			
	density (s) [g/cm ³]	weight % [%]	vol % [%]	density [g/cm ³]	T melt [°C]	Ingot mass for small cell [g]	Ingot mass for small cell with C/C sheet [g]
Au	19.32				1064.2		
Cu	17.28				1084.6	ca. 30	22
Fe	7.87	4.2	13.2	7.1	1153	ca. 30	
Co	8.9	2.6	9.5	8.3	1320	ca. 30	
Ni	8.9	3	10.9	8.2	1326.5	ca. 30	
Pd	12.02	2.7	12.9	10.8	1492	ca. 40	
Rh	12.41	1.9	9.6	11.4	1657		
Pt	21.45	1.2	10.3	19.5	1738	ca. 75	55
Ru	12.37	2.5	12.3	11.1	1953		
Ir	22.56	1.6	14	19.7	2290		
Re	21.02	2	16	18	2474	ca. 70	62
C	2.26						

Table A.1: Physical properties of selected metals, carbon and metal-carbon alloys at the eutectic composition

Acknowledgement

The last years I spent with M-C eutectics and radiometry have been an intense and manifold experience, that I cherish and of which I am proud. I feel indebted to many people who contributed to this work, both from a scientific and a human point of view.

First of all, I would like to thank Axel Hoffmann for his willingness to supervise this work, his continued guidance and the fruitful discussions helped a lot.

At the Physikalisch- Technische Bundesanstalt I owe a hearty thank you to Jörg Hollandt and especially to Jürgen Hartmann for their constant support, valuable teachings and the insight into radiometric and thermo-physical principles.

Stephan Schiller and Beate Pruszeit helped to run and sometimes to repair the high-temperature furnaces, while the necessary graphite parts were promptly coming from the friendly mechanic of the working group Thomas Schönebeck. The help of Rüdiger Friedrich and Dieter Taubert was essential for the absolute calibration of the filter radiometers. Also, they are hosts for lively discussions with Christian Monte, Berndt Gutschwager, Thada Keawprasert, Rolf Thomas and Narudom Noulkhaw.

Stephan Sarge and Yosuke Moriya introduced me to differential scanning calorimetry and helped me a lot to investigate tiny fixed-point samples.

Yoshiro Yamada gave me the opportunity to work for one year in the stimulating environment of the NMIJ in Tsukuba/Japan. During this time the scientific work, discussions and excursions broadened my view on thermometry and japanese bathing culture. どうもありがとうございます to Yoshi and his family, Nao Sasajima, Pieter Bloembergen, Tiejun Wang, Yunfen Wang, Zheng Wei and Boris Khlevnoy.

Within the HIMERT consortium, I have to thank Graham Machin and Dave Lowe of the NPL, Mohamed Sadli and Ronan Morice of the CNAM/INM-LNE and Pablo Jimeno-Largo and Miguel Villamanan of the University of Valladolid(E) for preparing the small aperture fixed-point cells, and exciting comparisons and discussions.

I acknowledge the work of Mikhail Sakharov and Boris Khlevnoy of the VNIIOFI for building large aperture fixed-point cells and bringing them to PTB. Their expertise on running and improving the HTBB furnace was very helpful.

Finally, I am deeply grateful for the support I received from my family. I thank my wife Anette and my son Karl Moritz for putting up with late hours and spoiled weekends and inspiring and motivating me with their love and liveliness.